M.MURAT KARASAN

METU 2007

# RESIDUAL STRESS ANALYSIS OF RIVETING PROCESS USING FINITE ELEMENT METHOD

M. MURAT KARASAN

NOVEMBER 2007

# RESIDUAL STRESS ANALYSIS OF RIVETING PROCESS USING FINITE ELEMENT METHOD

A THESIS SUBMITTED TO
THE GRADUATE SCHOOL OF NATURAL AND APPLIED SCIENCES
OF
MIDDLE EAST TECHNICAL UNIVERSITY

BY

M. MURAT KARASAN

IN PARTIAL FULFILLMENT OF THE REQUIREMENTS
FOR
THE DEGREE OF MASTER OF SCIENCE
IN
MECHANICAL ENGINEERING

NOVEMBER 2007

Approval of the thesis:

## “RESIDUAL STRESS ANALYSIS OF RIVETING PROCESS USING FINITE ELEMENT METHOD”

submitted by **M.MURAT KARASAN** in partial fullfillment of the requirements for the degree of **Master in Science in Mechanical Engineering** by,

Prof. Dr. Canan Özgen
Dean, Graduate School of **Natural and Applied Sciences**

Prof. Dr. Kemal İder
Head of Department, **Mechanical Engineering**

Prof. Dr. Suat Kadıoğlu
Supervisor, **Mechanical Engineering, METU**

**Examining Committee Members:**

Prof. Dr. Metin Akkök.
Mechanical Engineering, METU

Prof. Dr. Suat Kadıoğlu
Mechanical Engineering, METU

Assoc. Prof. Dr. Mehmet Çelik
Aselsan

Assoc. Prof. Dr. Bora Yıldırım
Mechanical Engineering, Hacettepe University

Assist. Prof. Dr. Serkan Dağ
Mechanical Engineering, METU

**Date:**

**I hereby declare that all information in this document has been obtained and presented in accordance with academic rules and ethical conduct. I also declare that, as required by these rules and conduct, I have fully cited and referenced all material and results that are not original to this work.**

Name, Last Name: M. Murat KARASAN

Signature:

# ABSTRACT

## RESIDUAL STRESS ANALYSIS OF RIVETING PROCESS USING FINITE ELEMENT METHOD

Karasan, M. Murat
M.S., Department of Mechanical Engineering
Supervisor: Prof. Dr. Suat Kadıoğlu

November 2007, 98 pages

Rivets are widely used as a means of fastening in airframe construction industry. There are various types of riveted joints on an aircraft fuselage or on a helicopter body. Among the other types of fasteners riveted joints are preferred in such applications due to; their permanence after installation and their economical advantages. In a riveted joint, it is known that residual stresses are present as a result of the installation process. Furthermore, during the flight of an aircraft, the fuselage is loaded in one cycle and such cycles are repeated throughout the service life. As a result, the panels and the rivets are subjected to fatigue type loading. The integrity of the joint must be maintained against this combination of service loads and the residual stresses. Hence, the riveting process parameters which influence the residual stresses are utmost critical in terms of fatigue life of the hole body.

In this study it is aimed to obtain an accurate numerical model of a single-lap riveted joint which is widely used in airframes. 2-D axisymmetrical and 3-D numerical models are generated using commercial finite element code ABAQUS/CAE and subsequent parametric studies are carried out on these models. The Results of both models are compared with those found in the literature.

Clearance between hole and rivet shank is selected as the primary parameter to be inspected. The effects of hole clearance on the final residual stress field are examined on 2-D and 3D models. Furthermore, a through the thickness, crack on the inner panel which is initiated after installation is modeled. The crack is perpendicular to the direction of loading. It is placed to the residual tensile stress zone that surrounds the rivet hole. Hence, the effects of residual stresses are also taken into account. For a riveted joint subjected to fatigue loading, such a macroscopic crack could eventually form. In this thesis, stress intensity factors (SIF's) for this crack are calculated for various parameters such as clearance and crack length. These can be utilized in a subsequent fatigue crack growth analysis as the initial values or they can be used in a fracture analysis, to predict unstable crack growth due to overload (i.e. crack linking).

**Keywords:** FEM, riveted joints, residual stress, hole clearance, SIF calculation

# ÖZ

## PERÇİNLİ BAĞLANTILARDA OLUŞAN KALINTI GERİLMELERİN SONLU ELEMANLAR YÖNTEMİYLE ANALİZİ

Karasan, M. Murat
Yüksek Lisans, Makina Mühendisliği Bölümü
Tez Yöneticisi: Prof. Dr. Suat Kadıoğlu

Kasım 2007, 98 sayfa

Perçinler uçak gövdesi endüstrisinde yaygın olarak kullanılan bağlantı elemanlarıdır. Uçak ve helikopter gövdesinde farklı türde birçok perçin türü kullanılmaktadır. Perçinlerin diğer bağlantı elemanlarına göre tercih edilmesi; montajdan sonra sökülmemeleri ve ekonomik olmaları nedeniyledir. Perçinli bağlantılarda perçinleme işlemi sonucunda oluşan kalıntı gerilmeler vardır. Ayrıca uçuş esnasında uçak gövdesi tek bir döngüde yüklenmektedir ve bu döngü uçağın ömrü boyunca tekrarlanmaktadır. Bunun neticesinde gövde panelleri ve perçinler yorulma türünde yüklere maruz kalmaktadır. Perçinin bağlantıların sağlamlığı bu iki farklı yükün birleşimine dayanacak özellikte olmalıdır. Bu nedenle kalıntı gerilmeleri etkileyen perçinleme işlemi parametreleri uçak gövdesinin yorulma ömrüne etkisi yönünden çok kritik hale gelmiştir.

Bu çalışmada uçak gövdesi yapımında sıklıkla kullanılan tekli bindirme bağlantısının gerçekçi bir sayısal modelinin geliştirilmesi hedeflenmiştir. İki boyutlu eksenel simetrik ve üç boyutlu sayısal modeller ABAQUS/CAE programı kullanılarak elde edilmiş ve diğer parametrik çalışmalar oluşturulan bu modeller üzerinde gerçekleştirilmiştir. Bu iki modelden elde edilen sonçlar literatürde bulunan benzer çalışmalarla karşılaştırılmıştır.

Percin gövdesi ve delik yüzeyi arasındaki boşluk incelenecek öncelikli parametre olarak seçilmiştir. Delik boşluğunun kalıntı gerilmelere etkisi iki boyutlu ve üç boyutlu model üzerinde incelenmiştir. Son olarak plaka kalınlığı boyunca yer alan ve perçin çakma işleminden sonra oluşmuş bir çatlak modellenmiştir. Çatlak, yükleme yönüne dik olarak perçin deliğini çevreleyen çekme gerilme bölgesine yerleştirilmiştir. Bu tarz bir çatlak yorulma yükü etkisi altındaki perçinli bağlantıda oluşabilecek bir çatlaktır. Bu tez kapsamında bu tür bir çatlağın gerilme şiddeti çarpanı perçinleme işlemi parametrelerine göre değişimi hesaplanmıştır. Bu çalışmanın sonuçları bir çatlak ilerlemesi çalışmasında başlangıç değeri olarak veya bir kırılma analizinde aşırı yük altındaki bir çatlağın ilerlemesini incelemek amacıyla kullanılabilir.

**Anahtar kelimeler:** Sonlu elemanlar analizi, perçinli bağlantılar, kalıntı gerilmeler, gerilme şiddeti çarpanı

**To My Family**

# ACKNOWLEDGMENTS

I would like to express my deepest gratitude and appreciation to my supervisor Prof. Dr. Suat Kadıoğlu who inspired, encouraged and supported me at all levels of this study.

I would like to thank to my friend Fatih Altunel, whose friendship, support and suggestions made great contributions to this work. This thesis would not be complete without talking of Fatih Murat Eğilmez who was always there for listening me patiently.

I am also grateful to TUBITAK for encouraging Turkish students in participating graduate studies and providing them scholarship.

Throughout the work I made pretty helpful discussions on ABAQUS with Cemal Gözen from A-Z Tech, without his help this work would be much difficult for me.

Finally, my greatest thanks go to my family who shaped me with their never-ending patience.

# TABLE OF CONTENTS

CHAPTER

APPENDICES

# LIST OF FIGURES

# CHAPTER 1

# INTRODUCTION

## 1.1 Motivation

In earlier times of the manufacturing and design, casting was the primary method to realize the desirable shapes in metal. However, limitations arising from the casting technique prevented to obtain the parts in desirable shapes and sizes. At this point, the idea of joining emerged in order to create more complex and larger assemblies from separate parts.

Today, all types of the joints can be classified into two main groups; namely, permanent joints and nonpermanent joints. Examples to nonpermanent joints are threaded bolts, setscrews and pins. As the name implies this type of joints give chance to disassemble the joint which can be useful for maintenance purposes. On the other hand, techniques like bonding welding, brazing and the riveting can be counted in the other group. The main advantage of this group lies in the property of hindering nonintentionally opening of the joint.

Among the other type of joints, the riveted connections are the most preferred ones especially in aircraft and helicopter fuselage production. As compared to threaded fasteners, riveted connections are preferred due to their permanence after installation and their economical advantages such as lower unit cost, no threading of the material to be joined required and installation in a relatively short time. A solid rivet has a shank and a manufactured head before installation, after installation the driven head is formed (Figure 1.1). For a proper installation, usually an impacting tool is used. While applying force on the manufactured head, a flat bucking bar is hold against the driven rivet head. The impacting tool is actuated either by hydraulic, pneumatic, electro-magnetic or manual means [1].

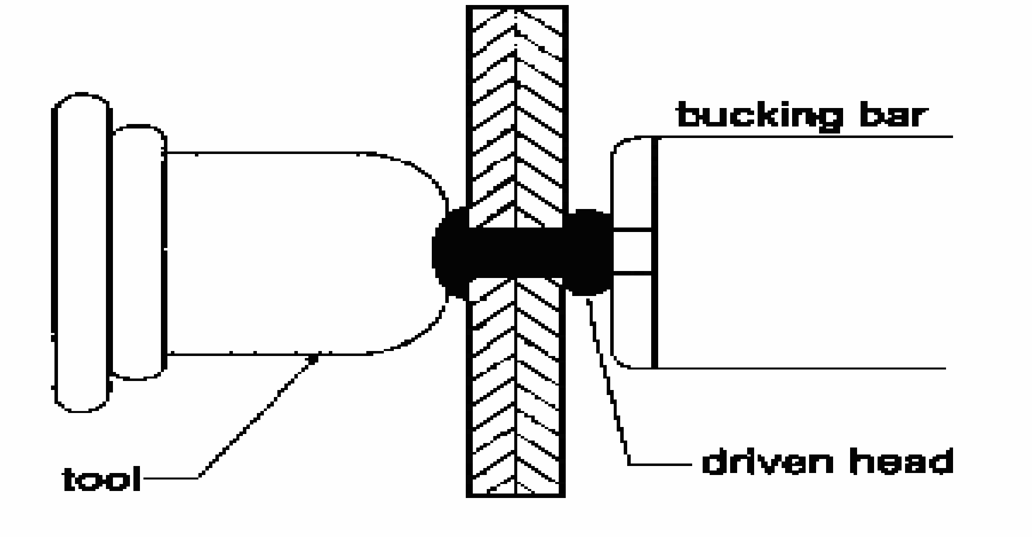

**Figure 1.1** Schematic view of rivet installation [1]

Typically aircraft fuselage is composed of stiffened metal panels, as shown in Figure 1.2, which are attached to the main frame of the aircraft body through intermediate clips Outer skin of an aircraft is manufactured by layering two (single-lap joint) or three (double lap joint) sheets of metal panel and then joining them by means of a fastener. During assembly of the fuselage, numerous amount of solid rivets, blind bolts and threaded fasteners are used. For example, the rear pressure bulkhead of a Boeing 747 aircraft requires approximately 100,000 solid rivets for assembly [2].

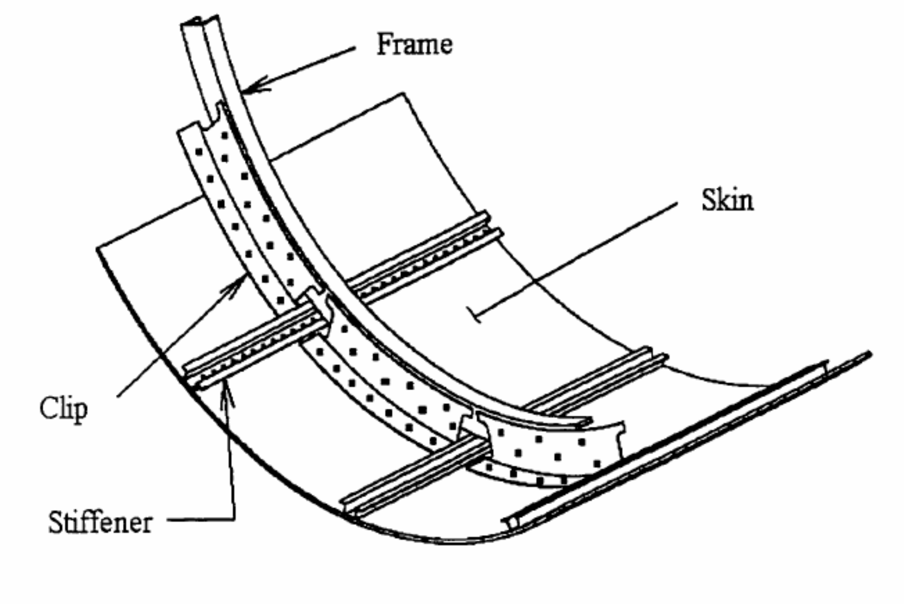

**Figure 1.2** Schematic view of stiffened panel [2]

The outer skin of an aircraft typically fastened with flush-head fasteners to minimize aerodynamic drag, while non-aerodynamic joints are fastened through lower cost and easy to analyze protruding head fasteners (Figure 1.3).

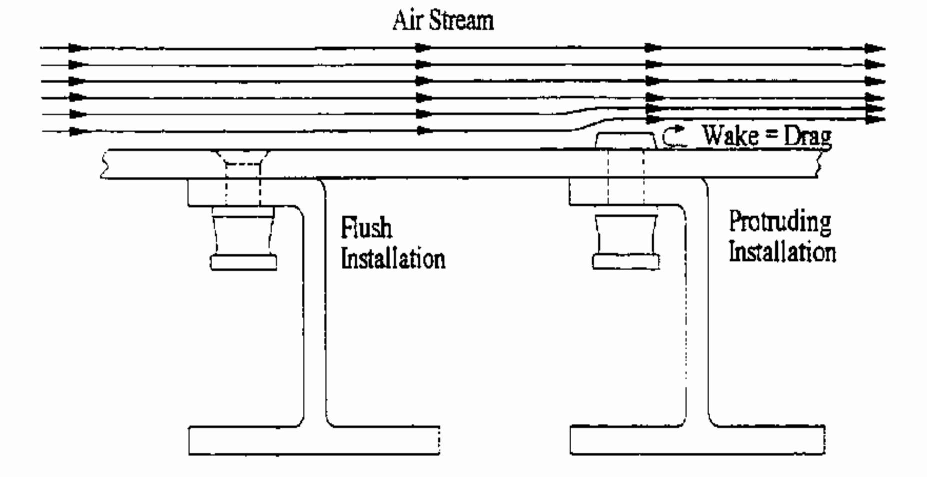

**Figure 1.3** Schematic view of aerodynamic drag [2]

## 1.2 Literature Survey

Rivets are essential parts of various structures. As a consequence many researches have been carried out on riveting design parameters. The main topics that have been adressed till now are as follows: Riveted airframes[3,4], residual stress prediction [1,5], load sharing between rivets [6], design of single lap joints [4,7], fatigue life evaluation [8] and fretting problems [9]. In addition, after the evolution of Finite Element Analysis (FEA) 2D and 3D static and dynamic riveted joint modeling and analysis have been realized. Brief descriptions of recent relevant studies on this area are given below.

Typical aircraft structure is manufactured by layering two sheets (single-lap joint) or three sheets (double-lap joint) of material and than joining the assembly by using a fastener [1]. As a widely used joining technique riveted joints' reliability has a direct proportion to the reliability of the aircraft fuselage. As a result there are many ongoing researches on the fatigue performance of the riveted joints. Main benefits of the improvement of the fatigue life of the riveted joints to the aircraft industry are reduction of the unscheduled maintenance, increasing the maintenance period, reduction of the maintenance cost and improvement of the airplane readiness [10]. In general, it can be said that any factor that changes local state of stress in and around the riveted joint affects the fatigue performance of a riveted joint. Local state of stress combined with the surface condition determines the fatigue life of the joint. Hence, it is important in terms of riveted joint life to investigate the role of each riveting parameter on the local state of stress that is induced after installation.

The stress levels on many aircraft joints experience the effect of plasticity. Plasticity changes the load distribution between the rivets and the local stress around the joint [3, 11]. Because of this, three-dimensional contact model with elastic-plastic material model should be employed for an accurate numerical model of the riveted joint [3]. It is also possible to represent the riveted joint by a two-dimensional finite element model with either linear or nonlinear type of an analysis [12]. Obviously the accuracy is better for nonlinear analysis but it consumes much more time than the linear analysis. Here a compromise may be needed between the time and the accuracy.

During setting, a portion of the rivet's material is forced into the rivet hole. A sufficient hole fill is required for a long service life of the riveted joint. Comparison of an orthotropic and an isotropic material is performed in the literature[13] and more homogenous hole fill is observed in the case of isotropic material as the stiffness of the orthotropic material is varying depending on the direction of the fibers. Larger radial expansion is observed in the less stiff direction of the material property. In that study besides the fiber metal laminates material, effect of inhomogeneity is also observed for the isotropic material but not as pronounced.

It is important to investigate the mechanisms that alter the stress distribution around the joint. In a strain gage analysis that carried out to investigate the edge margin effects for a countersunk type rivet, the riveting process was divided into seven main steps (Figure 1.4) in terms of change of stress and strain values [7]: In the first step the rivet is crushed and it does not have interaction with the plate yet, than in the second step the rivet shank comes into contact with the hole surface and radial compressive stresses develop within the plate. The formation of the driven head of the rivet occurs in the third step and another contact region between the plate and the rivet driven head is created, some material of the rivet is trapped by the rivet driven head and this causes the reversal of the compression state to a radial tension state. The formation of the driven head continues and a lug which is seen in Figure 1.5 is eventually formed. As the rivet takes its final shape the displacement of the loading bar has stopped, this step is dedicated to the stress homogenization and it constitutes the fifth step. The sixth step begins with the release of the load but the rivet head keeps in contact with the loading bar, the elastic recovery of the driven head results in a new radial compression state in the plate. Finally in the seventh step the plate's partial elastic return occurs and the strain gages show a tension state. Reversal of stress which constitutes the third step is an essential phase in terms of formation of the clamping stress [14].

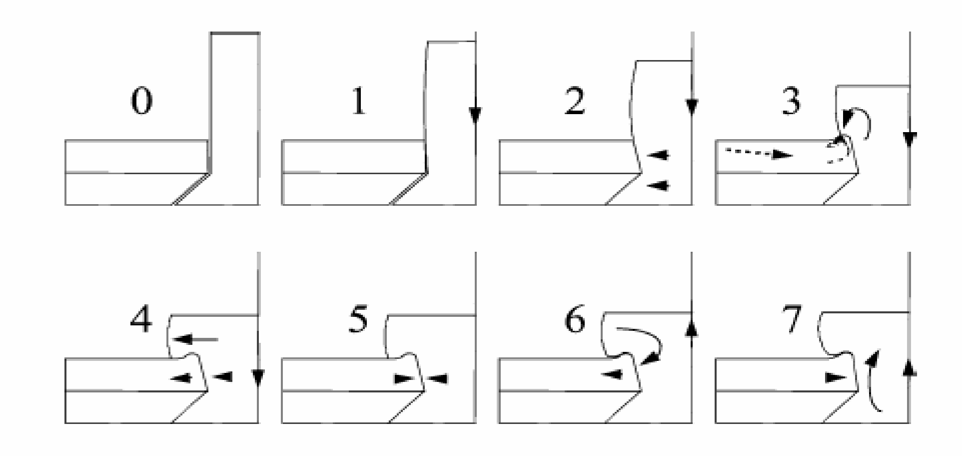

**Figure 1.4** Riveting mechanism stages [7]

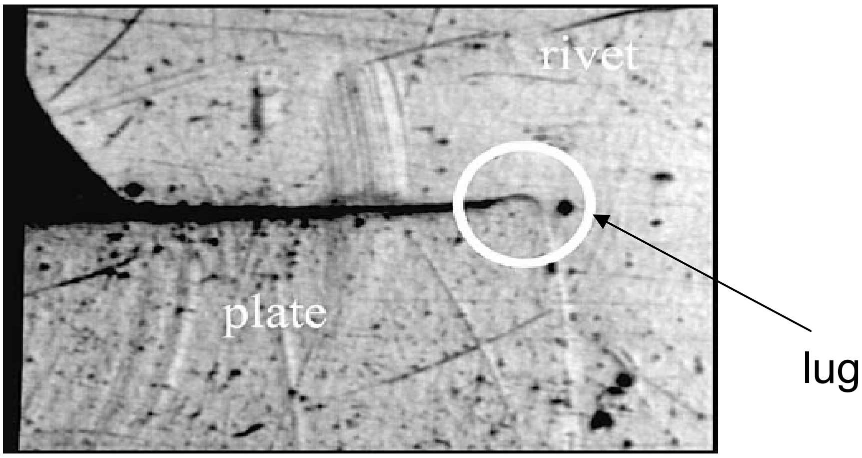

**Figure 1.5** Lug visualization [7]

Clamping stress is defined as the load exerted by the rivet to the plates divided by the cross-sectional area of the rivet shank at the interface between the sheets. High squeeze force applied to the rivet head produces high clamping stress and it is found beneficial in terms of fatigue life in the literature as it induces compressive stresses in the vicinity of the rivet hole [1, 3, 11, 14]. In a study, aiming to model the residual stress field formed during riveting process, the squeezing force is found to have a significant effect on fatigue performance of the joint. High squeeze forces results in retardation of fatigue crack growth at the rivet/hole interface by increasing the magnitude of compressive stress field around the rivet hole [1]. On the other hand by pushing the tensile hoop stress zone away from the rivet/hole interface it helps fatigue crack nucleation and propagation at the faying surface away from the joint. In addition, high squeeze forces produce large driven head; up to a certain value of radius larger headed rivets are found to have enhanced fatigue life as large rivet head reduces bending stress on the joint [1]. In addition the size of the rivet head changes the clamping stress, Deng [14] in his study on the parameters affecting the residual clamping stress after rivet installation revealed that a critical value of rivet head to rivet thickness ratio exist for an idealized double sided symmetric rivet model. Deng also reported a relation between the clamping stress and initial gap size left between the rivet head and the sheets. For a specific value of the ratio of the gap and the sheet thickness the clamping stress reaches a maximum value asymptotically. The value of the rivet's yield stress should be kept close to the sheet's yield stress to achieve as large clamping stress as possible. He also reported that, although strain hardening does not alter the riveting process steps, it changes the final stress state.

Plate geometry and the position of the rivet relative to the edges and vertices of the plate are found to alter the residual stress field around the rivet hole. In a study aiming to quantify this effect numerically and experimentally, a flush head rivet is crushed into a circular and a square plate and the stress distribution data is extracted by means of strain gages. It is seen that the larger plate results in increased stress localization, high strain values around the rivet hole, on the other hand as the plate dimensions become smaller the strain values throughout the plate is distributed more homogenously. Similar results are seen for the square geometry in median direction but in diagonal direction the situation is totally changed [7]. Heywood [15] stated that three dimensions of the plate affect the joint strength: The sheet thickness, the diameter of the rivet and the pitch (width of the plate). Fung [11] found that the plate thickness hardly affects the stress state. Fung has observed that decreased pitch and thicker plates have longer fatigue lives. For a riveted joint the designer should keep the value of the 2r/t high to have an increased fatigue life where r and t being the radius of the rivet and thickness of the plate, respectively.

In terms of fatigue life, joint configuration also has a significant influence such that double shear joint arrangements are found up to 10 times stronger than single lap joints. In addition, applying multiple fastener rows increases the fatigue strength in simple lap joints [3, 16]. It is observed that the fretting failures are reduced to only %10 of the failures by the help of multiple fastener rows [3], due to reduction in the relative displacement of the plates. Heywood [15] stated that typical fatigue strength of a double row simple lap joint is 1.4 times better than the fatigue strength of a single row simple lap joint.

During its service life a riveted joint undergoes different types of loading. A test set up called Arcan (Figure 1.6) is used to simulate the different directions of loading on the rivet. Observations revealed that up to α=30˚ the failure is due to punching of the manufactured rivet head by the rivet shank, beyond this angle the manufactured head is sheared. Figure 1.7 shows the samples of the failed riveted joints during tests. According to Reference 7, the failure of the rivet head is always caused by the shear stress even in a pure tension loading condition.

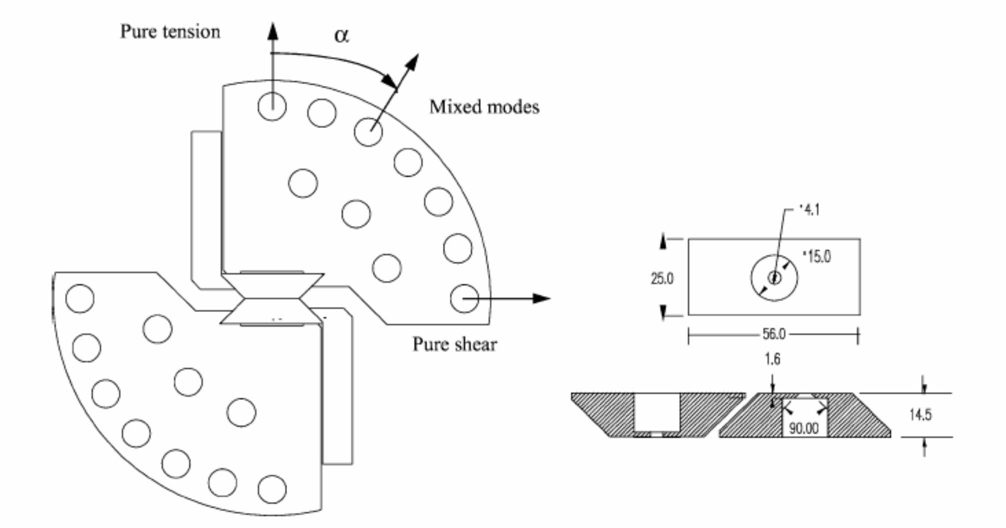

**Figure 1.6** Arcan rig and test specimen [7]

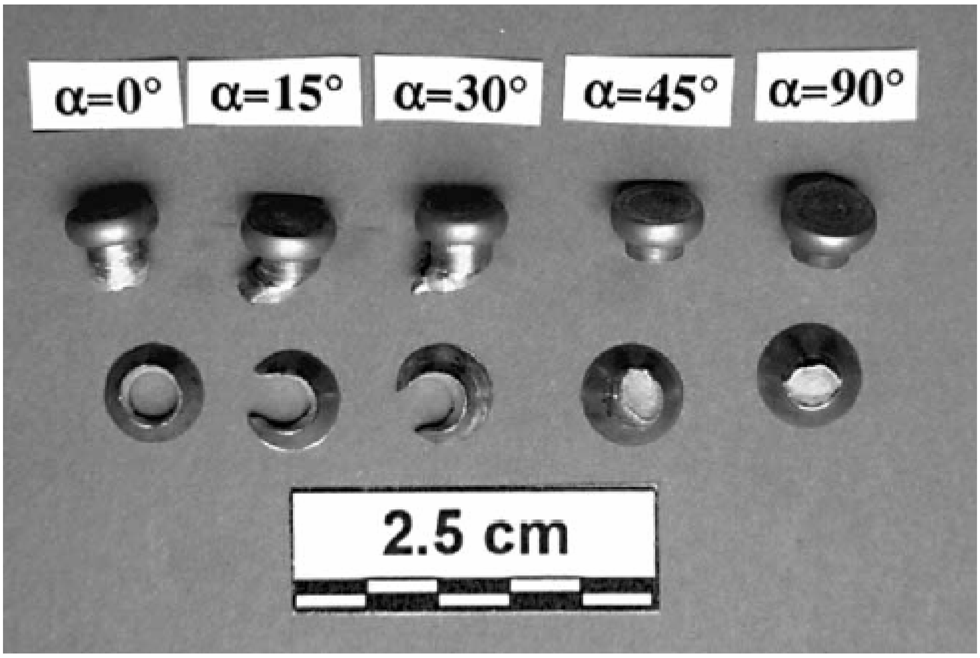

**Figure 1.7** Failure modes of rivet [7]

Tolerances of the rivet and the hole can contribute to the stress distribution around the joint. It is observed that interference enhances the fatigue life of a universal head type rivet but it is insignificant for a countersunk type rivet.

Interference fit fasteners are found more beneficial among the other type of joints (e.g. clearance fit, neat fit) [11].

The fatigue life prediction is made via either the stress life or the strain life approach. Fung [16] showed that strain life approach gives far better results than the stress life approach.

Rivet installation generates relatively large stresses around the rivet holes. As a result, considering the fatigue life of the joint the fastener holes become critical locations. Toparli, et al. [5] focused on the effect of the cold-working of the fastener hole on the fatigue life of the specimen. Finite element analysis and experiments were performed and the results were compared. The radial expansion and the stretching methods are used to generate the compressive residual field. The stress field is obtained by using the finite element method; crack growth rates and the stress intensity factors are extracted from the analysis. The same parameters were found with experimental procedures and compared. Cold-working of fastener hole was found beneficial in terms of fatigue life. Among the two methods applied in that program the radial expansion method was seen to be more effective. In another analysis program the cold working of the rivet hole was studied [10]. The effect of using models with different levels of complexity was examined. 2-D, 2-D axisymmetric and 3-D finite element models with different material properties namely elastic, elastic perfectly plastic and hardening material behavior were generated. In addition two different kinds of geometries namely finite rectangular plate and infinite cylindrical plate are included in the analysis program. The residual stress field through the thickness of the plate was compared for each different model. Although the physics of the cold working process was not altered, different stress levels were reached. In 2-D axisymmetric model higher maximum tensile and compressive stresses were achieved than that of the 3-D model. Moreover, higher stress values were read for hardening material behavior. An important result of that analysis is that residual compressive stress which is responsible for the retardation of the crack from the hole edge by decreasing the stress intensity factor varies along the thickness of the plate. Hence, this phenomenon should be taken into account in calculating the stress intensity factors of cracks that do not cross the entire thickness.

Multiple site damage (MSD) is a significant phenomenon that affects the service life of an aircraft. MSD is a major threat to the aging aircraft fuselage. In MSD type of a failure cracks initiate at different joint hole locations, they grow and finally join forming a large, visible crack that can cause the catastrophic failure of the whole structure. As in the case of conventional fatigue crack the cracks initiate at a point of stress concentration such as discontinuities and fretted surfaces. Poor drilling method can also trigger formation of crack [17, 18]. In most cases, cracks grow longitudinally in the direction of the rivet row. After the initiation of the cracks similar crack growth characteristics are observed in fuselage skin panels. By linking-up of a two adjacent crack in a rivet row, a lead crack forms and this linked crack grows much faster than unlinked cracks. The critical size of the MSD crack can be much smaller than that of a single crack. In general, the shortest life occurs when the largest cracks grow towards each other from adjacent fastener holes. Larger life is expected if cracks initiate in widely separated holes and link up. The residual life is either predicted by calculating the stress intensity factor of the part and comparing it with the plain strain fracture toughness, if the plain strain conditions prevail, or the stress is re-calculated each time taking into account the reduction in the cross-sectional area and a failure criterion is applied.

The structural loads exerted on a lap joint are transferred by means of joint holes. The fastener holes are drilled commonly by hand during fuselage production. Although it seems to be simple machining process, its quality may deeply affect the final stress distribution around the joint. An improperly drilled hole may create regions of stress concentration hence, it diminishes the fatigue life. Ralph et al. [18] focused on some number of variables affecting the hole drilling process namely: Use of pilot hole, condition of bit, bit length, feed rate and operator experience. During the study surface roughness, number and the orientation of the gouge marks and the conicality of the hole surface are measured. Among the parameters studied in that paper pilot hole utilization produced the greater effect on the hole quality. Pilot hole application reduces the number of gouge marks and the surface roughness significantly. In addition, a new drilling bit leaves fewer marks than an old bit. Due to vibration longer bits increases surface roughness in hand drilling. Higher feed rate leaves more gouge marks than lower feed rate since, pressure applied to the tip results in deflection of the tip. In that study it was revealed that by taking simple precautions during manufacturing of the fastener holes, fatigue life of the fuselage can be improved greatly.

There are many riveted joint configurations applied to several different fastening applications. Among them riveted joints having three rows of rivet in one column are widely used in aircraft applications. In the case of multiple rivet rows load sharing of the rivets becomes critical in terms of fatigue life prediction. Moreira et al. [6] studied load sharing characteristics of such a joint numerically using ABAQUS as finite element code. For this purpose the joint assembly was divided into three sections and the force carried by each cross-section was calculated using the nodal stress values. The authors concluded that the first and the last rivets carried the majority of the applied load.

There is not a clear agreement on the effect of friction on local state of stress around the riveted joint. There exist both types of studies claiming that it is a significant factor or its effect is negligible. The frictional forces become more significant when the clamp-up forces are increased [3]. As the friction is increased, more load is transferred via the contacting surface. As a result, stress and strain levels are reduced. Although decreasing stress levels have favorable influence on the fatigue performance, the fatigue life expected to be lower as increased frictional forces trigger the fretting fatigue. This effect is more severe for the multiple fastener rows since, the contacting areas of the plates are larger [11, 14].

As stated before, a major threat in terms of service life of riveted joints especially used in fuselage construction is the existence of the fatigue cracks. These cracks, most of the time, either initiate in the vicinity of the hole edge or on the faying surface where the plates contact each other [19]. The reason for the former type of cracks is high contact stresses developed in this region whereas; the latter one is the due to relative motion of the plates. Figure 1.8 shows these regions schematically.

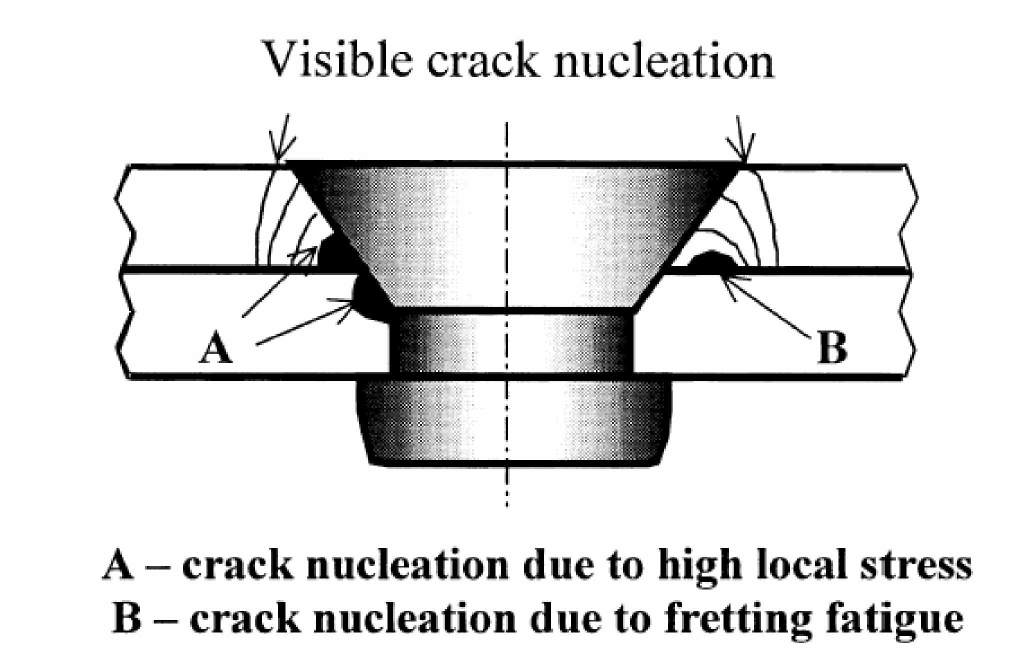

**Figure 1.8** Crack nucleation sites for riveted connection [19]

In the case of a general cracked structure problems calculation of the stress intensity factors (SIF) , which characterize the magnitude of the crack tip stress field, plays a significant role. There are three main ways to calculate the SIF numerically. These are: Displacement extrapolation technique, strain energy release rate and J-Integral technique [24]. In the literature there are many attempts to calculate the SIF using finite element method. Courtin et al [20] calculated the SIF of a compact tension (CT) specimen and a round bar by commonly used displacement extrapolation technique and Rice's J-Integral approach [32]. Their aim was to compare these techniques in predicting the SIF and to show the power of the each technique. Throughout their study ABAQUS was used as the finite element software. They reported that ABAQUS which can calculate the J-Integral automatically is sufficiently accurate and easy to apply for linear elastic fracture mechanics (LEFM) problems. In that study it was also observed that, by the help of ABAQUS, J-Integral approach is easier to apply than the application of quarter node point technique for most of the problems. However, J-Integral method turns out to be path dependent integral in the presence of residual stress field and can not be directly obtained using commercial codes. This fact was proved with an analysis and presented in Figure 1.9. In general, the J-Integral values are expected to converge to a certain value as the numbers of the contours are increased. But a contrary situation was observed in Figure 1.9 and the J-Integrals were diverged. Hence, this method is not appropriate for the current study. In another study aiming to represent capability of finite element software in modeling crack tip singularity and the SIF prediction some common type of specimens were modeled [21]. Plate with a central through crack and plate with a central circular hole with one or two edge crack were modeled applying different mesh densities. The results obtained in that study were compared with those predicted by the mathematical formulations. The finite element results were found consistent with the mathematical results.

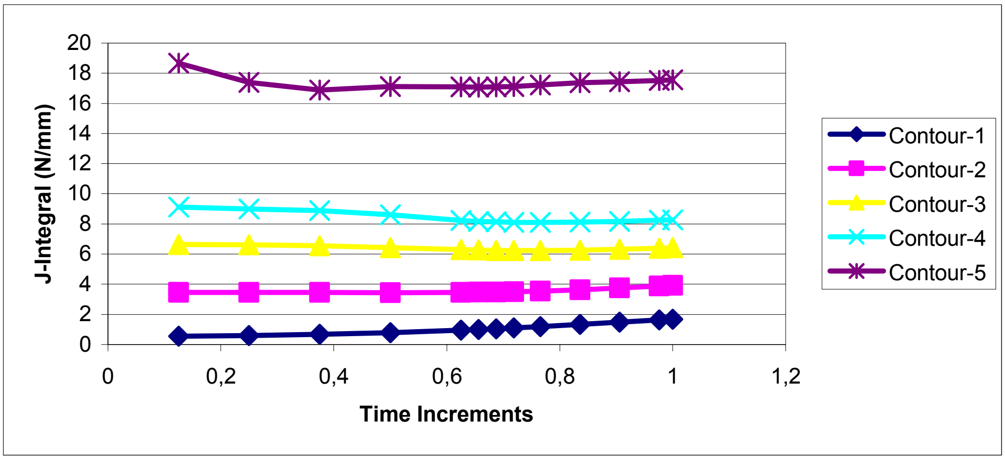

**Figure 1.9** J-Integral values for a through crack in the presence of residual stress field

Moreover, in Reference 6 the interaction of rivets and cracks has received attention. In this study effects of the cracks on the load sharing characteristics of riveted joints were studied [6]. For a single column with three rivets arrangement a symmetrical and an asymmetrical crack were modeled on the sides of the first hole. The subsequent loading was applied on both ends of the plates and effects of the residual stresses were not taken into consideration. Twenty-node brick elements were used for the mesh. The elements in the vicinity of the crack tip were manipulated such that their one side is collapsed and the midside nodes was moved to the quarter of edge length distance from the value of the crack tip, by this way the square root singularity was simulated. SIF's are extracted through the thickness of the plate and an average value of the SIF's are calculated for each element. Again the J-Integral technique was used throughout the study. In that study it was observed that presence of the crack affects the load sharing of the joints. The middle and the last rivet carry more load as compared to uncracked configuration. The load carrying capacity of the first rivet diminishes. Finally, for a given crack length and surface, SIF of the symmetrical crack always higher than that of an asymmetrical crack.

In conclusion, a wide survey of literature revealed that many critical design parameters have been studied till now. However there are still some parameters which have been examined but requiring more profound analysis. Effect of clearance on the residual stress field and the interaction of the residual stress field and cracks are examples of such parameters. This study will primarily focus on these topics.

## 1.3 Aim and scope of this study

In 1988 an aircraft which belongs to Aloha Airlines had an accident during a short flight. A portion of the fuselage was separated from the main frame of the aircraft in air. Experts report revealed that the sudden linking of small cracks at and around the rivet holes was the reason for that accident.

This incident made the researchers to concentrate on the parameters affecting the fatigue life of the metal panels constituting the fuselage. Hitherto many analytical, experimental and numerical studies have been carried out on the parameters coming out during design and manufacturing stage. Among these parameters the ones that manipulate the residual stress state at and around the joint locations was found to play the most significant role on the fatigue life of the hole structure.

This study focuses on the residual stress state and its interaction with a nearby crack at a riveted joint.

Firstly, an attempt has been made to develop accurate finite element models in 2-D and 3-D to simulate the installation of the rivet. Commercial software ABAQUS/CAE Version 6.6 which has implicit and explicit solving capability was used for this purpose. The model included all types of nonlinearities namely geometric, material and boundary conditions (contact). Clamping (installation) process and installation of rivet and forming of the driven head was simulated first.

Secondly, affect of the clearance, between the rivet shank and the hole, on the residual stress field has been investigated for a universal head rivet. An axisymmetrical finite element model was used to explore the clearance effect for the unloaded model, then loading was applied to a 3-D model and again the effect of same parameter was investigated on this model.

Thirdly, a defect in the form of a through crack in the elastic region was introduced on the 3-D finite element riveted joint model. Stress intensity factors (SIF's) were extracted from this model. Effect of joint clearance on SIF's were studied.

# CHAPTER 2

# STRESS ANALYSIS OF THE RIVETING PROCESS AND MODEL VALIDATION

## 2.1 Introduction

Finite element analysis has proven to be a powerful modeling tool for a wide range of problems encountered in mechanical engineering area. Also in this research it was aimed to establish accurate numerical models of the riveting process in both 2-D and 3-D. Here the capabilities of a commercial implicit numerical tool, ABAQUS, were examined. In this chapter the squeezing of the rivet in a force controlled process was explained in detail. The most essential aspects of the numerical modeling of such a process were put forward. In the end, residual stress field and displacement field were obtained and finally, the results were compared with those predicted by other researches in the literature.

## 2.2 2-D Numerical model

The specimen analyzed herein is a single-lap joint. As stated before, single-lap joint is obtained by layering two sheets of material and then joining them by means of a fastener. Hence, the specimen consisted of three bodies. These were outer and inner plates which are made of 2024-T3 aluminum alloy and a universal head type 2117-T4 aluminum alloy rivet. The specimen geometry and rivet dimensions are presented in Figure 2.1.

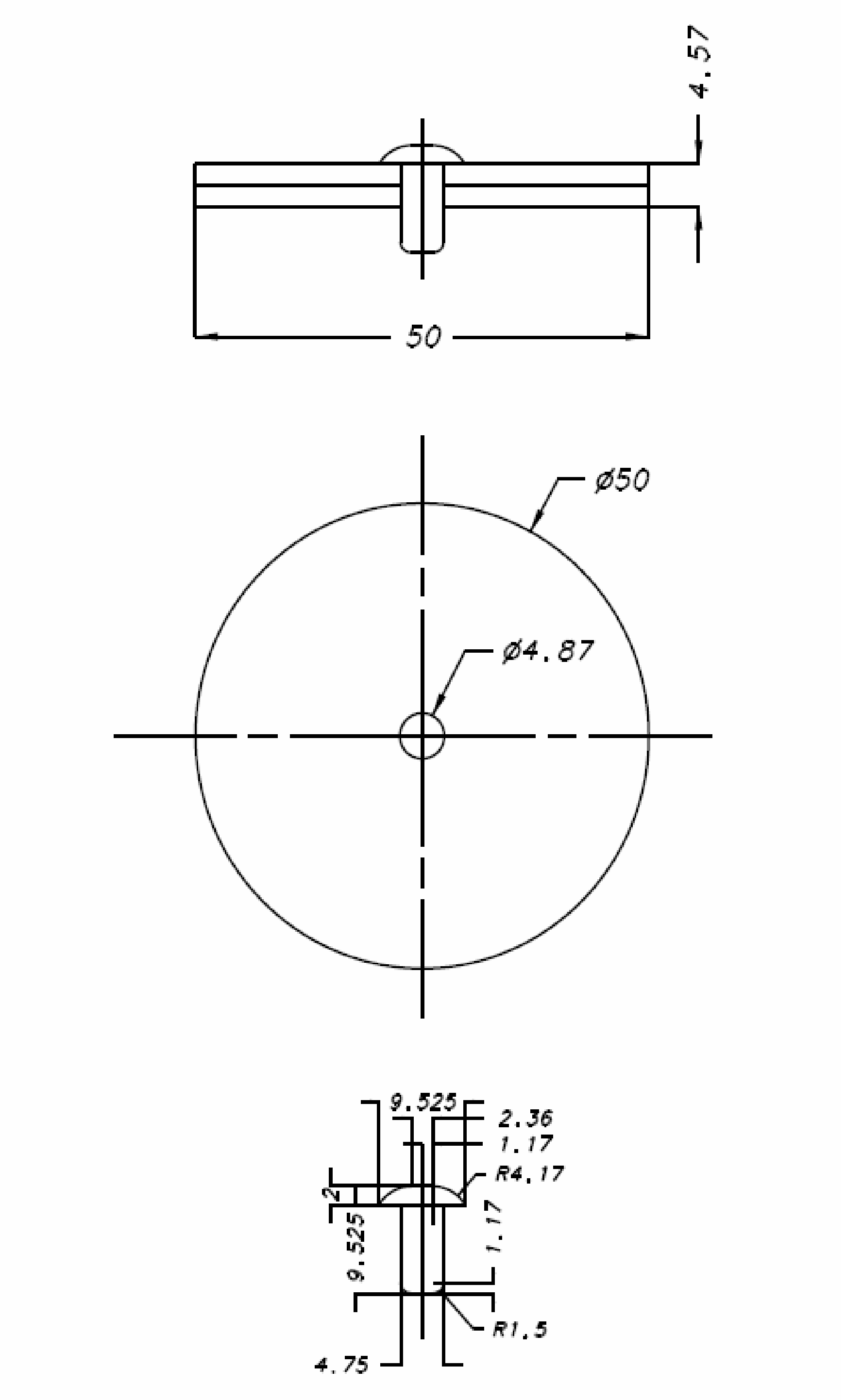

**Figure 2.1** Specimen geometry and rivet dimensions

Throughout the research nonlinearities arising from material properties were taken into consideration. Material properties of both the rivet and the metal plates were taken from the literature. Hardening properties of the rivet material was extracted through compression test on 2117-T4 billet samples and the data was presented in the form of equation 2.1 [1]. On the other hand, in order to obtain the material properties of 2024_T351 aluminum alloy plates uniaxial tensile tests were conducted then, the data was presented in the form of equation 2.2 [4]. Material properties of both the rivet and the plates are presented in Table 3.1.

$$\sigma = C\varepsilon^{n} \tag{2.1}$$

$$\sigma = A + B\varepsilon^{n} \tag{2.2}$$

**Table 2.1** Elastic and hardening properties of both the rivet and the plate material

| | **Material** | **Elastic Properties** | | **Hardening Parameters** | | |
|---|---|---|---|---|---|---|
| | | **E (GPa)** | **v** | **A (MPa)** | **B (MPa)** | **n** |
| **Plate** | Al 2024-T351 | 74 | 0.33 | 350 | 600 | 0.502 |
| | | | | | **C (MPa)** | **n** |
| **Rivet** | Al 2117-T4 | 71.7 | 0.33 | $0.02<\varepsilon_{true}<0.1$ | 544 | 0.23 |
| | | | | $0.1<\varepsilon_{true}<1$ | 551 | 0.15 |

Meshing the bodies that constitutes the whole assembly is a crucial step in finite element analysis. Creating an unnecessarily fine mesh results in consumption of time, whereas a coarse mesh can affect the analysis adversely and generates inaccurate results. For the sake of analyzing axisymmetrical model a 2-D quarter model was created as shown in Figure 2.2. The model consisted of two plates of equal thickness, rivet and the rigid bucking plate. Except the bucking bar all the bodies were modeled as deformable, the bucking bar is used as a rigid part. The deformable bodies were modeled with CAX4 4-node bilinear axisymmetric quadrilateral elements with reduced integration option was turned off. In ABAQUS/Standard the material response is evaluated at each integration points for each element. Although using full integration continuum elements can contribute to the accuracy of the problem considerably, this can affect the computational time of the model adversely.

Local mesh refinement was applied at locations where large deformations were expected. As a result, 13694 elements were generated on the entire assembly. In order to obtain finer meshes deformable bodies were sectioned into smaller sections. These sections were also used to represent contacting surfaces.

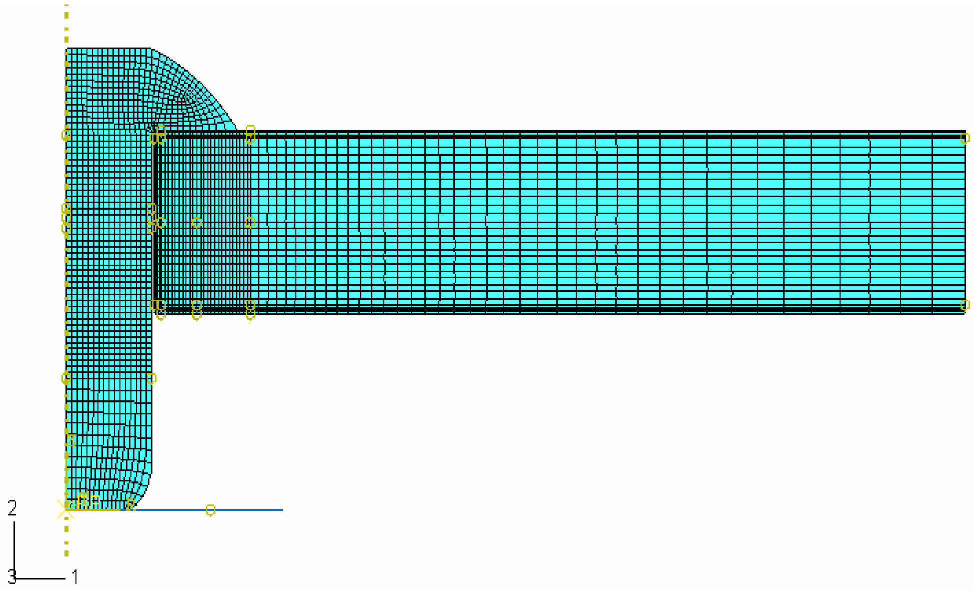

**Figure 2.2** Whole 2-D modelof rivet and plates with mesh

Riveting process was divided into two steps, in the first step the force was applied to the rigid bucking bar and the driven head of the rivet was formed in the second step the bucking bar was returned to its original position and the model was allowed to spring back. In the end, the actual residual stress field was obtained.

Besides including the nonlinearities arising from the material properties, geometric and surface interaction nonlinearities were also included in the model. Using master/slave contact algorithm with finite sliding option provided by ABAQUS the contacting edges were defined. The contact surfaces are defined between all deformable bodies as well as between the rivet and the bucking bar (Figure 2.3). Since the size of the contact surfaces increases the solution time largely, this section requires intensive care. As stated before, the sectioned surfaces were used to define the contact surfaces. By this way, the contact interfaces were minimized and considerable amount of time was saved. At all contact locations Coulomb friction model was assumed and a coefficient of friction of 0.2 was assigned [1, 4]. Since large deformations take place during riveting process geometric nonlinearities were included in the model by using the NLGEOM feature of the ABAQUS. This setting allows users to formulate large displacement problems.

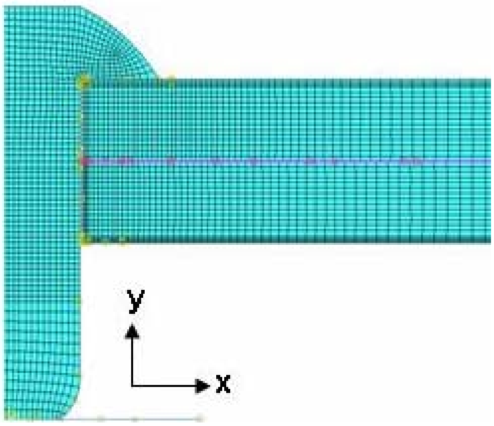

2.3 (a)

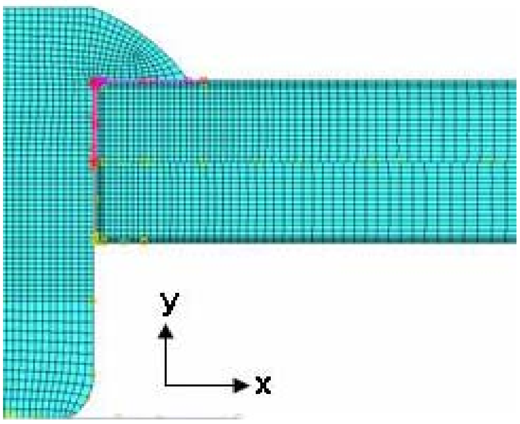

2.3 (b)

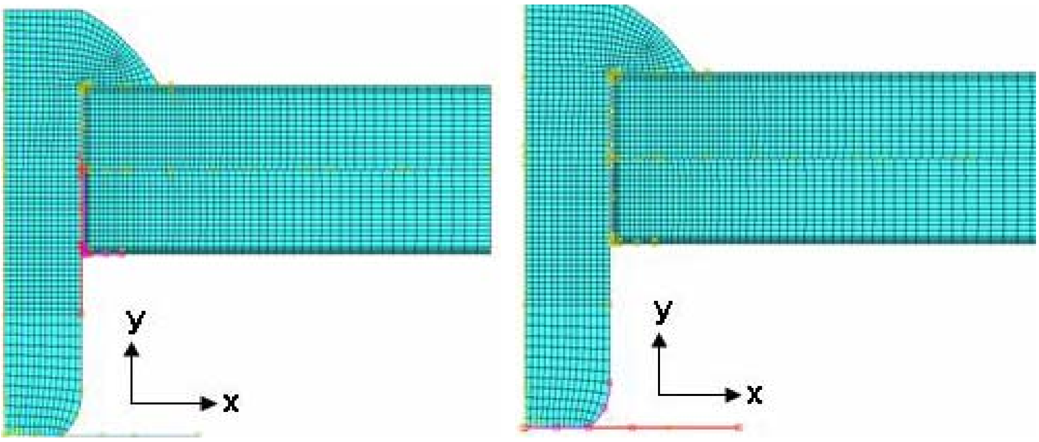

2.3 (c) 2.3 (d)

**Figure 2.3** Contact surface definitions (a) outer plate/inner plate (b) rivet/outer plate (c) rivet/inner plate (d) rivet/rigid tool

Boundary conditions were applied to all deformable bodies as well as the rigid body. In ABAQUS, boundary condition of a rigid body can only be applied through reference points and a rigid body receives only one reference point. So as to apply the boundary condition on the analytical rigid body, a reference point was generated on the axis of symmetry. The squeezing force and the displacement constraint that prevents the rigid body motions were applied via this point. The rigid body was constrained in x direction and the rotation degree of freedom around z axis was prevented. For both of the metal plates, similar boundary conditions were applied. Translation in x (radial) direction was constrained for all nodes on the remote edge. In order to prevent rigid body motion, the top node of the outer plate and the bottom node of the inner plate at the remote edge were also constrained in y (axial) direction, other nodes at this edge were left free to move in y direction. Symmetry boundary conditions were applied on the axis of symmetry of the rivet and the nodes on the manufactured head of the rivet was fixed. The applied boundary condition was shown schematically in Figure 2.4.

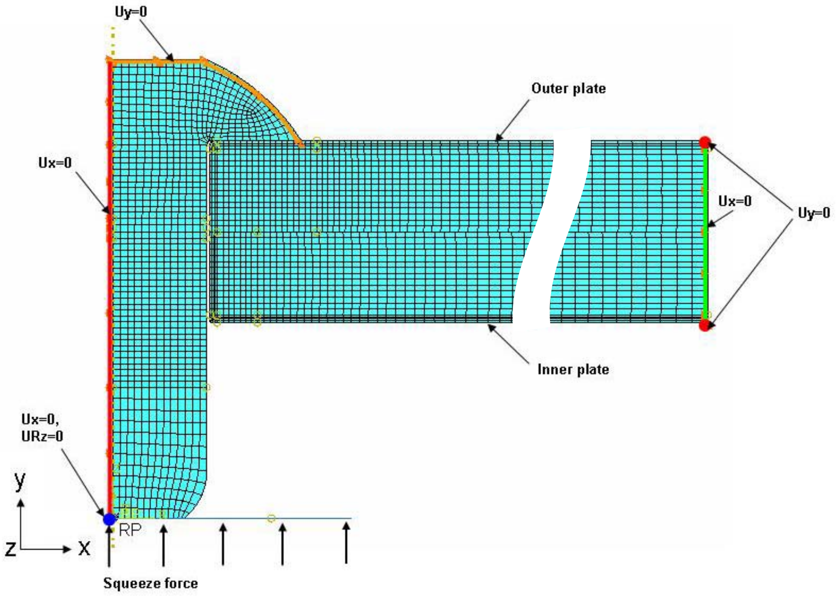

**Figure 2.4** Schematic representation of the applied boundary conditions

## 2.3 Validation of the 2-D model

The final rivet driven head diameter and the final rivet driven head height obtained by numerical simulation were recorded for two different squeeze force values. These values were compared with those obtained experimentally in [1]. By this way the model was validated. Deformed shape parameters and deformed meshes after unloading under different loading conditions are presented in Figure 2.5. The obtained numerical values and the data used to compare the results are tabulated (Table 2.2). In addition a convergence check study was carried out by changing the overall mesh density of the numerical model. The model was meshed using coarse, medium and fine mesh densities these models had 793, 2033, 13694 elements, respectively. Again the driven rivet head final deformation values are shown in Table 2.2.

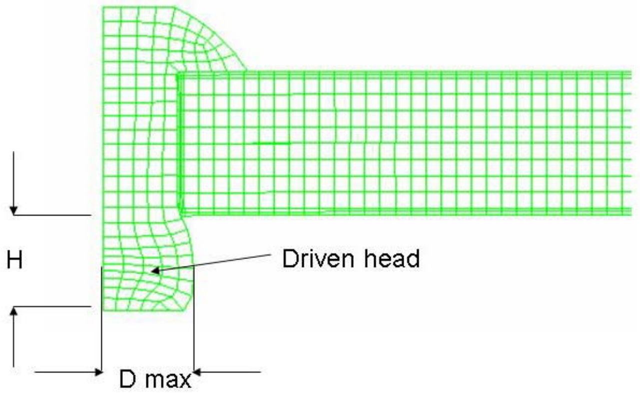
H
Driven head
D max

2.5 (a)

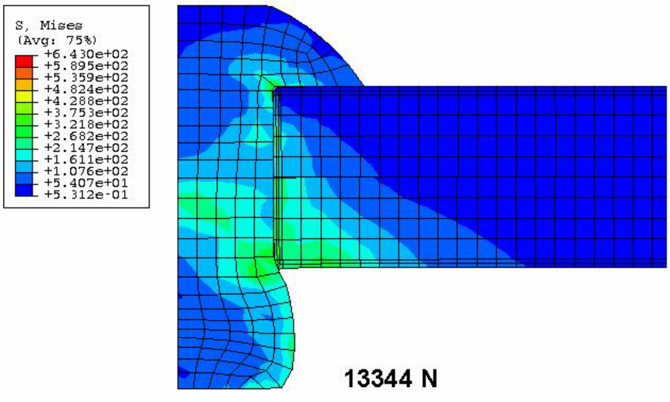
S, Mises
(Avg: 75%)
+6.430e+02
+5.895e+02
+5.359e+02
+4.824e+02
+4.288e+02
+3.753e+02
+3.218e+02
+2.682e+02
+2.147e+02
+1.611e+02
+1.076e+02
+5.407e+01
+5.312e-01
13344 N

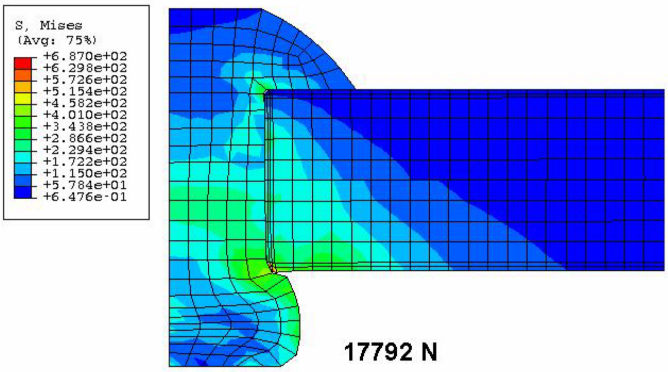
S, Mises
(Avg: 75%)
+6.870e+02
+6.298e+02
+5.726e+02
+5.154e+02
+4.582e+02
+4.010e+02
+3.438e+02
+2.866e+02
+2.294e+02
+1.722e+02
+1.150e+02
+5.784e+01
+6.476e-01
17792 N

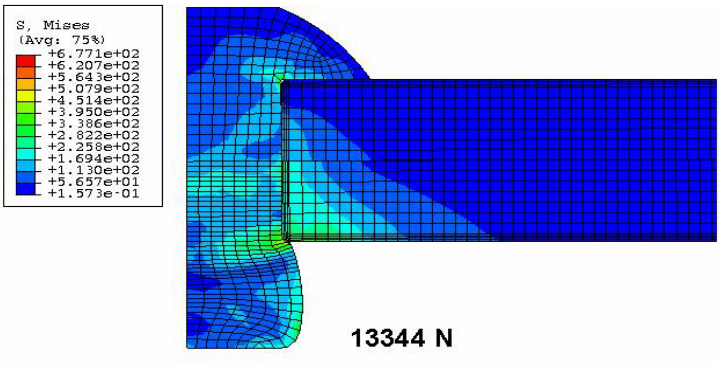
S, Mises
(Avg: 75%)
+6.771e+02
+6.207e+02
+5.643e+02
+5.079e+02
+4.514e+02
+3.950e+02
+3.386e+02
+2.822e+02
+2.258e+02
+1.694e+02
+1.130e+02
+5.657e+01
+1.573e-01
13344 N

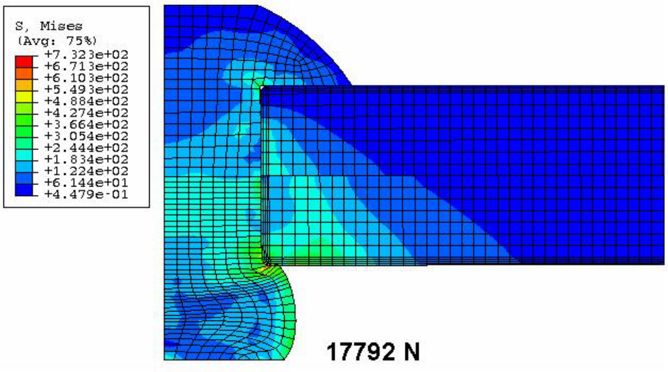
S, Mises
(Avg: 75%)
+7.323e+02
+6.713e+02
+6.103e+02
+5.493e+02
+4.884e+02
+4.274e+02
+3.664e+02
+3.054e+02
+2.444e+02
+1.834e+02
+1.224e+02
+6.144e+01
+4.479e-01
17792 N

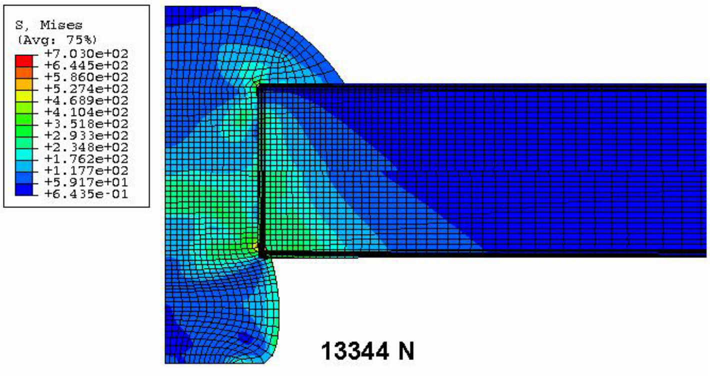
S, Mises
(Avg: 75%)
+7.030e+02
+6.445e+02
+5.860e+02
+5.274e+02
+4.689e+02
+4.104e+02
+3.518e+02
+2.933e+02
+2.348e+02
+1.762e+02
+1.177e+02
+5.917e+01
+6.435e-01
13344 N

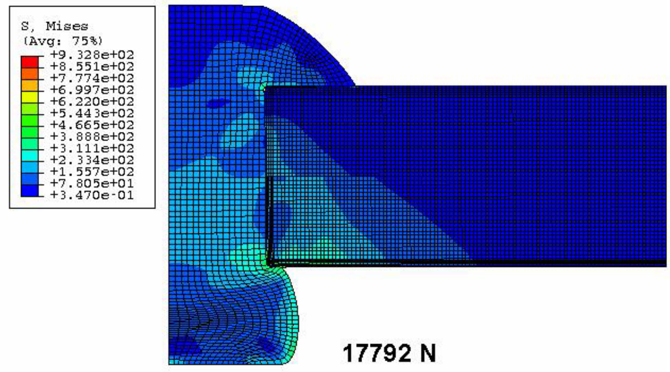

2.5 (b)

**Figure 2.5** (a) Deformed shape parameters (b) Deformed meshes and von Mises stress distribution under different loading conditions for 2-D axisymmetrical model with different mesh sizes

**Table 2.2** Table of comparison of the rivet deformations obtained by numerical analysis and the experimental values

| ***Squeeze Force*** | | ***Dmax (mm) FEM*** | ***Dmax Expt.*** | ***% Error*** | ***H (mm) FEM*** | ***H Expt.*** | ***% Error*** |
|---|---|---|---|---|---|---|---|
| **13344 N (3000 lbs)** | **Literature [1]** | 5.977 | 6.0452 | 1.1 | 3.053 | 3.1496 | 3.1 |
| | **Coarse mesh** | 5.932 | | 1.9 | 3.062 | | 2.8 |
| | **Medium mesh** | 5.969 | | 1.3 | 3.073 | | 2.4 |
| | **Fine mesh** | 5.994 | | 0.8 | 3.095 | | 1.7 |
| **17792 N (4000 lbs)** | **Literature [1]** | 6.464 | 6.5786 | 1.7 | 2.537 | 2.5654 | 1.1 |
| | **Coarse mesh** | 6.676 | | 1.5 | 2.451 | | 4.5 |
| | **Medium mesh** | 6.647 | | 1.0 | 2.473 | | 3.6 |
| | **Fine mesh** | 6.57 | | 0.1 | 2.529 | | 1.4 |

The data obtained by finite element method is in good agreement with those taken from the literature. The maximum error in the rivet deformed diameter, which was encountered in coarsely meshed model, is % 4.5. For the driven head height maximum % 1.9 error was encountered again in the coarsely meshed model. On the other hand, these values decreases significantly as the mesh density increases and they become % 1.4 and % 0.8, respectively. Error in Table2.2 is defined as follows:

$$\% \text{ Error} = (Dmax_{Exp} - Dmax_{FEM}) \backslash Dmax_{Exp} x100 \qquad (2.3)$$

Comparisons of the models in Figure 2.5 reveal that as the numbers of the elements are increased from very coarse mesh to fine mesh the maximum stress values are also increased. Because, stress concentration locations, such as corners, sharp edges, necessitate smallest possible elements to be used around them. On the other hand, for the regions where relatively moderate stresses are formed, stress levels do not differ much. In addition, in the same Figure, stress distributions across the interface between the plates are not continuous. At first glance, this may made us to think that the model does not converge. However, the discontinuity on von mises stress distribution is due to the contact condition on the interface. As a result of contact boundary condition, radial and tangential stresses distributions differ for two plates and hence, the resulting von mises stress distributions seem discontinuous.

In further validating the model, force-deflection diagram of the interface between the tool (rigid bucking bar) and the workpiece (driven head of the rivet) was compared with those predicted in the literature [1]. Figure 2.6 depicts the results of the finite element analysis, inspection of the curves reveal that the result of the current study is in good agreement with the literature. In the second stage of the riveting process in which the rigid bucking bar was retracted to the original position the reaction force decreases, as expected. When it becomes zero, the displacement value shows the final driven rivet head height.

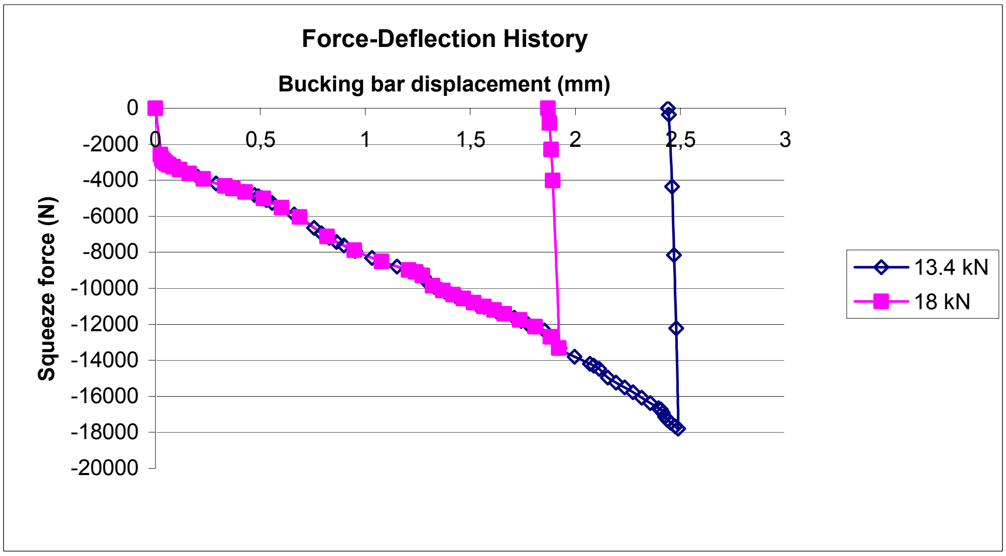

**Figure 2.6** Force displacement history with P=13.4 kN and P=18 kN superimposed on each other

## 2.4 3-D Numerical model

A 3-D finite element model of the same specimen configuration analyzed in Chapter 2.1 was generated in ABAQUS/Standard. The aim is to analyze non-axisymmetrical riveting process parameters in subsequent chapters on a similar 3-D numerical model. Material properties of the rivet and the plates are the same as those which was used for the axisymmetrical model (Table 2.1). Again tabular input of the stress and strain data was provided in the program.

A quarter symmetry model which had 23182 elements and 35746 nodes was generated using ABAQUS with eight noded C3D8R reduced integration solid elements. Three deformable bodies namely inner sheet, outer sheet and rivet and one rigid bucking bar were included in the model. Figure 2.7 depicts the joint assembly and the mesh used throughout the analysis. In order to get a convergent model local mesh refinement was applied where the largest deformation takes place. By this way considerable amount of time was saved.

Here element size of the rivet model is very critical. Since riveting is a highly nonlinear process, large distortions may occur in the elements. As a result, solution may not converge.

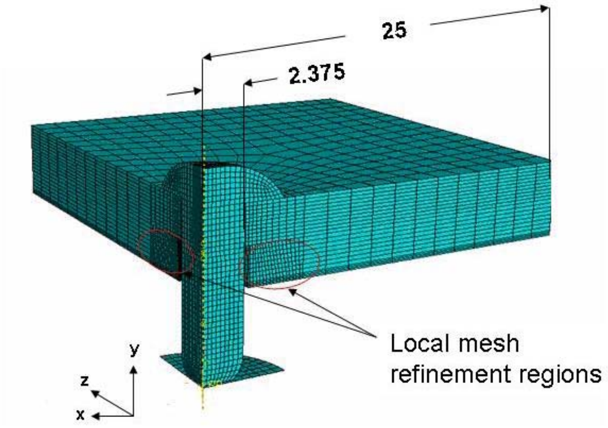

**Figure 2.7** Whole 3-D quarter symmetry model with mesh

The interactions of the bodies were modeled using Coulomb friction model and a coefficient of friction of 0.2 was used as before. Deformable bodies were sectioned such that optimum contact surface areas were obtained. Except the contact interface between the inner plate and the outer plate, finite sliding formulation was set. On the other hand small sliding formulation was used between the plates, by this way surface penetrations were minimized. Selection of the master and slave surfaces between the interaction regions were summarized in Figure 2.8.

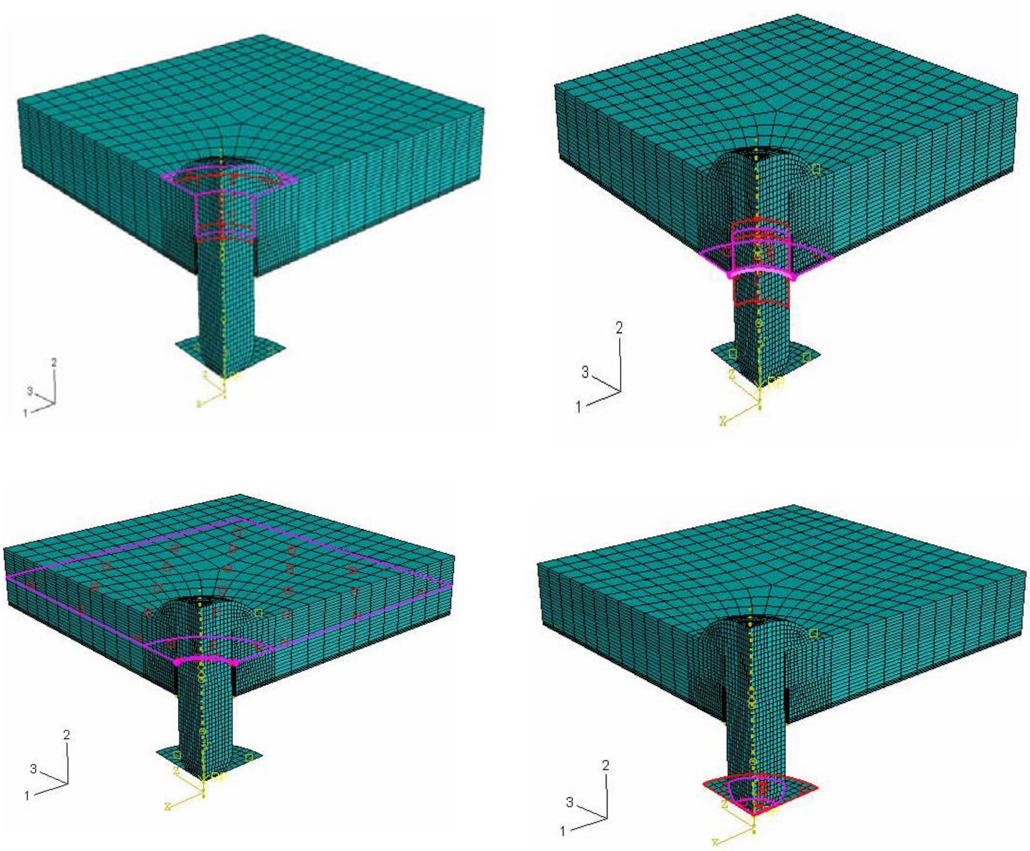

**Figure 2.8** Contact surfaces between the bodies

The constraint applied by the tool that constrains head of the rivet during the riveting process was simulated by means of boundary conditions. Free surfaces of the plates were constrained in x and z direction besides, free edges on the top and bottom were constrained in y direction so as to prevent rigid body motion. Squeezing force was applied to the rigid bucking bar. The magnitudes of squeeze forces were the same as in the case of axisymmetrical model. The whole analysis was performed in two steps in order to obtain the actual residual stress field after riveting process. Therefore, the rigid bucking bar was retracted to the original position at the end of squeezing stage of the riveting process by means of a displacement boundary condition. Symmetry boundary conditions were applied to the symmetry surfaces. Displacements of the nodes were constrained in the direction perpendicular to the surface and the rotations were constrained in the other two directions. Boundary conditions were depicted in Figure 2.9.

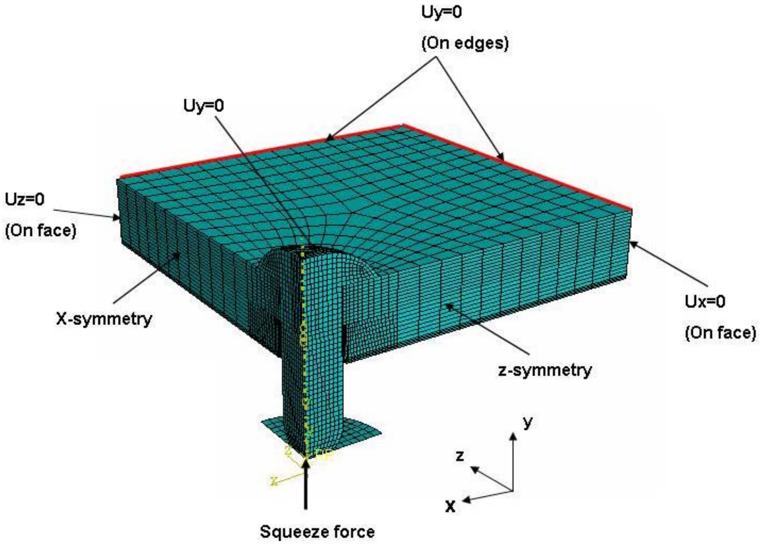

**Figure 2.9** Boundary conditions of the 3-D quarter symmetrical model

## 2.5 Validation of the 3-D model

Validation of the current three dimensional simulation was performed based on the results obtained in 2-D axisymmetrical model. Since the two dimensional model was found to be consistent to that reported by Szolwinski and Farris [1], it can also be a good reference for the 3-D study. Three criteria were used to compare the results of the 2-D and 3-D model. The von Mises and tangential stress variation along two selected paths in both of the plates were compared. Also driven head height and diameter of the driven head after riveting process were tabulated. The analysis was carried out for two different squeeze force values (13.4 kN and 18 kN), as before, and result were compared with those predicted by the 2-D axisymmetrical model and by simulation conducted in the literature [1]. Finally force-displacement history of both model were depicted.

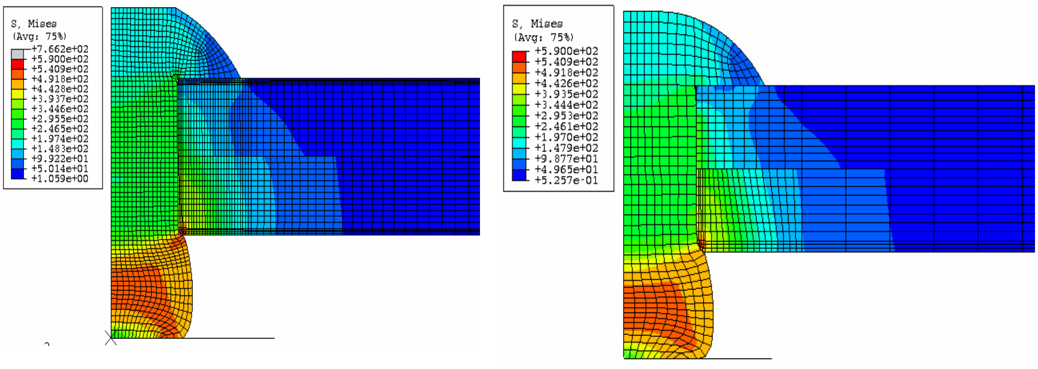

**Figure 2.10** Von Mises stress contours before unloading of 2-D model(left) and 3-D model (right) for 13.4 kN

Figure 2.10 combined with Figure 2.11 showed that the stress state in both of the models were essentially in agreement. In Figure 2.10, although the stress contours were similar, maximum von Mises stress value of 2-D model differed from the one predicted by the 3-D model. The reason for this mismatch is inherent in finite element analysis. The problem arises from excessive distortion of the mesh used throughout the analysis. When the element shape for a particular location differs from the original shape much, numerical inaccuracy around that region begins. In order to overcome this problem finer mesh can be used for the whole model or local mesh refinement can be applied. On the other hand, the computational time of the problem is affected by number of elements used in the model considerably so, a compromise is needed between the numerical accuracy and the computational time. In Figure 2.11, it is observed that in general 2-D model predicted higher stress values than those of the 3-D model. This is due to the fact that having smaller elements around critical regions 2-D model has the ability to model stress state more accurately. If the high stress regions are omitted rest of the stress contours have similar stress levels for both of the models.

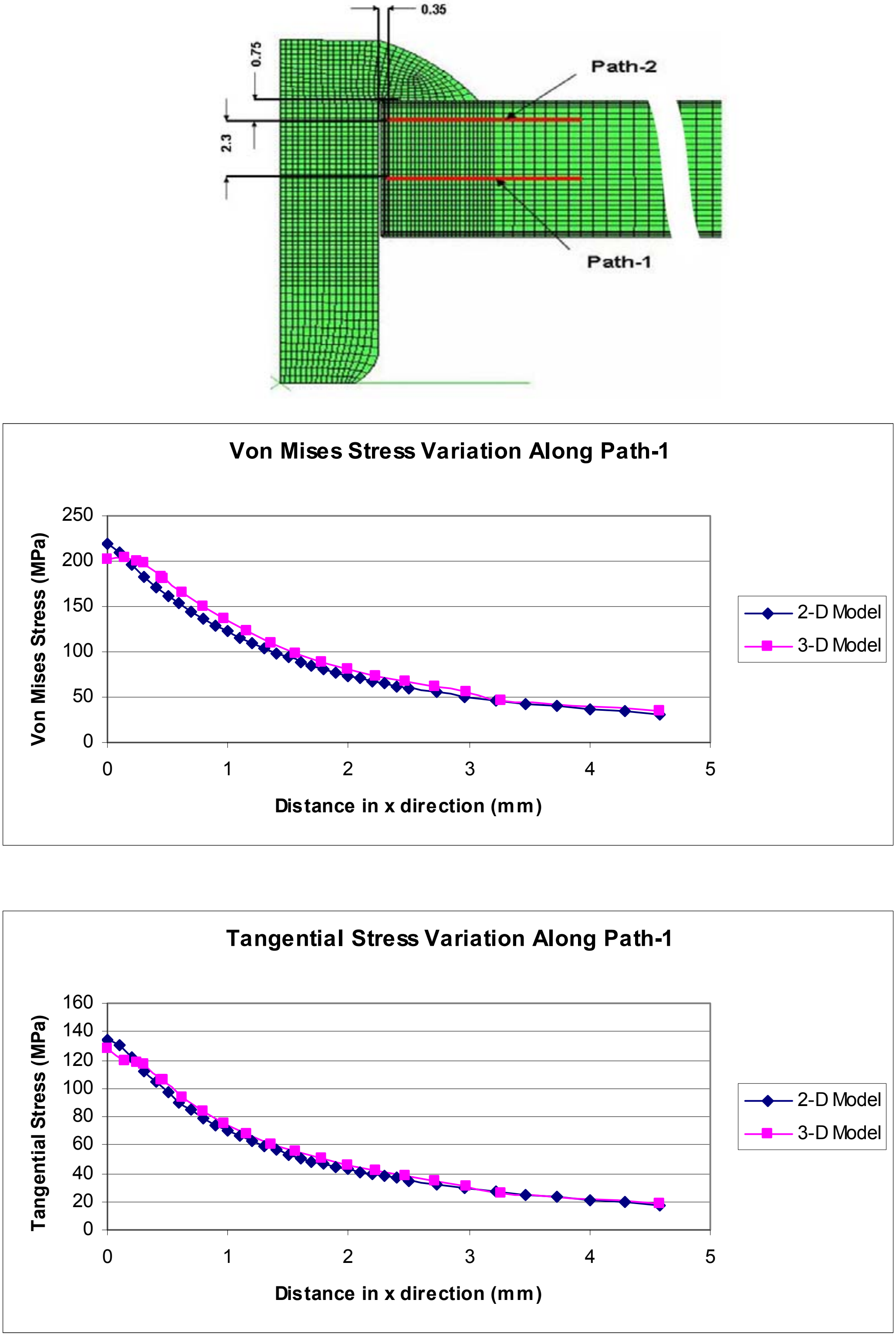
0.35
0.75
2.3
Path-2
Path-1
Von Mises Stress Variation Along Path-1
Von Mises Stress (MPa)
250
200
150
100
50
0
0
1
2
3
4
5
Distance in x direction (mm)
2-D Model
3-D Model
Tangential Stress Variation Along Path-1
Tangential Stress (MPa)
160
140
120
100
80
60
40
20
0
0
1
2
3
4
5
Distance in x direction (mm)
2-D Model
3-D Model

2.11 (a)

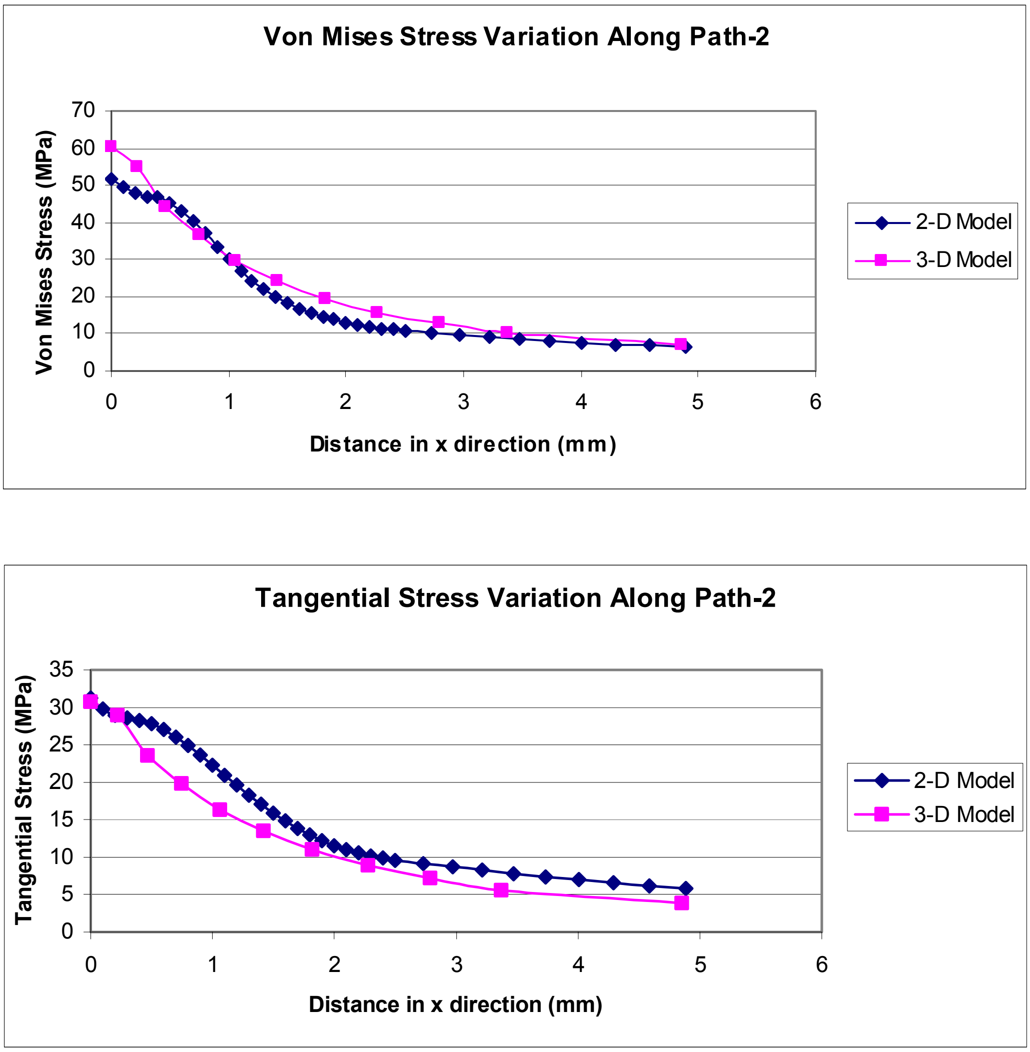

2.11 (b)

**Figure 2.11** Comparison of von Mises stress and tangential stress along (a) path-1 and (b) path-2

Deformation of the driven head which is given in Table 2.3 was compared with not only the 2-D model results but also with those predicted by Szolwinski et al.. Again the values were found to be in agreement with a small error which is reasonable. It should be noted 2-D axisymmetrical model approximated to the experimental results better than the 3-D model. The reason for that can be the fact that many elements are used on the cross-section for the axisymmetrical problem.

**Table 2.3** Table of comparison of the experimental rivet deformations with deformations predicted by numerical analysis

| *Squeeze Force* | | *Dmax (mm) FEM* | *Dmax Expt.* | *% Diff.* | *H (mm) FEM* | *H Expt.* | *% Diff* |
|---|---|---|---|---|---|---|---|
| **13344 N (3000 lbs)** | **Literature** | 5.977 | 6.0452 | 1.1 | 3.053 | 3.1496 | 3.1 |
| | **2-D model** | 5.994 | | 0.8 | 3.095 | | 1.7 |
| | **3-D model** | 6.024 | | 0.4 | 3.08 | | 2.2 |
| **17792 N (4000 lbs)** | **Literature** | 6.464 | 6.5786 | 1.7 | 2.537 | 2.5654 | 1.1 |
| | **2-D model** | 6.57 | | 0.1 | 2.529 | | 1.4 |
| | **3-D model** | 6.61 | | 0.5 | 2.496 | | 2.7 |

In further validating the model, the force deflection histories of both of the models (2-D and 3-D models) were superimposed onto each other. The resulting plots were consistent with each other denoting the similarity of the both of the simulations. Force-deflection histories for two different loading conditions were presented in Figure 2.12.

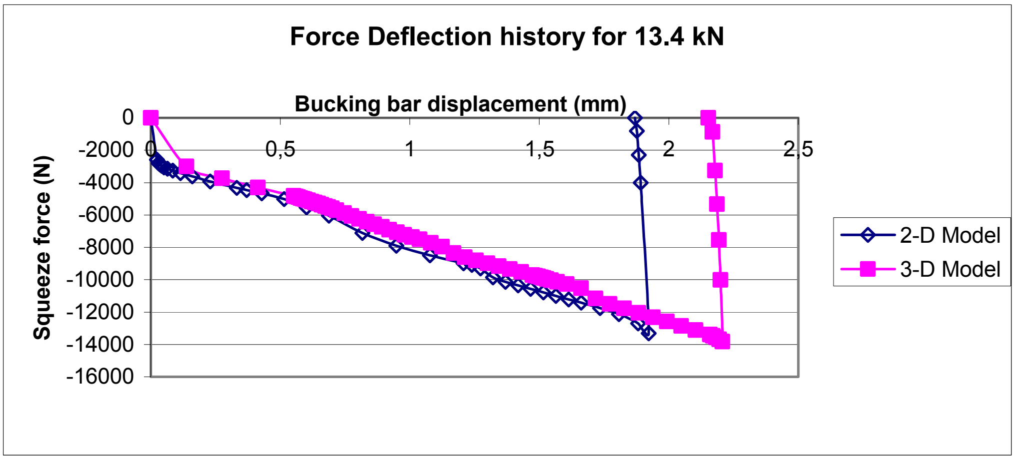

(a)

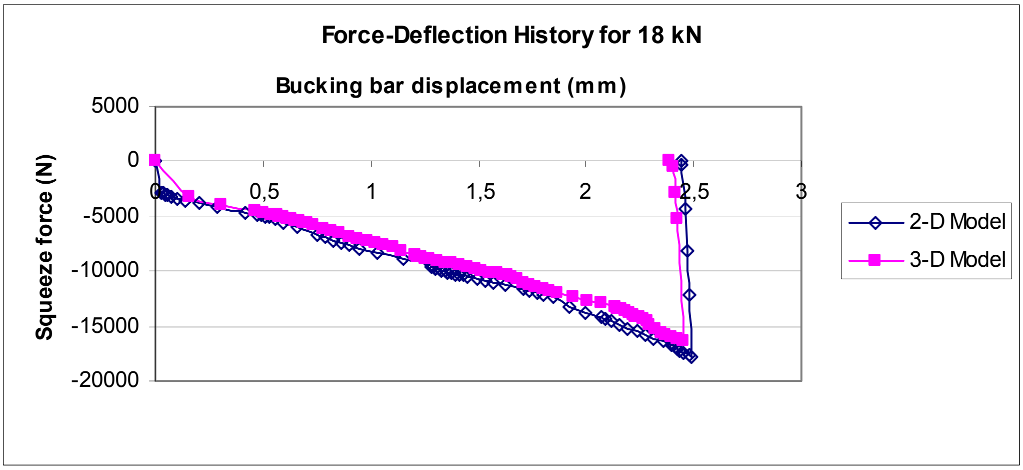

(b)

Figure 2.12 Comparison of force-deflection history for (a) 13.4 kN and (b) 18 kN

In this chapter, a 3-D numerical model of riveting process was generated. The validation of the model was performed by comparing this model with the 2-D model of previous section. In addition, deformation values obtained from the literature was used again for validation purpose. In the end, capability of the ABAQUS in modeling such a complex 3-D nonlinear problem was proved.

# CHAPTER 3

# EFFECT OF CLEARANCE ON THE RESIDUAL STRESS IN RIVETING PROCESS

## 3.1 Introduction

In the previous chapter it was shown that the finite element model generated is viable in terms of analyzing the riveting process. With a high degree of confidence in the model established, now it is possible to draw conclusions about the potential impact of the riveting process parameters on the final residual stress field induced on the rivet and the plates. In this chapter, the focus will be on the effect of clearance, which exist between the rivet shank and the hole surface, on the residual stress field. In light of the data acquired on the 2D model, the results will be interpreted in terms of their potential influence on fatigue life.

## 3.2 Model definition

In performing this analysis, the aim was to capture the effect of hole clearance and hence, some idealizations on the present model was done. The rivet to be analyzed was assumed to be sufficiently away from the other rivets and the plate edges that may interfere with the residual stress field around the rivet. The same 2D axisymmetrical model of the previous chapter was used for this study. Holes of the both plates were modeled as concentrical and of the same size. Also the same process parameters were used. Hence, an axisymmetrical distribution of the stress field was obtained.

## 3.3 Model results

Before interpreting the model results, it should be noted that it is the hoop stress that plays a considerable role on the propagation of the fatigue cracks either on the hole edge or on the faying surface. Figure 3.1 shows the deformed plot and the contours of the residual hoop stress for the whole assembly for a range of hole clearance value.

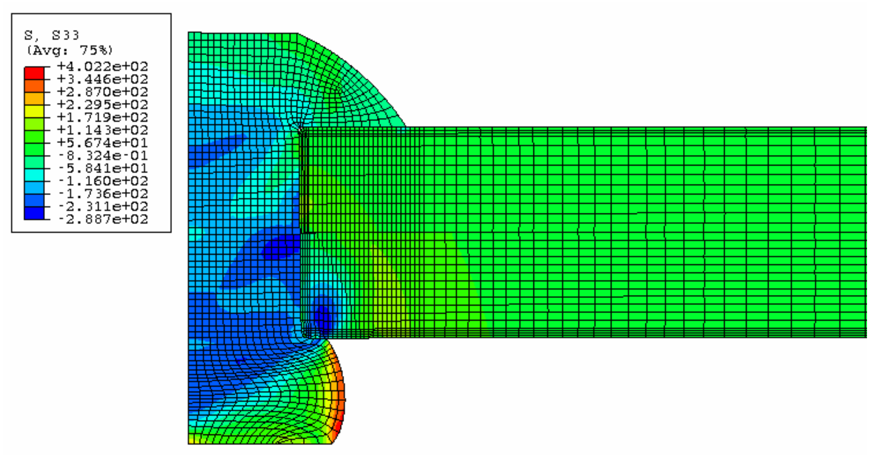

3.1 (a)

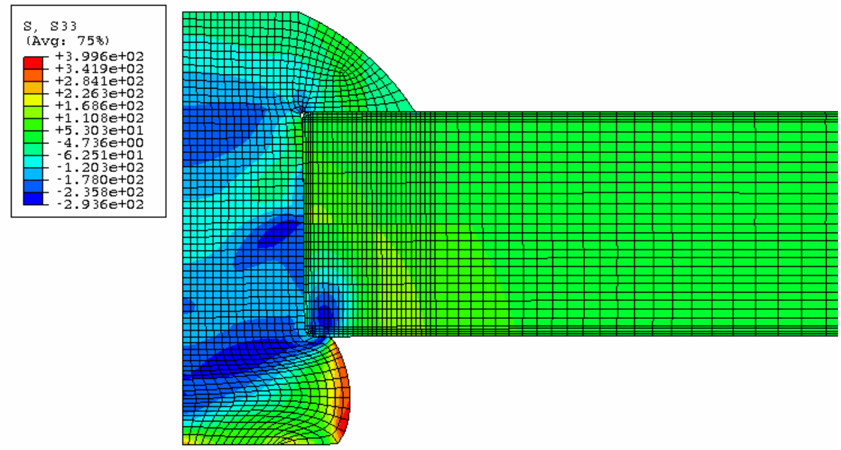

3.1 (b)

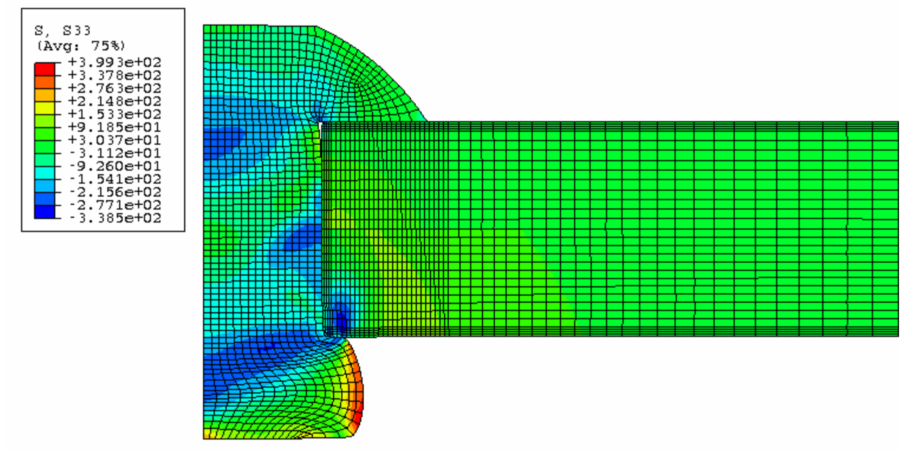

3.1.(c)

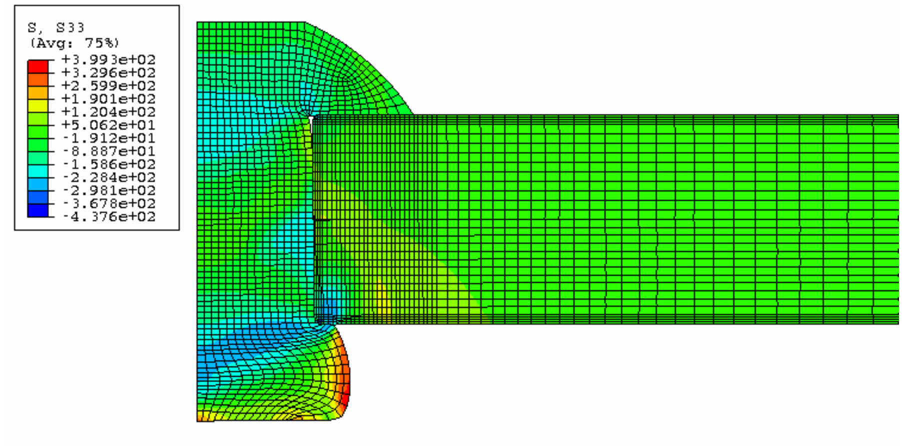

3.1 (d)

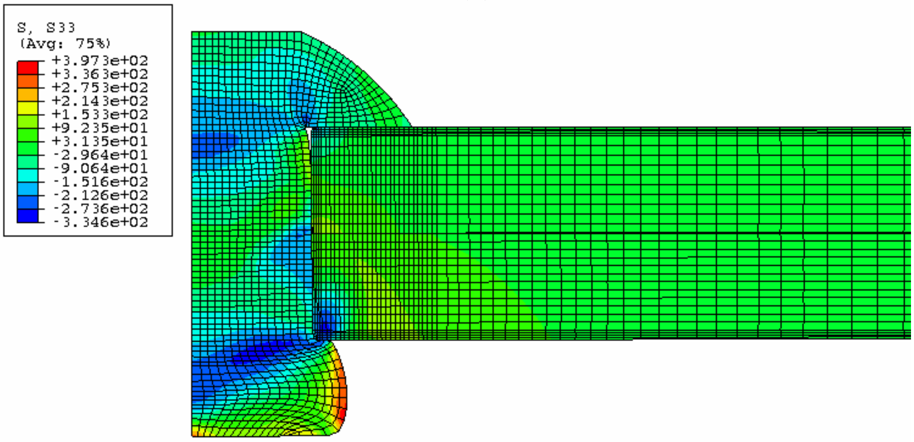

3.1 (e)

**Figure 3.1** Deformed configurations and residual hoop stress contours for different clearance values (a) 0.055 mm, (b) 0.090 mm, (c) 0.135 mm, (d) 0.180 mm and (e) 0.210 mm

The stress contours in these plots clearly show the stress concentration locations. In comparing the contour plots of Figure 3.1, it can be seen that the changes in the clearance affects the residual stress field considerably. Another point that stands out is the presence of a compressive residual hoop stress zone at the hole edge near the driven head. The nature of this compressive hoop stress zone will be examined later on. Moreover, the stress variations along a number of paths were drawn in Figure 3.2 with the goal of demonstrating the residual stress variation in corresponding directions.

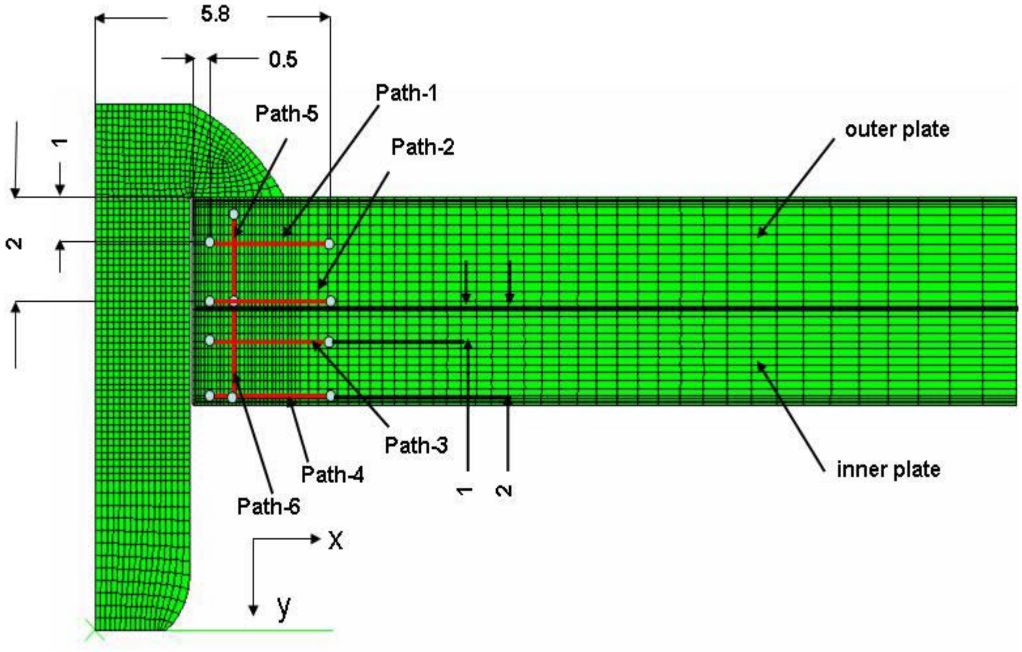

3.2 (a)

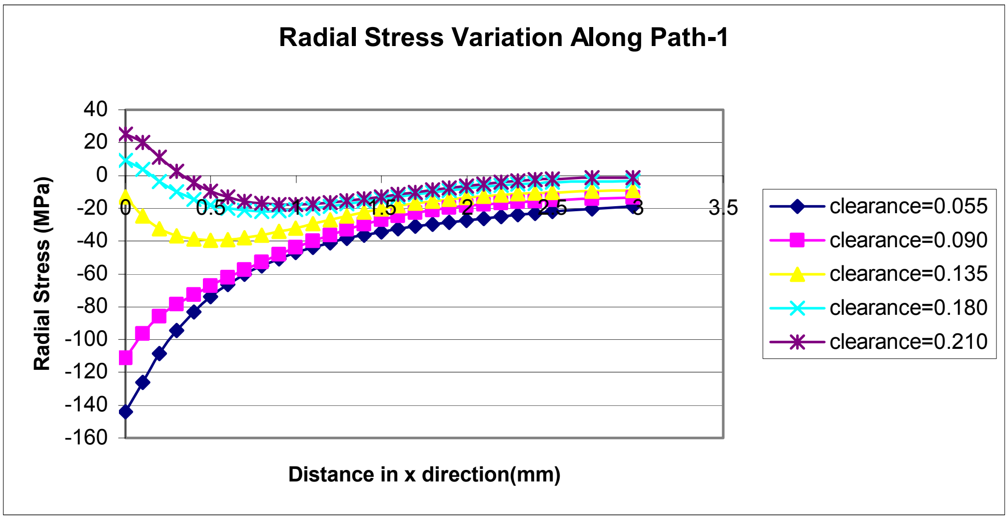
Radial Stress Variation Along Path-1
Radial Stress (MPa)
40
20
0
-20
-40
-60
-80
-100
-120
-140
-160
0
0.5
1
1.5
2
2.5
3
3.5
Distance in x direction(mm)
clearance=0.055
clearance=0.090
clearance=0.135
clearance=0.180
clearance=0.210

3.2 (b)

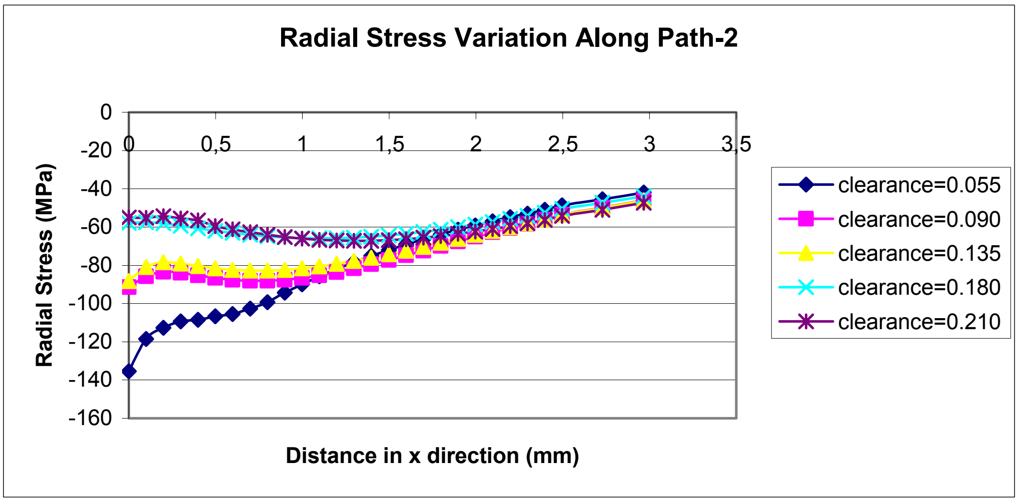
Radial Stress Variation Along Path-2
Radial Stress (MPa)
0
-20
-40
-60
-80
-100
-120
-140
-160
0
0,5
1
1,5
2
2,5
3
3,5
Distance in x direction (mm)
clearance=0.055
clearance=0.090
clearance=0.135
clearance=0.180
clearance=0.210

3.2 (c)

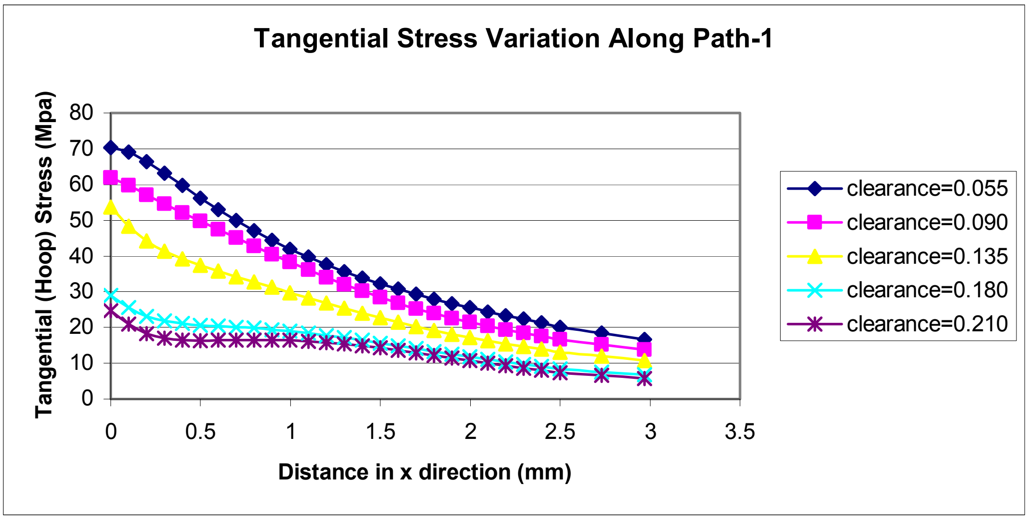
Tangential Stress Variation Along Path-1
Tangential (Hoop) Stress (Mpa)
80
70
60
50
40
30
20
10
0
0
0.5
1
1.5
2
2.5
3
3.5
Distance in x direction (mm)
clearance=0.055
clearance=0.090
clearance=0.135
clearance=0.180
clearance=0.210

3.2 (d)

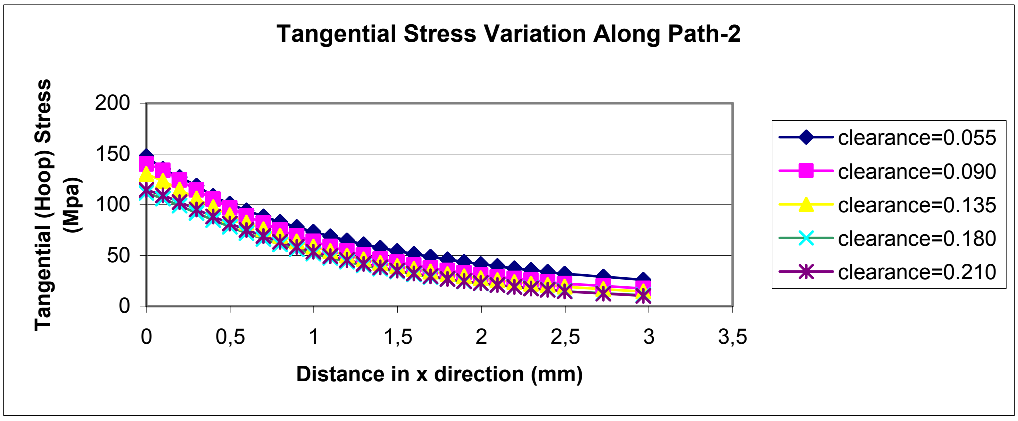
Tangential Stress Variation Along Path-2
Tangential (Hoop) Stress (Mpa)
200
150
100
50
0
0
0,5
1
1,5
2
2,5
3
3,5
Distance in x direction (mm)
clearance=0.055
clearance=0.090
clearance=0.135
clearance=0.180
clearance=0.210

3.2 (e)

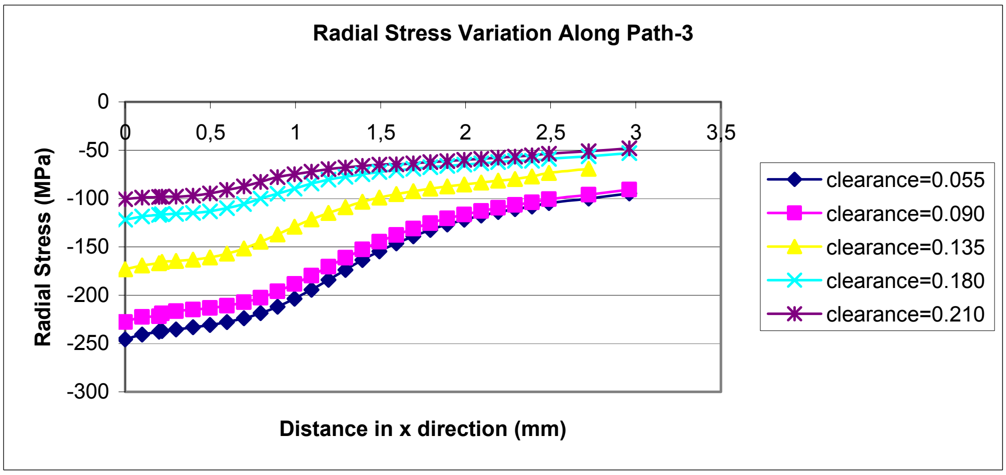
Radial Stress Variation Along Path-3
Radial Stress (MPa)
0
-50
-100
-150
-200
-250
-300
0
0,5
1
1,5
2
2,5
3
3,5
Distance in x direction (mm)
clearance=0.055
clearance=0.090
clearance=0.135
clearance=0.180
clearance=0.210

3.2 (f)

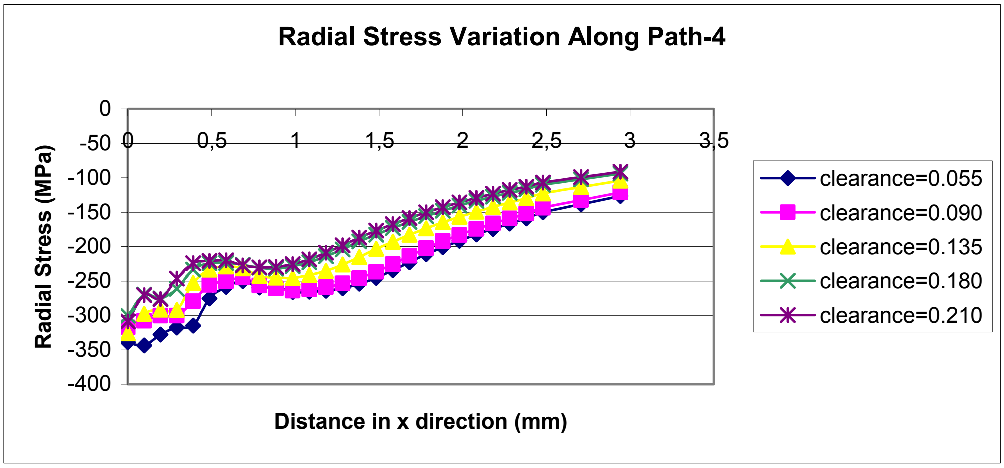
Radial Stress Variation Along Path-4
Radial Stress (MPa)
0
-50
-100
-150
-200
-250
-300
-350
-400
0
0,5
1
1,5
2
2,5
3
3,5
Distance in x direction (mm)
clearance=0.055
clearance=0.090
clearance=0.135
clearance=0.180
clearance=0.210

3.2 (g)

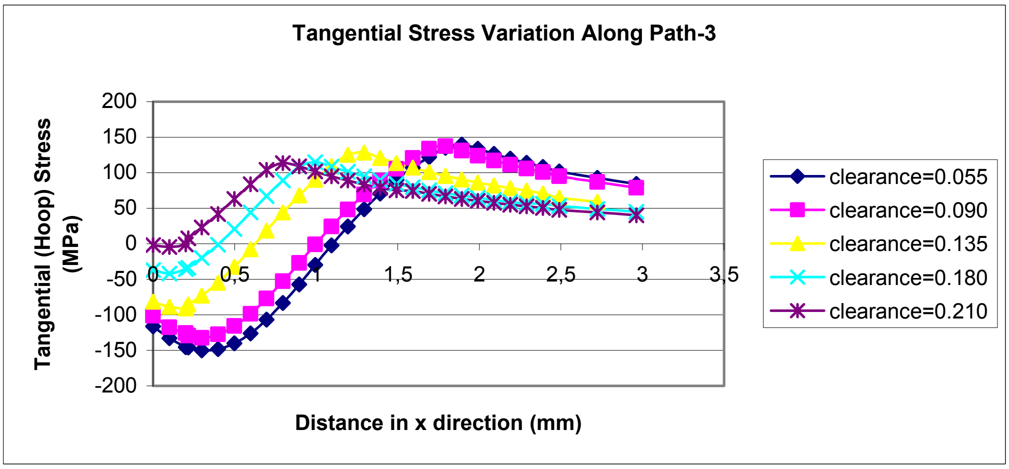
Tangential Stress Variation Along Path-3
Tangential (Hoop) Stress (MPa)
200
150
100
50
0
-50
-100
-150
-200
0
0,5
1
1,5
2
2,5
3
3,5
Distance in x direction (mm)
clearance=0.055
clearance=0.090
clearance=0.135
clearance=0.180
clearance=0.210

3.2 (h)

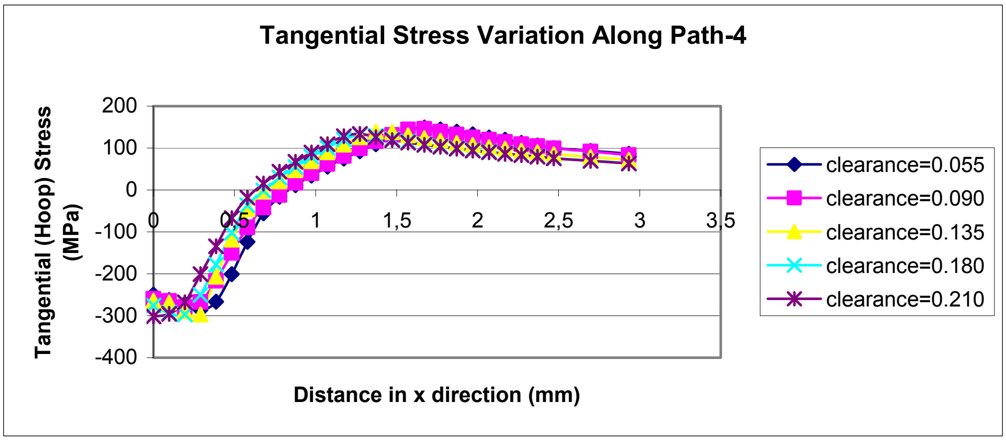
Tangential Stress Variation Along Path-4
Tangential (Hoop) Stress (MPa)
200
100
0
-100
-200
-300
-400
0
0,5
1
1,5
2
2,5
3
3,5
Distance in x direction (mm)
clearance=0.055
clearance=0.090
clearance=0.135
clearance=0.180
clearance=0.210

3.2 (i)

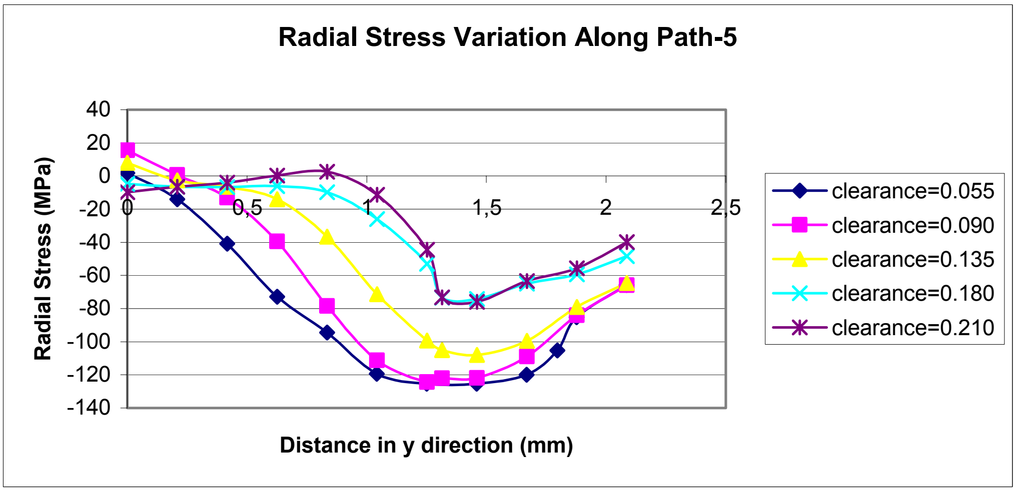
Radial Stress Variation Along Path-5
Radial Stress (MPa)
40
20
0
-20
-40
-60
-80
-100
-120
-140
0
0,5
1
1,5
2
2,5
Distance in y direction (mm)
clearance=0.055
clearance=0.090
clearance=0.135
clearance=0.180
clearance=0.210

3.2 (j)

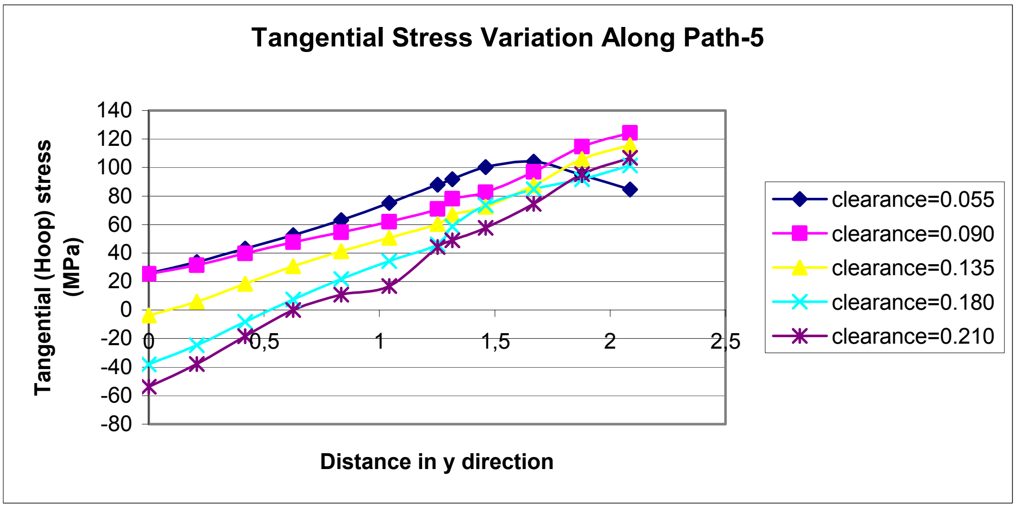
Tangential Stress Variation Along Path-5
Tangential (Hoop) stress (MPa)
140
120
100
80
60
40
20
0
-20
-40
-60
-80
0
0,5
1
1,5
2
2,5
Distance in y direction
clearance=0.055
clearance=0.090
clearance=0.135
clearance=0.180
clearance=0.210

3.2 (k)

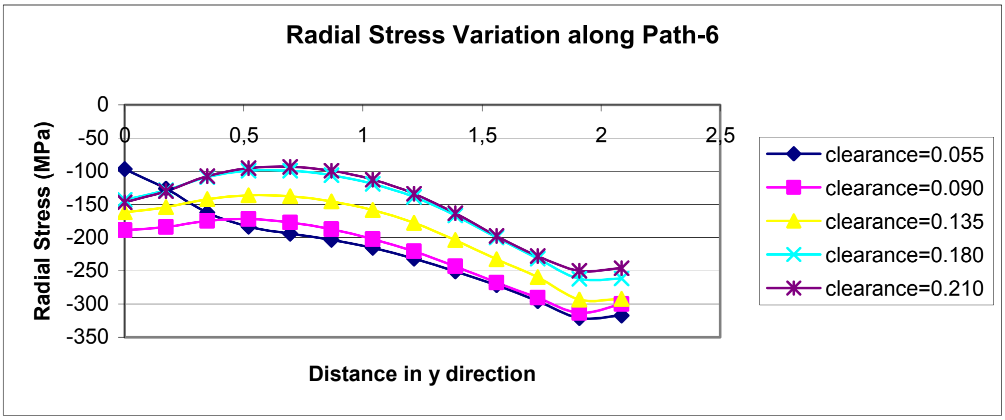
Radial Stress Variation along Path-6
Radial Stress (MPa)
0
-50
-100
-150
-200
-250
-300
-350
0
0,5
1
1,5
2
2,5
Distance in y direction
clearance=0.055
clearance=0.090
clearance=0.135
clearance=0.180
clearance=0.210

3.2 (l)

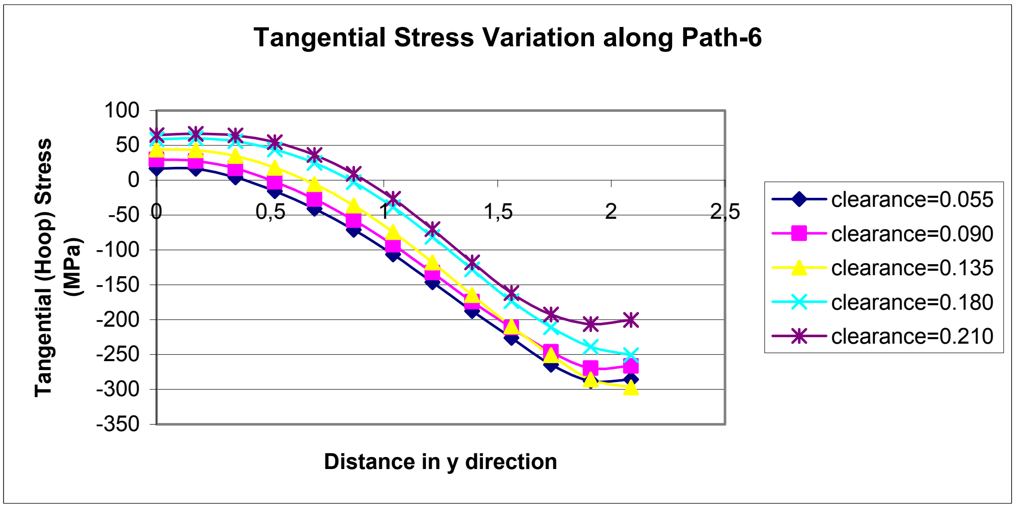

3.2 (m)

**Figure 3.2** (a) Selected paths in the riveted plates (b-m) Residual radial and tangential stress variations in the plates for different hole clearances

The deformation of the rivet hole is similar to the one which is obtained by cold working of the hole with an expanding mandrel. In critical rivet holes such a compressive zone is intentionally induced before the rivet installation in order to retard the nucleation of the fatigue crack. A residual compressive hoop stress zone in the inner plate is clearly seen in both Figure 3.1 and 3.2h. The presence of this area can be explained by looking at the yielding behavior of the material. According to the Tresca yield criterion, under the assumption that $\sigma_{yy}$ is the intermediate principal stress yielding occurs when,

$$|\sigma_{11} - \sigma_{33}| \geq S_y \tag{3.1}$$

As the rivet expands against the hole surface the contact pressure builds up. Eventually, the yield point of the material is exceeded. The material in the vicinity of the hole plastically deforms such that the circumference of the hole increases. Upon unloading (retraction of the bucking bar) the surrounding elastic material recovers and compresses the plastically deformed and enlarged material. The compressive stress zone near the hole edge is balanced with a tensile stress zone (Figure 3.2e) away from the hole edge. By this way, the compatibility of the material in radial direction is maintained.

The rivet shank is forced to fill the hole as the driven head of the rivet is formed. A sufficient amount of hole fill is required for a proper rivet installation. Hence, resulting interference between rivet shank and the rivet hole shows the quality of the connection. In addition to a through the thickness compressive stress variation, different magnitudes of the residual compressive stress fields were observed in the outer and the inner plate (Figure 3.3). A larger compressive residual stress field was developed in the inner plate especially around the driven head. As a result the inner plate will have a tighter connection than the outer plate.

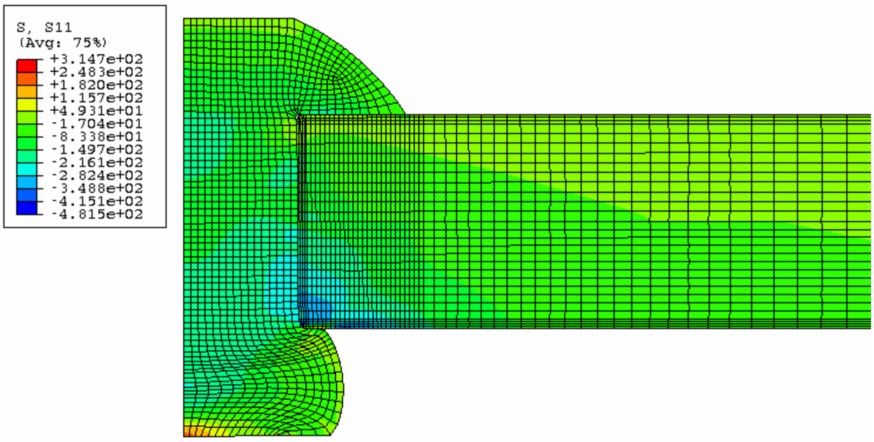

3.3 (a)

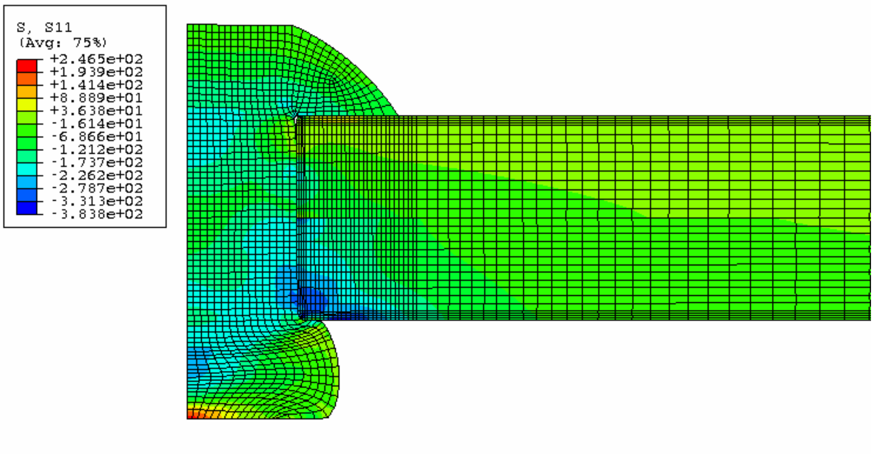
S, S11
(Avg: 75%)
+2.465e+02
+1.939e+02
+1.414e+02
+8.889e+01
+3.638e+01
-1.614e+01
-6.866e+01
-1.212e+02
-1.737e+02
-2.262e+02
-2.787e+02
-3.313e+02
-3.838e+02

3.3 (b)

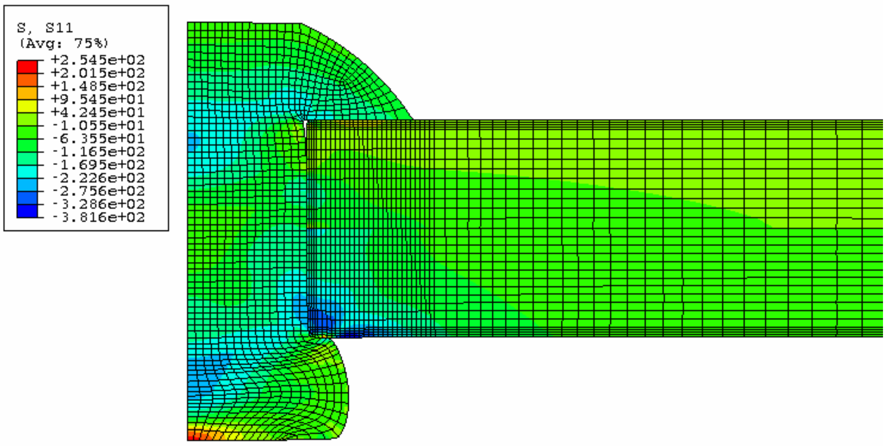
S, S11
(Avg: 75%)
+2.545e+02
+2.015e+02
+1.485e+02
+9.545e+01
+4.245e+01
-1.055e+01
-6.355e+01
-1.165e+02
-1.695e+02
-2.226e+02
-2.756e+02
-3.286e+02
-3.816e+02

3.3 (c)

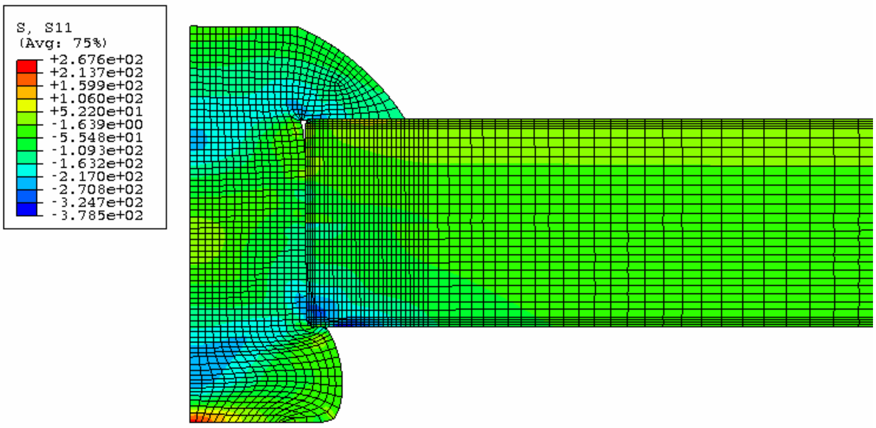
S, S11
(Avg: 75%)
+2.676e+02
+2.137e+02
+1.599e+02
+1.060e+02
+5.220e+01
-1.639e+00
-5.548e+01
-1.093e+02
-1.632e+02
-2.170e+02
-2.708e+02
-3.247e+02
-3.785e+02

3.3 (d)

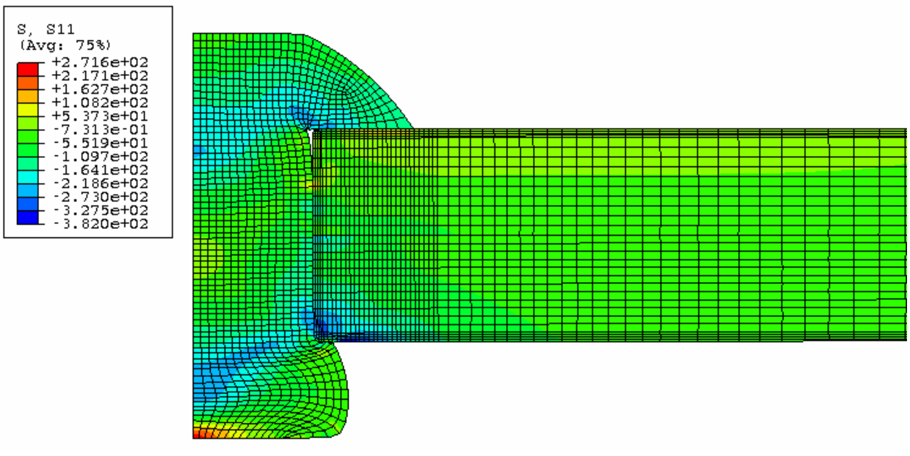

3.3 (e)

**Figure 3.3** Deformed rivet configurations and residual radial stress contours for the clearance values of (a)0.055 mm, (b) 0.090 mm, (c) 0.135 mm, (d) 0.180 mm and (e) 0.210 mm,

### 3.3.1 Effect of hole clearance on the final residual stress

In general, the stresses in the outer plate are lower than those in the inner plate. As a result the inner plate which is close to the driven head of the rivet becomes more critical in terms of fatigue. For a proper understanding of the effect of variations in the hole clearance on the fatigue life of the riveted connection the residual hoop and compressive stress contour plots and Figure 3.2 must be carefully examined. On these Figures the paths are drawn such that contact stress zones which is difficult to simulate accurately are omitted so, the initial stress values are slightly different than the real values. At first glance, it can be said that all the stresses in plates increase in magnitude as the hole clearance is decreased. In the outer plate radial stresses, which is an indication of the level of interference, become tensile for the larger values of the clearance, as seen in Figure 3.2b. Because, as a result of poor interference, shear stress acting on outer surfaces of this plate prevails. This means that unnecessarily large hole clearance values leads to poor riveted joint connection and load transfer mechanism changes. For a riveted connection the load is transferred either by means of the rivet body or via the frictional forces at the faying surface. In the case of large rivet holes the first load transfer mechanism prevails and more load is carried by the rivet. Hence, fatigue cracks are likely occur at the hole edge. Similar conclusions can be drawn for tangential stresses which are the critical stress of interest. The tangential stresses in the outer plate are all tensile and decrease as the clearance increases. Whereas, for the inner plate, the tangential stresses near the hole edge are compressive, as stated before, and they turns to the tensile stresses away from the hole edge. Figure 3.4 was generated in order to exhibit the sensitivity of the stress state to the clearance changes more clearly. In this Figure, radial (S11) and tangential (S33) stresses at some selected points in both plates and the rivet are drawn as a function of clearance changes. A linear curve was fitted to the data points from the analysis and the error of the curve fitting was expressed next to the each curve as $R^2$. The data gathered from the numerical model is naturally subjected to numerical error. One option to minimize this type of error in a numerical study is to decrease the size of the elements, especially, in regions where excessive deformation is expected. But, there is always a dilemma between numerical accuracy and the time spent for it. As a consequence of this, a curve was fitted to the data points in order to see the trends of the curves clearly. A careful investigation in figure 3.2 and 3.4 shows that as the clearance of the hole decreases the magnitude of the compressive stresses in the vicinity of the lower edge of the inner plate increases. On the other hand, the peak value of the tensile stresses increases and the tensile stress zone is shifted away from the hole edge. As a result, while the resulting compressive residual stress field increases, the fatigue performance by retarding the fatigue cracks emanating from the hole edge, the nucleation and subsequent propagation of the fatigue cracks are expected to take place at the faying surface away from the hole edge. This phenomenon makes the faying surface more critical in terms of fatigue.

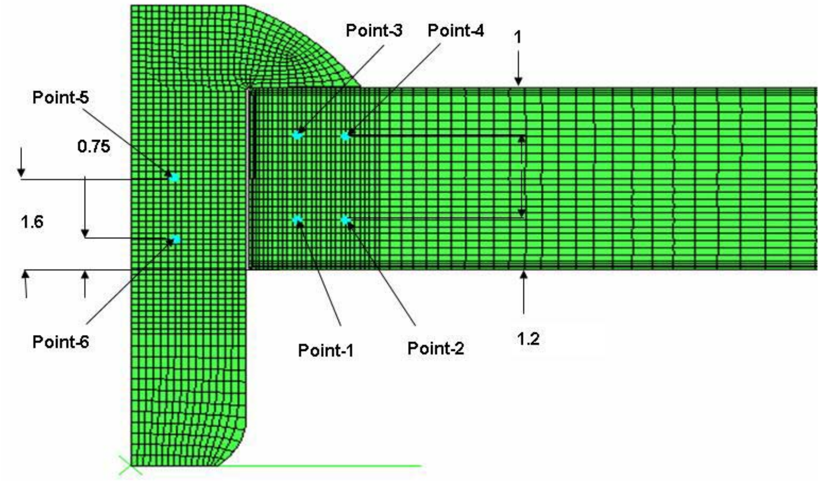
Point-3
Point-4
1
Point-5
0.75
1.6
Point-6
Point-1
Point-2
1.2

3.4 (a)

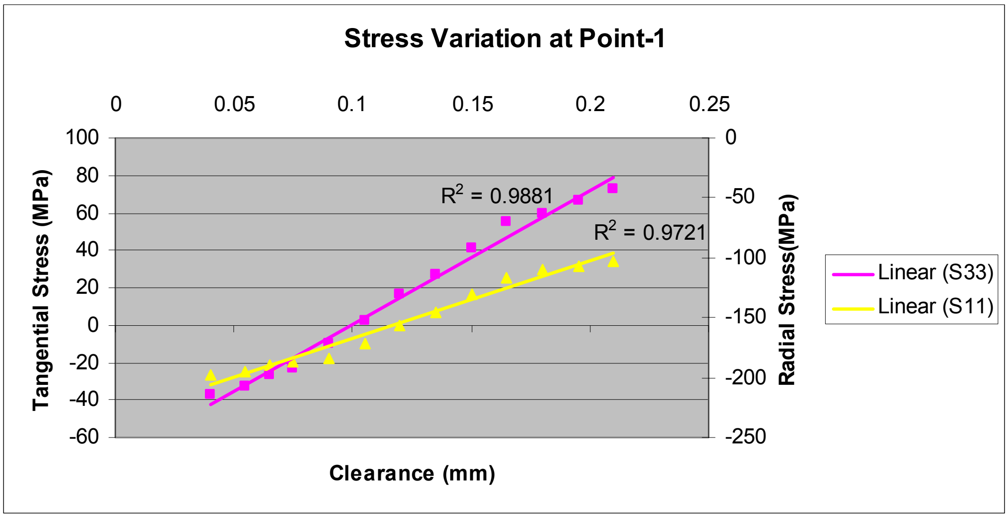
Stress Variation at Point-1
0
0.05
0.1
0.15
0.2
0.25
100
80
60
40
20
0
-20
-40
-60
0
-50
-100
-150
-200
-250
$R^2$ = 0.9881
$R^2$ = 0.9721
Tangential Stress (MPa)
Radial Stress(MPa)
Clearance (mm)
Linear (S33)
Linear (S11)

3.4 (b)

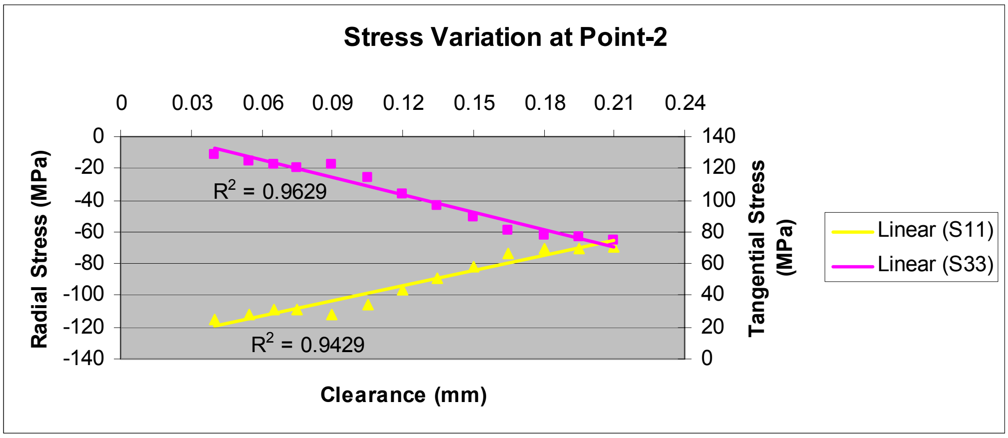
Stress Variation at Point-2
0
0.03
0.06
0.09
0.12
0.15
0.18
0.21
0.24
Radial Stress (MPa)
0
-20
-40
-60
-80
-100
-120
-140
Tangential Stress (MPa)
140
120
100
80
60
40
20
0
$R^2$ = 0.9629
$R^2$ = 0.9429
Clearance (mm)
Linear (S11)
Linear (S33)

3.4 (c)

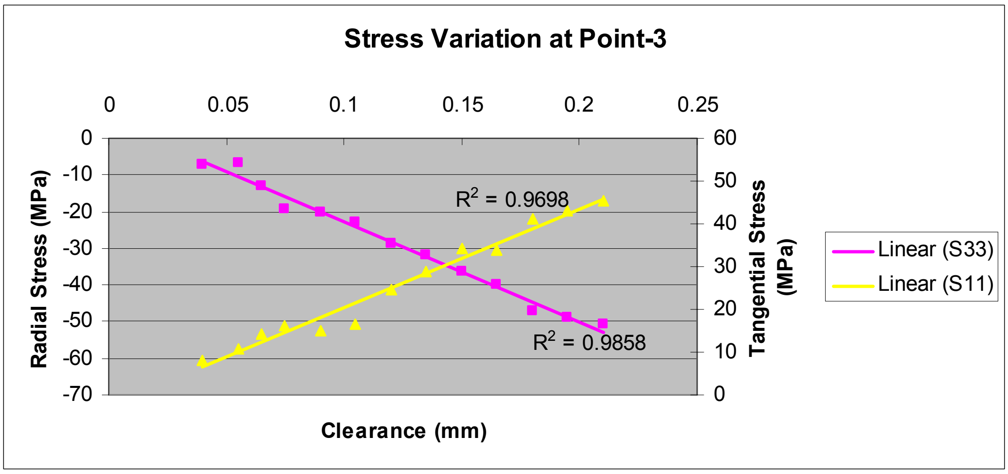
Stress Variation at Point-3
0
0.05
0.1
0.15
0.2
0.25
Radial Stress (MPa)
0
-10
-20
-30
-40
-50
-60
-70
Tangential Stress (MPa)
60
50
40
30
20
10
0
$R^2$ = 0.9698
$R^2$ = 0.9858
Clearance (mm)
Linear (S33)
Linear (S11)

3.4 (d)

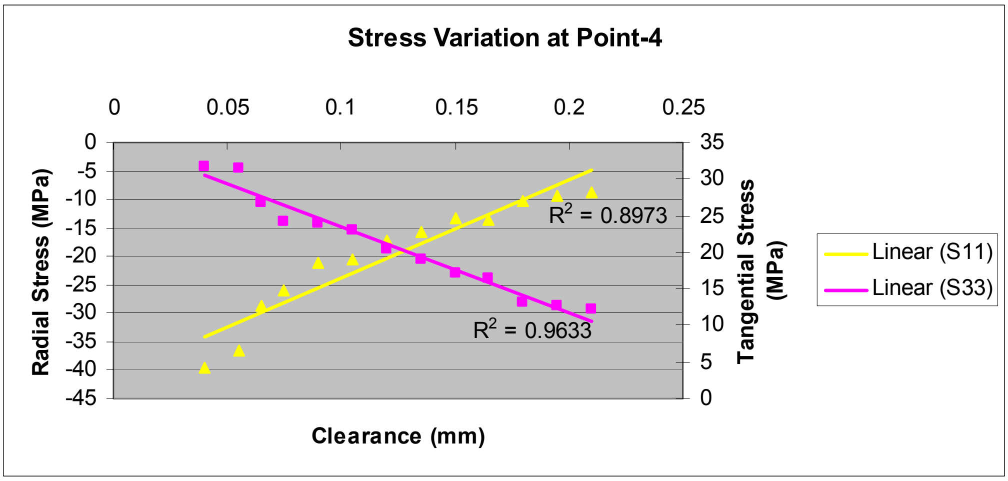
Stress Variation at Point-4
0
0.05
0.1
0.15
0.2
0.25
Radial Stress (MPa)
0
-5
-10
-15
-20
-25
-30
-35
-40
-45
Tangential Stress (MPa)
35
30
25
20
15
10
5
0
$R^2$ = 0.8973
$R^2$ = 0.9633
Clearance (mm)
Linear (S11)
Linear (S33)

3.4 (e)

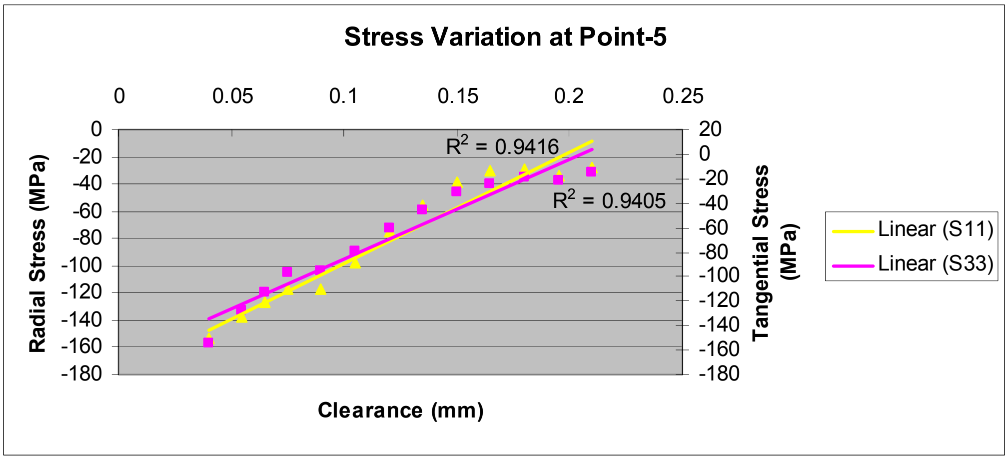

3.4 (f)

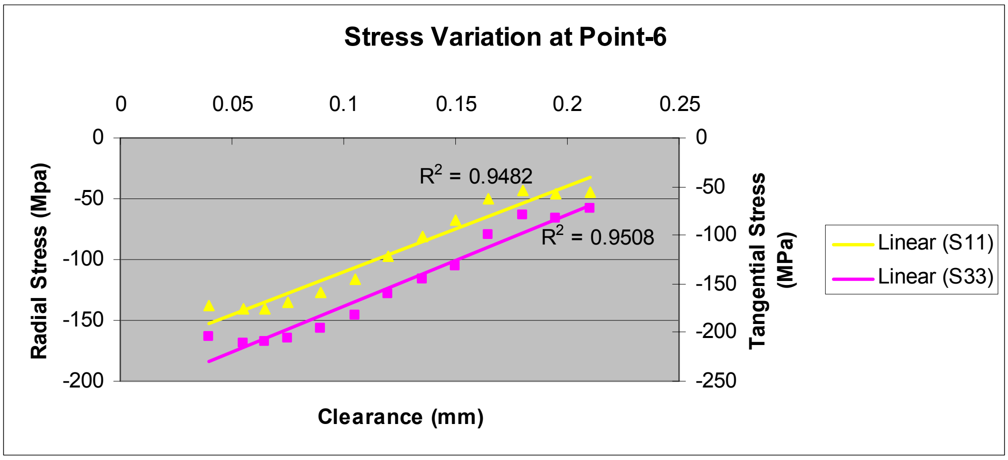

3.4 (g)

**Figure 3.4** Selected points and tangential and compressive stress changes as a function of the hole clearance on selected points

### 3.3.2 Effect of hole clearance on the deformation characteristics

As expected, changes in the clearance of the hole affects the deformation characteristics of the rivet. Figure 3.5 exhibits the changes of the maximum rivet driven head deformation (H) and the normalized driven head diameter ($D_{max}/D$) as a function of the hole clearance. In the case of a larger clearance value it is easier to force the rivet material into the rivet hole since the applied force is kept constant. Therefore, larger rivet shank expansions, smaller driven head diameters and smaller head height was observed. The rivets which have larger driven head diameter can provide more clamping resistance when the joint was loaded [1]. By this way, more load is transferred by the frictional force at the faying surface and as a result, the rivet bears fewer loads in loaded condition. This means that the probability of the fatigue crack formation near the hole edge decreases as the clearance of the hole is decreased. Again to filter out numerical inaccuracies, $D_{max}/D$ and H were fitted with a linear regression curve, whose equations are given below, respectively,

$$Dmax/D = -0.5521x+2.9333 \qquad R^2 = 0.9891 \qquad (3.2)$$

$$H = -1.4415x+2.377 \qquad R^2 = 0.981 \qquad (3.3)$$

Here, $R^2$ is again the error of the data points and x is the clearance value of the hole. Figure 3.5 represents the deformation characteristics of the selected type rivet under certain process parameters. Similar curves can be obtained for other type of rivets.

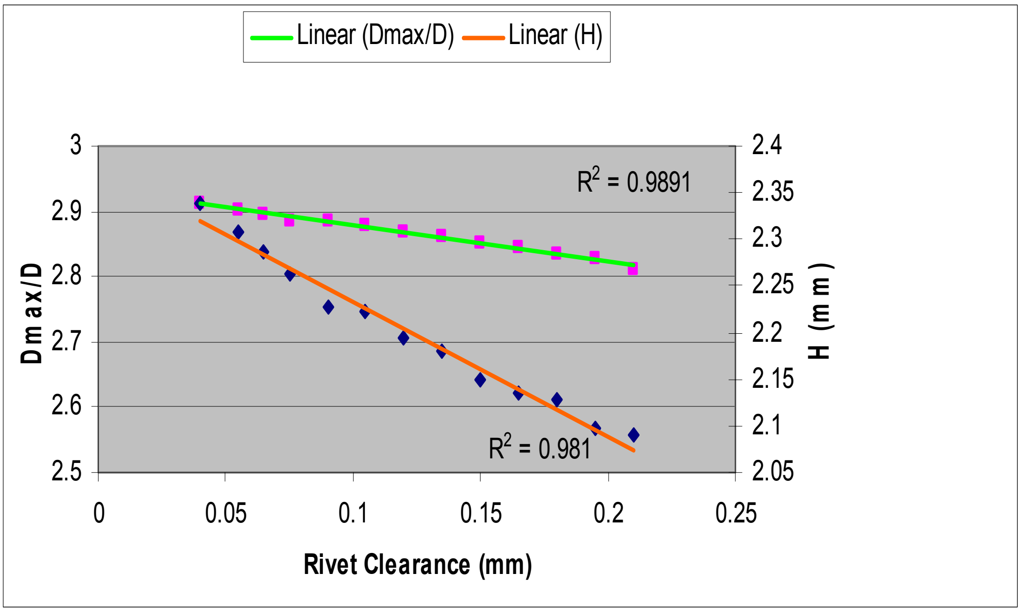

**Figure 3.5** Deformation of rivet head as a function of hole clearance

# CHAPTER 4

# DETERMINATION OF STRESS INTENSITY FACTOR USING THE FINITE ELEMENT METHOD

## 4.1 Introduction

As stated in the previous chapter, a potentially critical residual tensile stress zone exists in the inner plate. In airframes fatigue cracks are observed to initiate either on the hole edge or on the faying surface near to hole edge [14]. Hence, in the subsequent chapter a through crack will be positioned in the critical residual tensile stress zone and the effect of some riveting process parameters will be examined. Before studying on the final riveted lap joint model, which includes a crack in the inner plate, in this chapter a through crack will be placed in a rectangular plate and static tensile loading will be applied on the remote edge. By the help of this model the influence of mesh type on the precision of the finite element method result will be assessed. For this purpose firstly, a plate with a through crack will be modeled using different mesh densities and different meshing techniques. Secondly, mode-I stress intensity factor (SIF) will be evaluated . Displacement correlation technique (DCT) will be used for predicting the SIF. The results of the cracked plate will be compared with the results cited in the literature. After validation of the model, in the subsequent chapter, inner plate of the 3-D model which was generated in the third chapter will be replaced with a plate containing a through crack.

## 4.2 Numerical model of a through crack in a plate

The results of this chapter were compared with those given in the literature [21]. A rectangular plate with a thickness of 2mm subjected to tensile loading was modeled (Figure 4.1). The plate was made of Al 2024-T3 aluminum alloy, mechanical properties was input to the software according to Table 2.1. Although a quarter of the model is sufficient because of the symmetry condition, a half of the model was preferred in this study. For comparison purposes, 120 MPa tensile loading, which was used in reference 21, was applied by means of boundary conditions on the remote surface of the specimen. Moreover, displacement in y-direction on the symmetry plane was restricted.

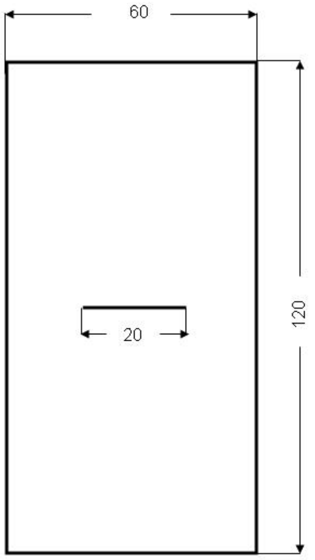

**Figure 4.1** Geometry of the center cracked plate

Since the crack tip causes very high, theoretically infinite, stresses and sharp stress gradients, partitioning of such a model is essential for applying an adequate mesh in the vicinity of the crack tip. The partitioned geometry and the boundary conditions of the specimen were depicted in Figure 4.2. In Figure 4.2 the crack is highlighted and crack opening direction is shown as an arrow perpendicular to the crack plane. The crack is introduced into the model with a seam by means of interaction module of ABAQUS/CAE. A seam is defined as a face, which is passing across the crack tips, that is originally closed but can open during an analysis. The finite element code generates overlapping nodes along a seam when the mesh is generated.

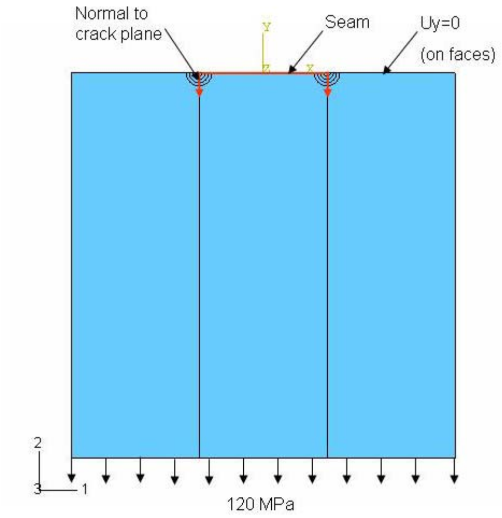

**Figure 4.2** The partitioned geometry and boundary conditions

A way to improve the results in the vicinity of the crack tip is to use singular finite elements suggested by Barsoum [35]. In order to generate this type of elements the whole body was meshed using 20-node second order quadratic brick elements called C3D20R. One side of these elements was collapsed such that all three nodes had the same geometric location. The mid-side nodes of the collapsed elements were also moved to a distance from the crack tip which was quarter of the edge length of the element, the method is so called quarter node point technique (Appendix-B.2). All these settings are done so as to obtain

$1/\sqrt{r}$ singularity in the strain field. The inclusion of the seam and the singularity definition using the interaction module of the software causes ABAQUS/CAE to crate automatically collapsed elements with correct connectivity definitions. The rest of the plate was meshed with sweep technique with medial axis algorithm.

## 4.3 Description of different meshing techniques

The aim of this section is to test different meshing techniques available in ABAQUS/CAE for SIF prediction in order to determine the most appropriate one for the subsequent study. For this reason two main mesh patterns, which were shown in Figure 4.3, were applied to the model with different mesh densities. The first type of mesh used the partitioning presented in Figure 4.2. By the help of circles centered on the crack tip the elements were focused on the crack tip zone. The inner circle contained second order wedge elements of which one edge was collinear with the crack front and the rest of the plate was meshed with hexahedral elements. The second type of mesh was again focused on the crack tip region but this time the whole plate was meshed with second order hexahedral elements. For this model focusing of the mesh was achieved by the help of appropriate seeding strategy applied on the edges of the plate. Seeding is a tool provided by ABAQUS for indicating necessary element sizes along the edges of the geometry. On the crack front, edge length of the element was adjusted such that its length was equal to 1/20, 1/40 and 1/80 of the total crack length for the very coarse mesh, coarse mesh and refined mesh, respectively.

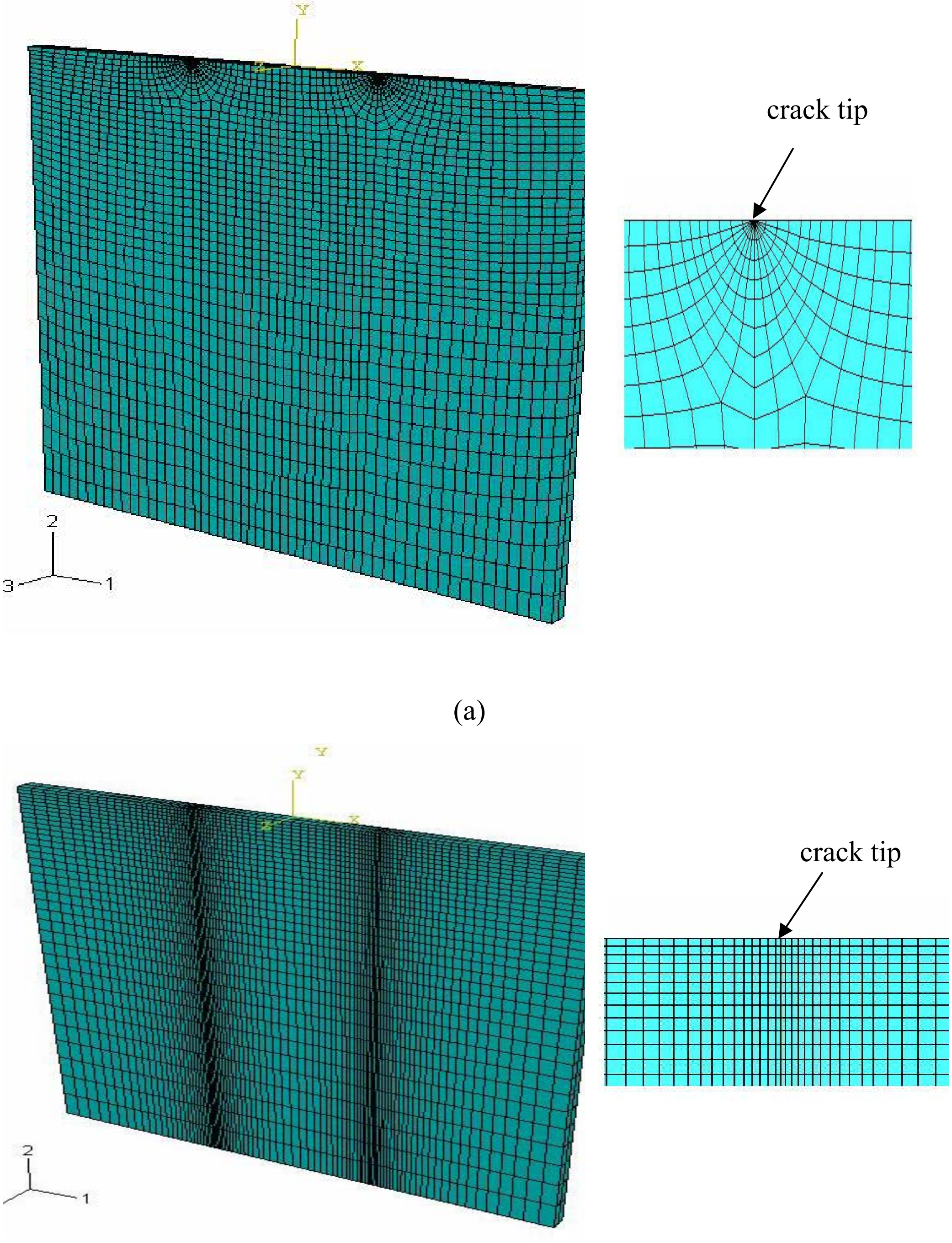

(a)

(b)

**Figure 4.3** (a) First type mesh and detail view of crack tip zone (b) Second type mesh and detail view of crack tip zone

**Table 4.1** Number of elements used throughout the analysis

| | | First type of mesh | Second type of mesh |
|---|---|---|---|
| Number of elements | Very coarse | 7160 | 6800 |
| | Coarse | 10840 | 11300 |
| | Refined | 18880 | 18000 |

## 4.4 Stress intensity factor calculation

The stress intensity factor was calculated via the DCT method. In this method displacement values of the two nodes which were adjacent to the crack tip were used (Appendix-B.2). Since the plate was loaded in the opening mode only mode-I stress intensity factor ($K_I$) was calculated. $K_I$ for a symmetrical crack can be calculated using Equation B.8. $K_I$ values for a node positioned in the middle of the sheet thickness were presented in Table 4.2 for comparison with the literature. Mode-I stress intensity factor was calculated using relevant solutions in the literature. General form of the $K_I$ is,

$$K_I = \sigma \cdot \sqrt{\pi \cdot a} \cdot F(a/b) \qquad (4.1)[22]$$

Where ‘a’ is the half of the crack length and ‘b is the half of the plate width. In Equation 4.1, a few solutions are available for F in the relevant reference. Among them Tada’s solution was found more precise [21] hence, the below expression was used for F,

$$F(a/b) = 1 - 0.025(a/b)^2 + 0.06(a/b)^4)\sqrt{\sec\frac{\pi \cdot a}{2b}} \qquad (4.2)[22]$$

**Table 4.2** $K_I$ values as a function of mesh density for an intermediate node

| | | $K_I$ (MPa.mm$^{1/2}$) | Tada,Ref [22] | % Error |
|---|---|---|---|---|
| **First type mesh** | very coarse | 645.39 | 721.29 | 10.52 |
| | coarse | 707.92 | | 1.85 |
| | refined | 726.48 | | -0.72 |
| **Second type mesh** | very coarse | 735.09 | | -1.91 |
| | coarse | 753.27 | | -4.43 |
| | refined | 757.57 | | -5.03 |

Moreover, the same geometry was modeled as a 2-D planar body and solved for plane stress and plane strain cases. Partitioning of the 2-D bodies were exactly the same as the first type mesh of 3-D analysis since better results were obtained for that case. Hence, a similar mesh structure was obtained between 2.D and 3-D analysis which was essential for proper comparison. The results, tabulated in Table 4.3, showed that the problem could be better approximated by using plane strain assumption. Also it was noted that considerable amount of time was saved in 2-D solutions.

**Table 4.3** $K_I$ values of the same problem for 2-D planar and 3-D cases

| | $K_I$ (MPa.mm$^{1/2}$) |
|---|---|
| **Tada,Ref [22]** | 721.29 |
| **3-D rectangular plate (2 mm thickness)** | 726,48 |
| **2-D planar (plane strain)** | 717.25 |
| **2-D planar (plane stress)** | 803.45 |

## 4.5 Comparison of different meshing techniques for SIF calculation

From this linear analysis it was expected to obtain a $K_I$ value which converge to a certain value as the number of the elements around the crack tip was increased. Figure 4.5 depicts the variation of the SIF's as a function of mesh density.

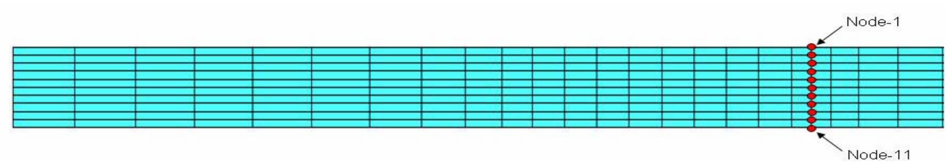

4.4 (a)

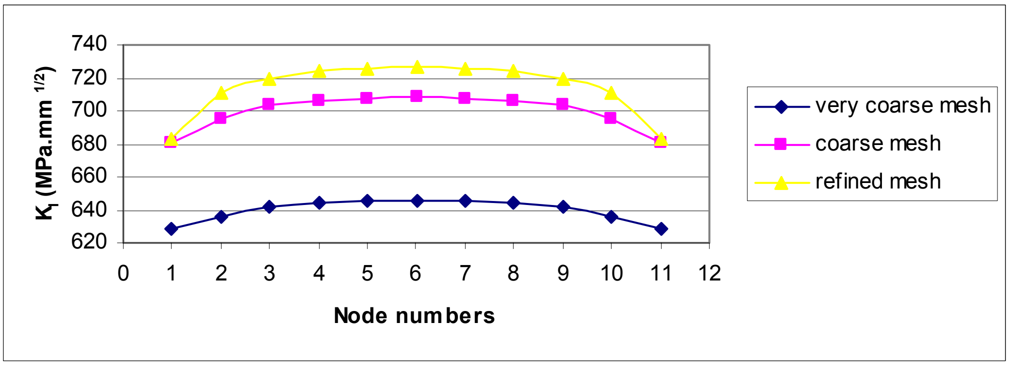

4.4 (b)

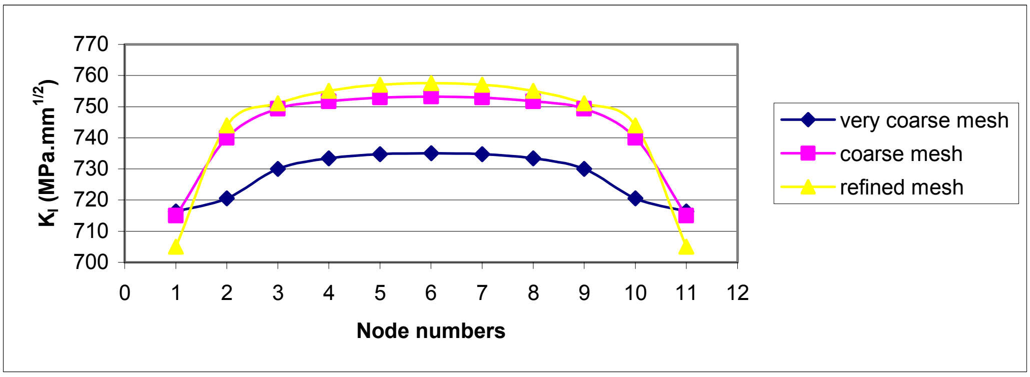

4.4 (c)

**Figure 4.4** (a) Position of nodes along the crack front (b) stress intensity factor plot for the first type mesh (c) stress intensity factor plot for the second type mesh

For better visualization of the convergence of the SIF's, $K_I$ values corresponding to each node were compared on a separate Figure.

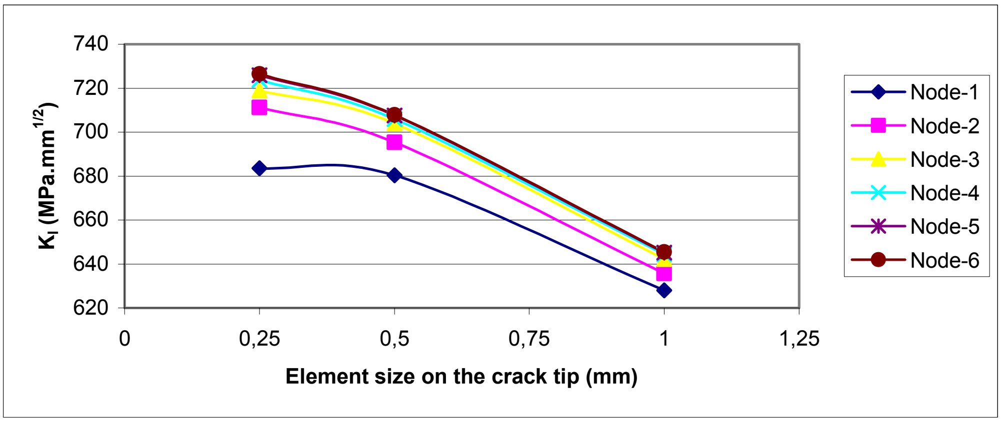

4.5 (a)

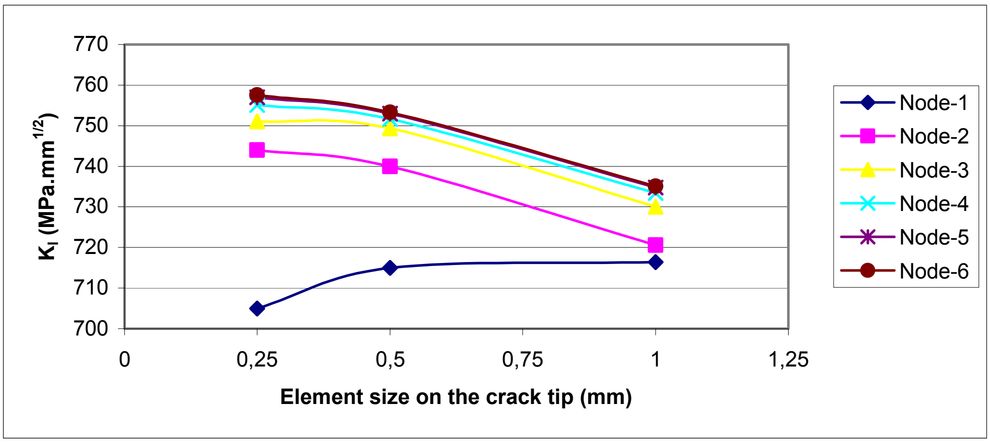

4.5 (b)

**Figure 4.5** (a) Comparison of the SIF's along crack front for the first type mesh (b) Comparison of the SIF's along crack front for the second type mesh

It was seen that the greater the mesh refinement the better the gradient of the stress state near the crack tip was modeled. In the case of first type meshing technique, it was easier to focus finite elements in the vicinity of the crack tip therefore, first type of meshing technique was found more powerful in terms of obtaining the crack tip singularity. Figure 4.5 and Figure 4.6 shows that both meshing techniques seemed to generate convergent results. In addition, the second meshing technique converged faster than the former one however, the second meshing technique's accuracy was poor, as seen from the Table 4.2. As the numbers of the elements were increased around the crack tip for the former meshing technique, the error became %-0.72 which was quite good. Moreover, it was observed that inaccurate results were predicted for the nodes close to the surface of the plate so, the number of the elements through the thickness of the plate seemed to be also crucial. In consequence, it was seen that DCT method requires elements whose edge lengths are as small as possible around the crack tip region. Furthermore, the first meshing technique generated more accurate results than the he second one. Also the first technique was superior in terms of modeling the crack tip singularity. Hence, the first meshing technique was preserved for the subsequent study

# CHAPTER

# FINITE ELEMENT ANALYSIS OF A CRACKED RIVETED LAP JOINT

## 5.1 Introduction

Hitherto, a 3-D finite element model of a single-lap joint and a plate with a through crack were generated. Accuracy of these models were examined by comparing their results with those presented in the literature. For both of the models satisfactory results were obtained. In this chapter focus will be on a model that combines these two models in single model in order to analyze effects of clearance and crack length changes on the SIF's of a through crack initiated on the inner plate of the joint.

In third chapter, a parametric study was carried out so as to uncover a relation between clearance changes and residual stress field. In the 2-D model of that chapter, a residual tensile stress field in tangential direction was observed next to the compressive stress filed in the vicinity of hole edge, as shown in Figure 3.2e. Since it is the tensile stress that forces a through crack to open, presence of this field becomes a threat for the fatigue life of the joint if a fatigue crack initiates in this region. In addition to that, as described in the literature [1,3], two main locations exist for the nucleation of a fatigue crack for a lap joint. First one is the hole edge where high contact stresses are responsible for damage and second one is on the faying surface due to effect of fretting or any other damage that occur during manufacture or assembly. In the worst case scenario, these two damage mechanisms (tensile residual stress field and crack) can occur at the same location and threaten fatigue performance of a joint which is under effect of external loading.

This chapter focused on a single lap joint of which the inner plate is substituted with a potentially cracked plate. The crack was positioned at the faying surface and passes through entire thickness of the sheet. In order to capture the effect of residual stress field, the crack was kept closed during rivet installation, then it was allowed to open in the residual stress field. Both tip of the crack lay in the tangential tensile stress zone, one of them being in the maximum tangential tensile stress zone, so that effect of this zone on the fracture parameters of the joint can be quantified. Two parameters were selected for the subsequent parametric studies namely; hole clearance, as studied in the third chapter, and crack length. Stress intensity factors were calculated as a function of these two parameters

## 5.2 Definition of the model

Analysis of a cracked riveted joint was composed of two main steps: Forming of the riveted joint and subsequent loading. Throughout the analysis half of the model was used due to symmetry condition. Rivet and the plates to be joined were modeled as deformable bodies and the bucking bar was modeled as rigid body. Geometry of the model was presented in Figure 5.1. The crack which was the focus of this chapter was positioned in the inner plate near to hole edge, perpendicular to the loading direction. In a study aiming to describe the areas prone to fatigue failure [23], majority of the fatigue failures were observed on the holes and on the surface of the plate (Table 5.1). The same study revealed that most of the failures occurring on the surface of the airframe had no obvious reason (Table 5.2). However, there was lack of information in the literature on the locations of the cracks resulting in fatigue failures.

Table 5.1 Main fatigue failure locations in aluminum alloy components of a helicopter [23]

| Initiation Site | Percentage | |
|---|---|---|
| | All | Fuselage Only |
| Hole | 34.4 | 52.9 |
| Surface | 30.9 | 28.1 |
| Radii | 19.5 | 11.6 |
| Corner/Edge | 7 | 6.6 |
| Weld Interface | 8.2 | - |

Table 5.2 Main causes of fatigue initiation in aluminum alloy components of a helicopter [23]

| Primary Cause of Initiation | Number of Failures | | | | |
|---|---|---|---|---|---|
| | Hole | Radii | Surface | Corner/Edge | Weld |
| Fretting Wear | 29 | - | 19 | - | - |
| No Obvious Cause/ Not Specified | 29 | 19 | 28 | 7 | 4 |
| Manufacture/Assembly | 18 | 16 | 13 | 5 | 15 |
| Corrosion | 7 | 3 | 7 | 1 | - |
| Design Issues | 5 | 7 | 2 | 1 | 2 |
| Service | - | 2 | 7 | 2 | - |
| Material Defects | - | 3 | 3 | 2 | - |

Therefore, the place of the crack was selected such that the effect of residual stress field and the external loading were experienced severely (Figure 5.2). In Figure 5.2, the critical analysis parameters of which the effect on the SIF’s will be evaluated are denoted as ‘c’ (clearance) and ‘a’ (crack length).

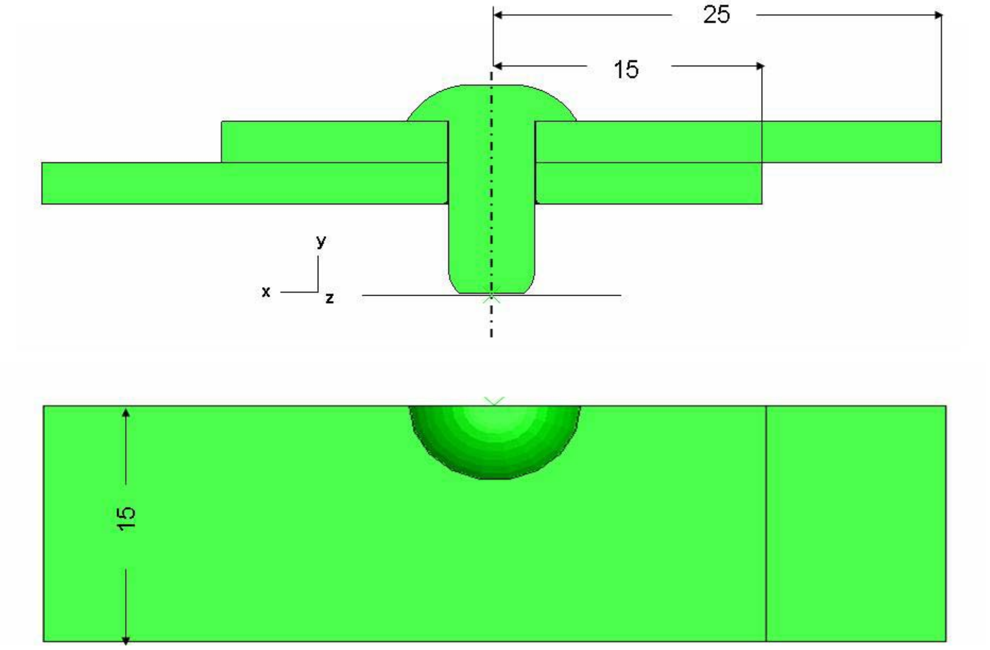

**Figure 5.1** Geometry of the model

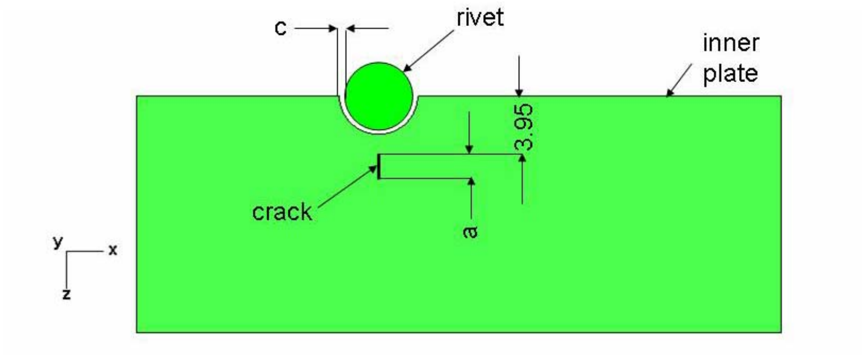

**Figure 5.2** Definition of the analysis parameters

## 5.3 Description of the finite element model

As studied in Chapter 4, DCT requires a very refined mesh for an accurate solution. Hence, in this section an extra effort was spend for obtaining a reasonable mesh especially around the crack tip region. Except the inner plate, which contained the crack, the model was meshed with C3D8R first order hexahedral elements whereas the inner plate was meshed with C3D20R second order hexahedral elements. The reason for the choice of different element types lay under the fact that the second order elements affects the solution time considerably. As a result, they were used wherever necessary. A view of the mesh is shown in Figure 5.3. 15069 elements and 21498 nodes were included in the whole model. 9762 numbers of the elements were used for the inner plate.

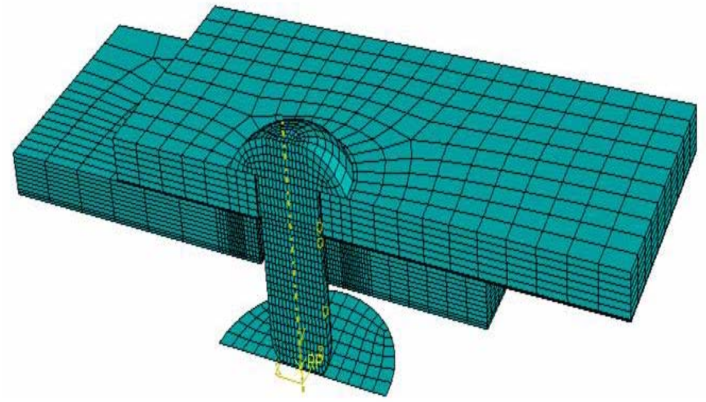

5.3 (a)

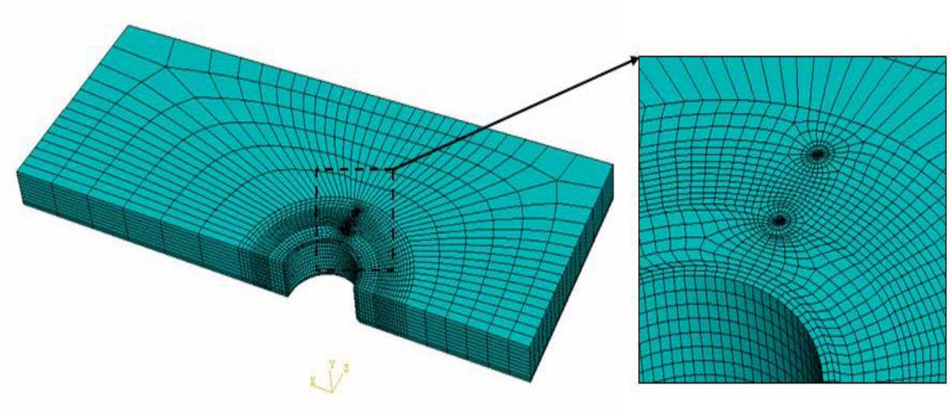

5.3 (b)

**Figure 5.3** Mesh of the (a) whole model and (b) the inner plate

The rivet was assumed to be a member of a rivet row so, the boundary conditions were applied to the rivet accordingly. Symmetry boundary conditions were applied to the remote surfaces of the plates. Squeezing force of 17000 N was applied by means of the rigid bucking bar as before and the manufactured head of the rivet was constrained via displacement boundary conditions. In addition, service load was applied on the free surfaces as tensile loading of 120 MPa. As a result, except the service loading, the model was similar to the one which was used in the third chapter in terms of boundary conditions. The boundary conditions of the current model was illustrated in Figure 5.4. Furthermore, a through crack was modeled in the inner plate perpendicular to the loading direction. In modeling the crack interaction module of the ABAQUS/CAE was used. As described in Chapter 4, a seam was placed on the crack plane. Then, crack parameters such as crack front and crack opening direction were specified in the interaction module. ABAQUS automatically generates duplicate nodes on the crack plane.

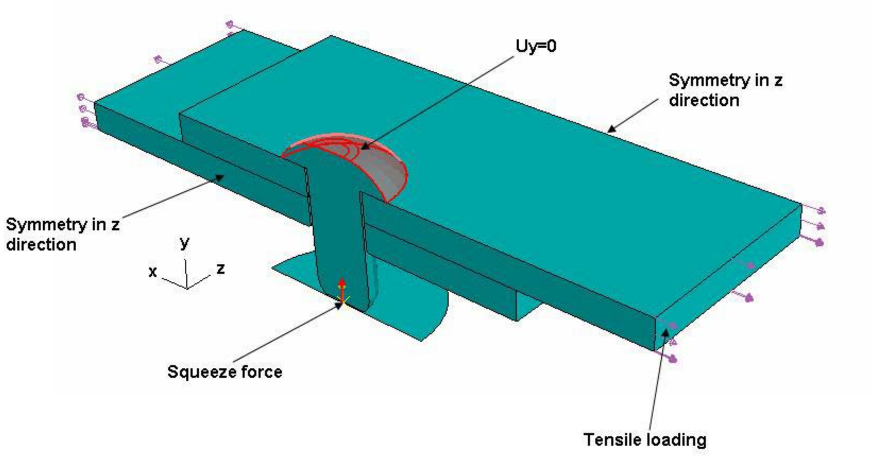

**Figure 5.4** Boundary conditions of the model

Interaction of the bodies with each other was described as contact condition with coefficient of friction "μ" was equal to 0.2 for all surfaces. Interaction of the inner and outer plate was specified as small sliding contact whereas the rest of the interactions were modeled as finite sliding.

A special technique was used in solving the problem in two separate steps. Firstly, whole model was solved as if there were no cracks in the inner plate and service loading on the edges. In order to keep the crack closed, throughout the first step every node on one face of the crack plane was tied to the counterpart node on the opposite face by means of multi-point constraints (MPC). Restart data was queried from ABAQUS/Standard at the end of each increments of the solution. Secondly, at the beginning of the second step the results of the first step were imported. Hence, the first increment of the second step became the final increment of the first step. By this way the residual stress field was transported to the second step. Then, the MPC's were removed and the crack was released at the same time the service loading was applied. This solution procedure was repeated for every changing parameter.

## 5.4 Convergence study

Altough, in previous chapters, the model of this chapter was proved itself to simulate the residual stress field satisfactorily, its capability of modeling a crack still required some justification. Thus, a convergence check was carried out so as to see the impact of number of elements on the results (Figure 5.5). For this type of analysis edge length of the collapsed elements adjacent to the crack front is critical. Therefore, the same model was solved for three different values of the edge length of the collapsed element, which were 0.03 mm , 0.06 mm and 0.12 mm and the $K_I$ values were predicted.

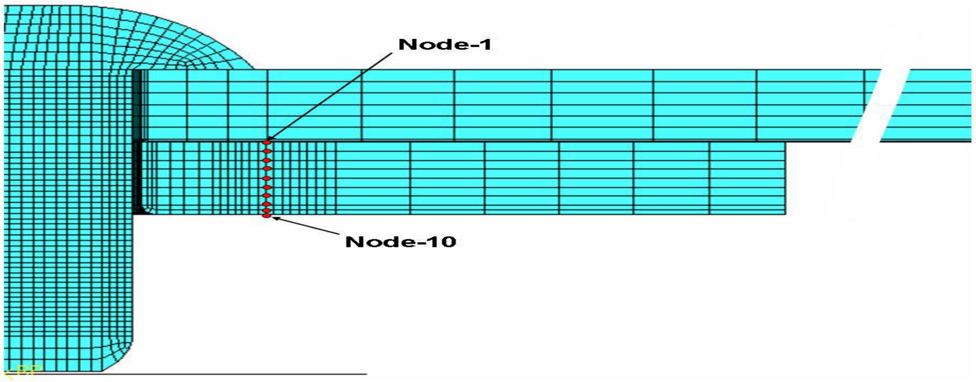

5.5 (a)

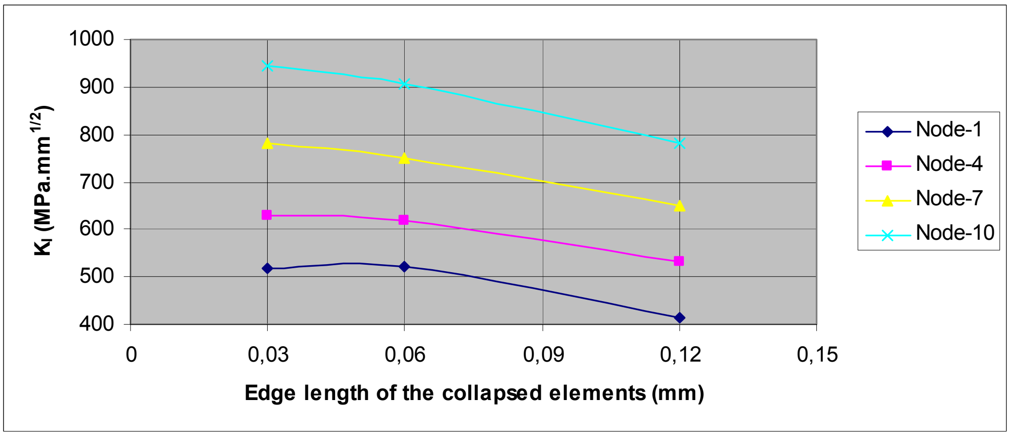

5.5 (b)

**Figure 5.5** FE model for SIF calculation (a) Position of nodes along the crack front and (b) SIF variation across the thickness

The model appeared to converge to a certain value especially, for the mid-nodes. So, the model will be used in subsequent chapters more reliably.

## 5.5 Parametric studies

Previous chapters proved the viability of the finite element method in simulating the riveting process. While simulating the riveting process, previous chapters were dedicated to the understanding of the complex residual stress field. In this chapter, effect of residual stress and some other boundary conditions will be studied. The crack length and the hole clearance were selected as the primary parameters to be examined. For this reason, a through crack was placed in tensile residual stress zone. Starting point of cracks, as shown in Figure 5.2, was selected such that they lay in the maximum tensile stress region which was observed in Figure 3.2i. In addition, the analysis was repeated for a number of clearance values corresponding to each crack length value.

### 5.5.1 Effect of hole clearance on the stress intensity factors

The first parameter to be studied was the clearance change. As stated before, the SIF's were calculated under the effect of external loading. Before moving to the actual study, the cracks were released to open without applying any external loading. By this way effect of just the residual stresses variations arising from the clearance changes on the SIF's were observed. Figure 5.6 illustrated five times enlarged views of the open cracks for the same model with different loading condition.

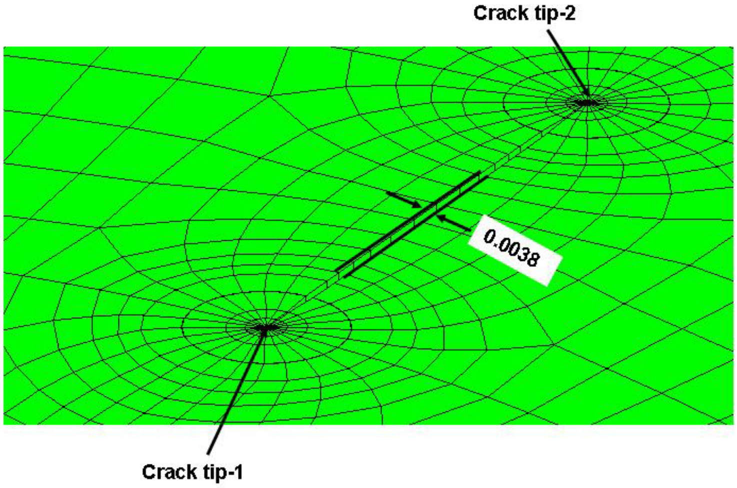

5.6 (a)

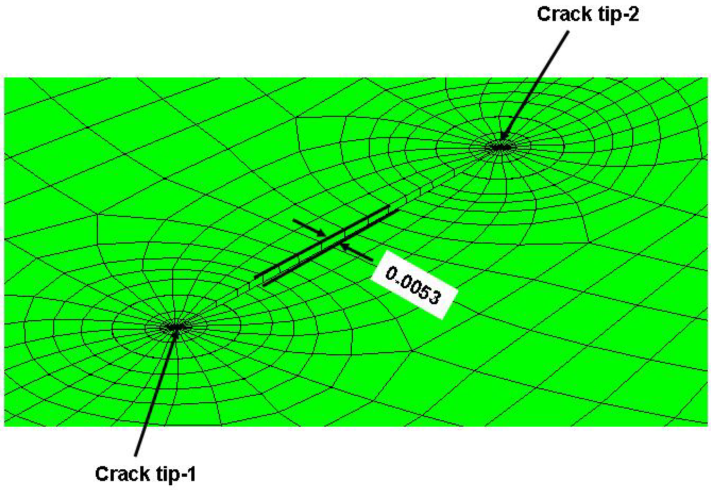

5.6 (b)

**Figure 5.6** Scaled view of (a) crack opened in the residual stress filed and (b) crack opened by external loading in addition to residual stress field

Since our primary goal is predicting the SIF's under external loading, this study was carried out for comparison purpose. Hence, the effect of residual stress was studied only for a crack length of 1.25 mm. The results were depicted in Figure 5.7.

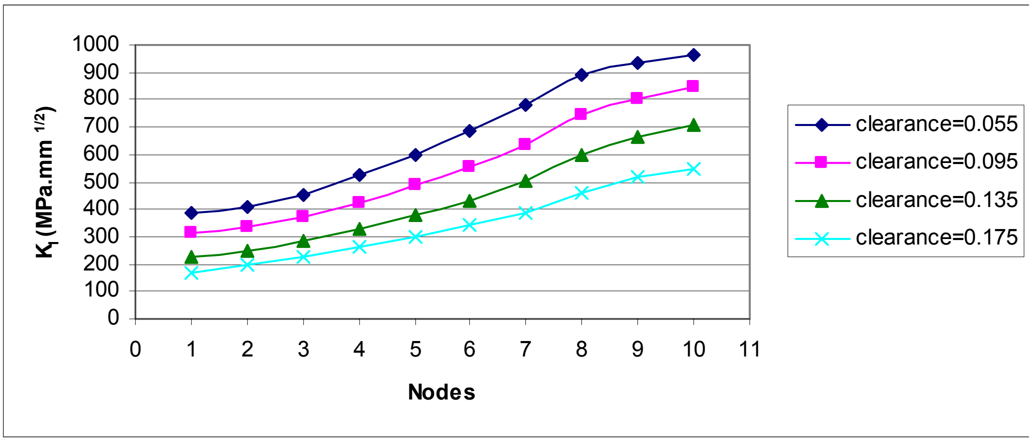

5.7 (a)

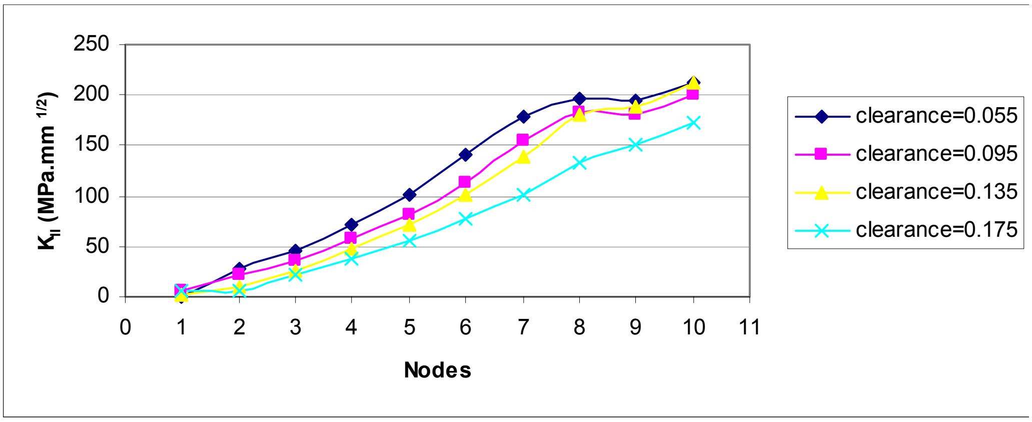

5.7 (b)

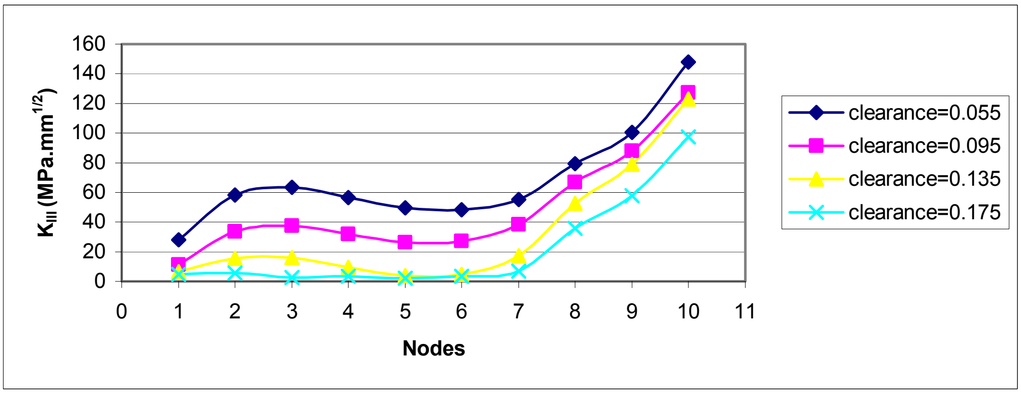

5.7 (c)

**Figure 5.7** Effect of clearance change on SIF (a) $K_I$ (b) $K_{II}$ and (c) $K_{III}$ without external loading

In a similar manner, external loading was applied and the SIF's were calculated by varying the clearance values for crack lengths 1.25, 1.5, 1.75 and 2. Each result was illustrated as a separate Figure. Although, this was a mixed mode crack problem, here only the $K_I$ values were presented. Because, there were large oscillations and considerable variations in $K_{II}$ and $K_{III}$ curves. The reason for this is that, even for simple model of Chapter 4, which was a rectangular plate loaded in tension, the software generates $K_{II}$ and $K_{III}$ values due to numerical inaccuracy. This numerical disturbance made the $K_{II}$ and $K_{III}$ values inaccurate since their values were much smaller than those of $K_I$. Figure 5.8 shows sample results for $K_{II}$ and $K_{III}$.

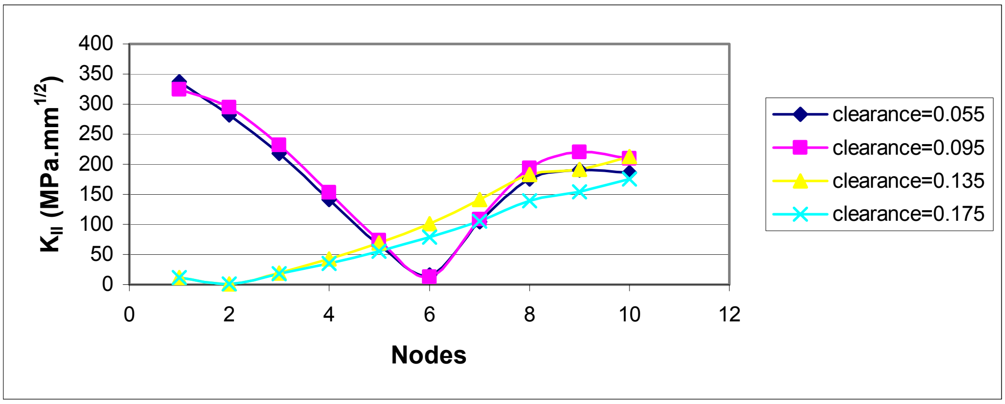

5.8 (a)

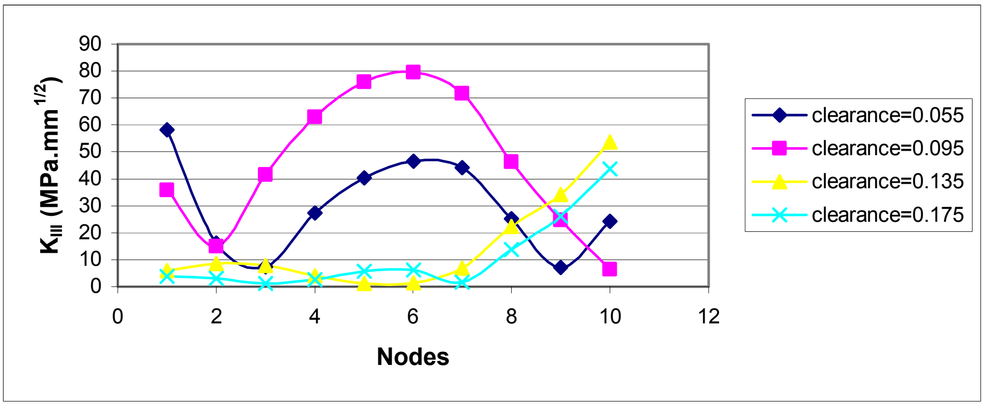

5.8 (b)

**Figure 5.8** Stress intensity factors of the model with 1.25 mm crack, (a) $K_{II}$ and (b) $K_{III}$

$K_I$ values were calculated for both of the crack tips. In Figure 5.9 $K_I$ values for the crack tip which is close to the hole edge were presented whereas the Figure 5.10 depicted $K_I$'s for the opposite side.

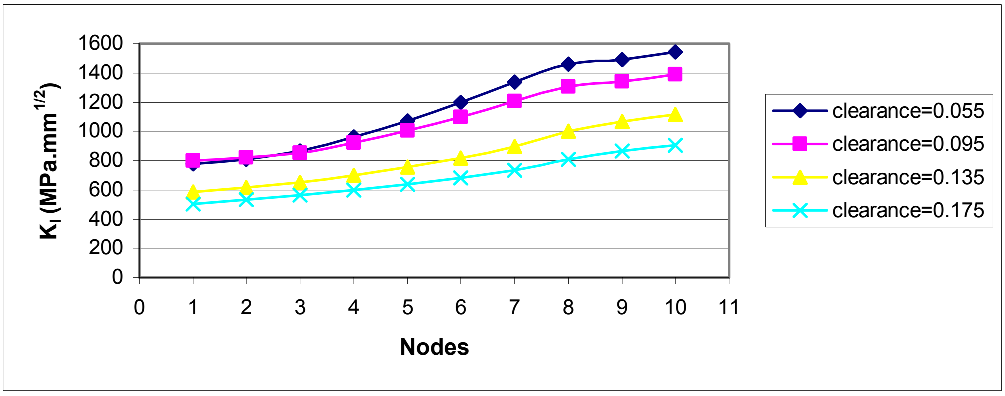
K$_I$ (MPa.mm$^{1/2}$)
Nodes
clearance=0.055
clearance=0.095
clearance=0.135
clearance=0.175
1600
1400
1200
1000
800
600
400
200
0
0 1 2 3 4 5 6 7 8 9 10 11

5.9 (a)

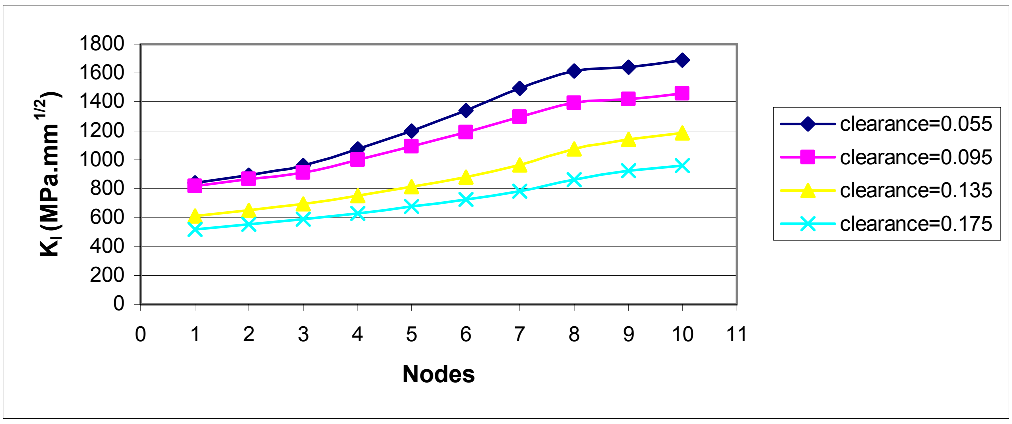
K$_I$ (MPa.mm$^{1/2}$)
Nodes
clearance=0.055
clearance=0.095
clearance=0.135
clearance=0.175
1800
1600
1400
1200
1000
800
600
400
200
0
0 1 2 3 4 5 6 7 8 9 10 11

5.9 (b)

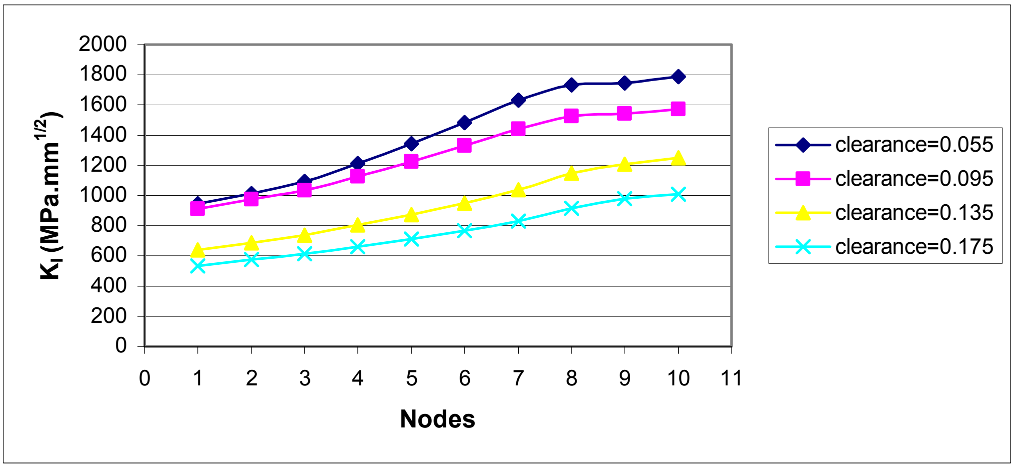
K$_I$ (MPa.mm$^{1/2}$)
Nodes
clearance=0.055
clearance=0.095
clearance=0.135
clearance=0.175
2000
1800
1600
1400
1200
1000
800
600
400
200
0
0 1 2 3 4 5 6 7 8 9 10 11

5.9 (c)

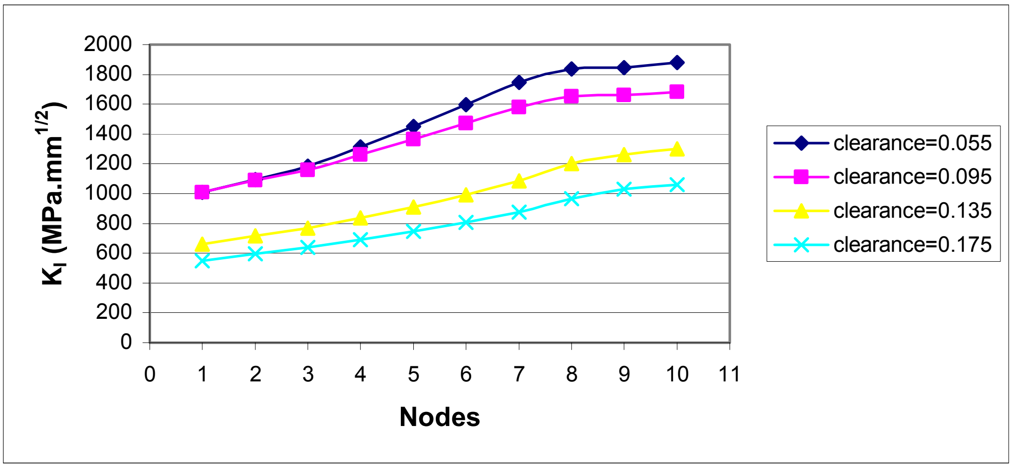

5.9 (d)

**Figure 5.9** Variation of mode-I stress intensity factor as a function of clearance for crack lengths of (a) 1.25 mm, (b) 1.5 mm, (c) 1.75 mm and (d) 2 mmofor crack tip-1

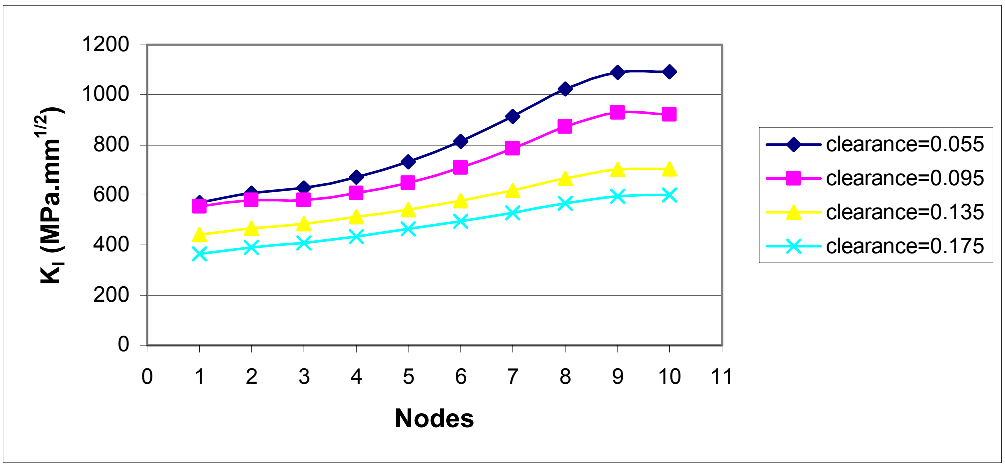

5.10 (a)

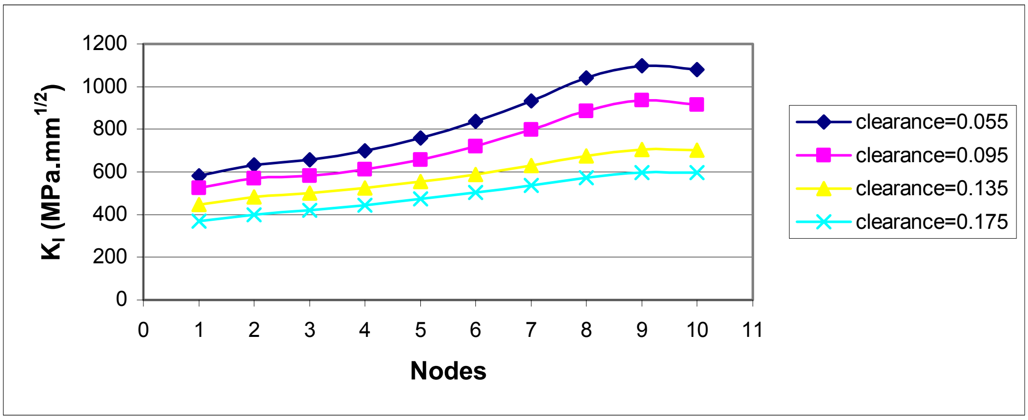

5.10 (b)

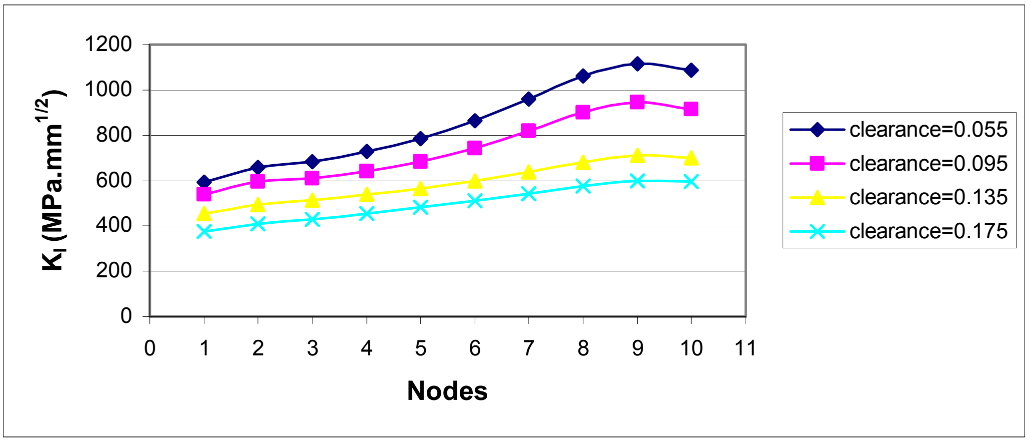

5.10 (c)

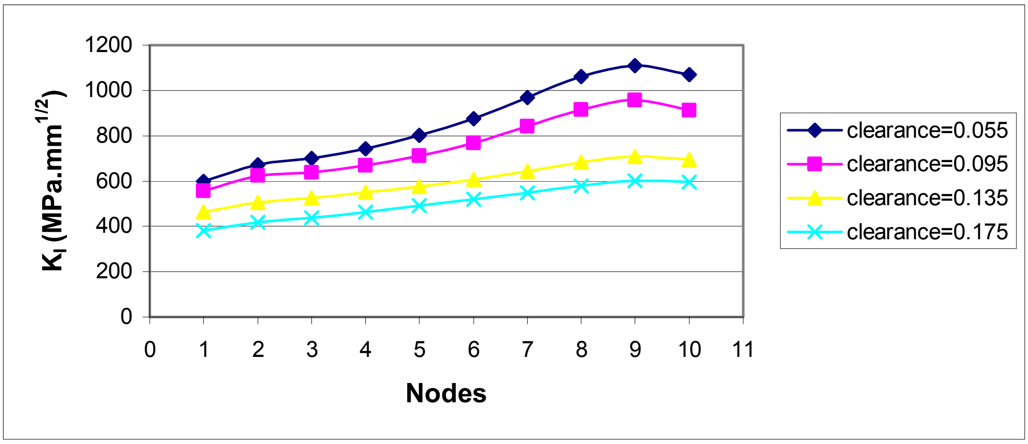

5.10 (d)

**Figure 5.10** Variation of mode-I stress intensity factor as a function of clearance for crack lengths of (a) 1.25 mm, (b) 1.5 mm, (c) 1.75 mm and (d) 2 mm for crack tip-2

Effect of clearance changes on SIF's were clearly seen in Figure 5.7 to 5.10. In parallel with the increasing magnitude of the tensile residual stress field, magnitudes of the stress intensity factors were increased. Magnitudes of the $K_I$'s showed dependence in the through the thickness direction. The $K_I$ values were much larger on the bottom side of the inner plate as larger stresses arising from larger deformations took place at this location. This fact is a natural consequence of the through the thickness variation of the stress state. Application of the tensile loading resulted in a shift of curves in the downward direction as the clearance was increased.

### 5.5.2 Effect of crack length on the stress intensity factors

The crack length was the second parameter to be studied. In studying the crack length, starting point of the crack was kept in the same location and the analysis was repeated for a number of crack length values. Figure 5.11 and 5.12 illustrated the variation of the mode-I stress intensity factor as a function of crack length.

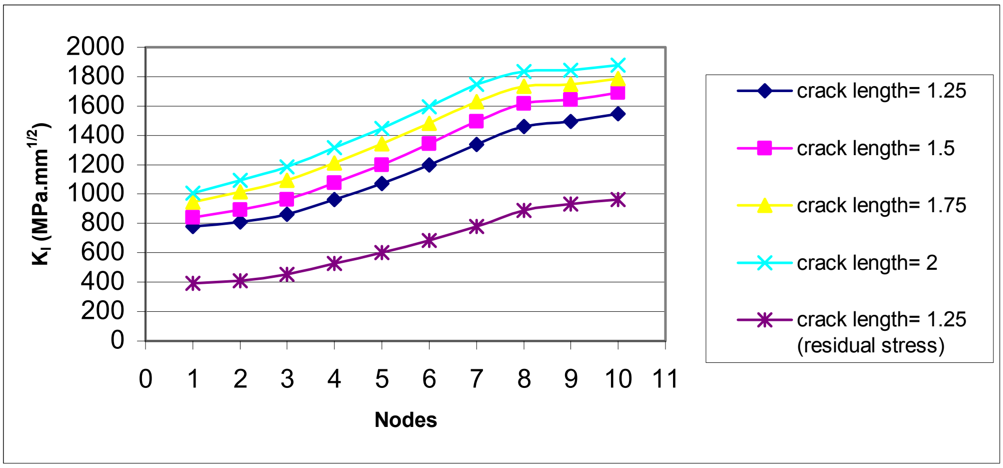

5.11 (a)

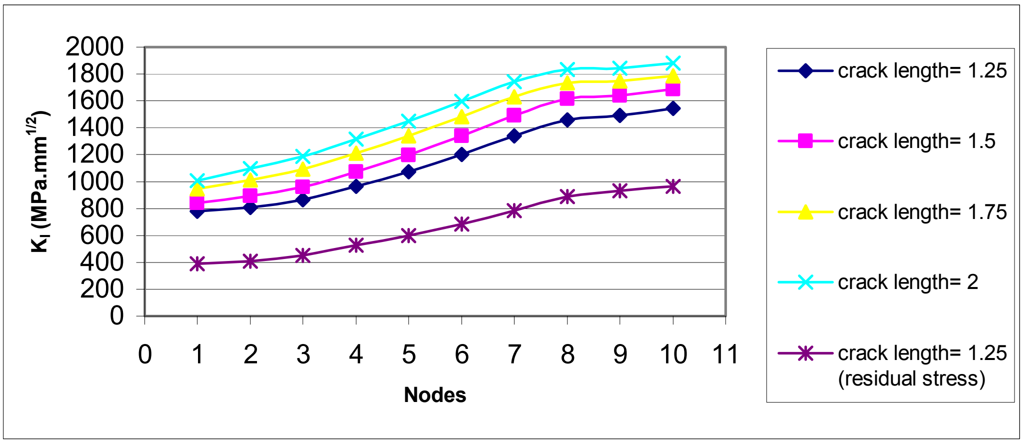

5.11 (b)

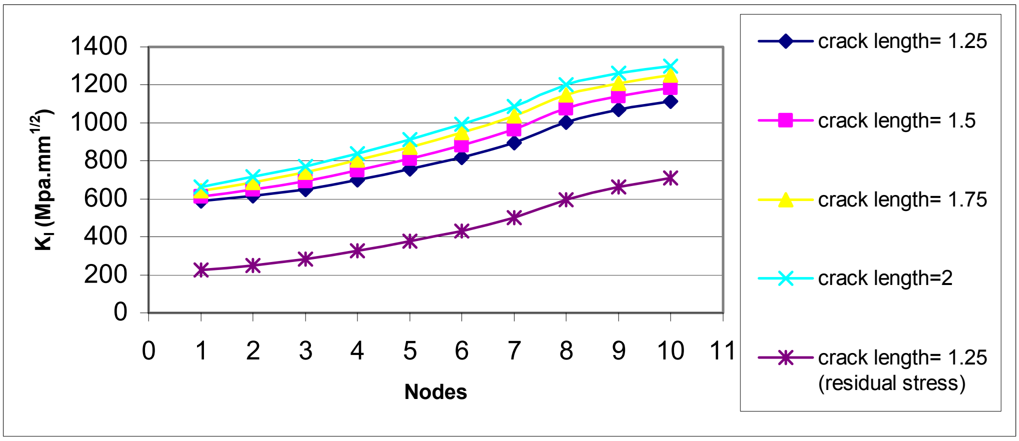

5.11 (c)

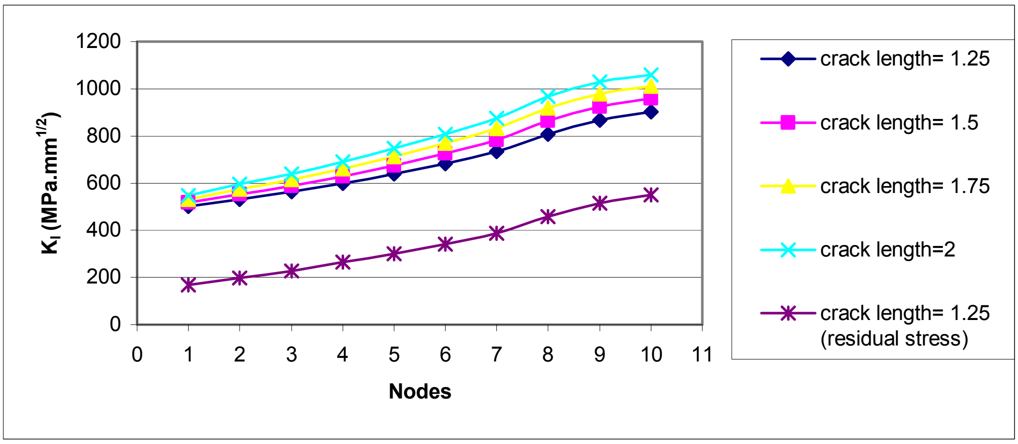

5.11 (d)

**Figure 5.11** Variation o the mode-I stress intensity factor as a function of crack lengths for clearance values of (a) 0.055 mm, (b) 0.095 mm, (c) 0.135 mm, (d) 0.170 mm for crack tip-1

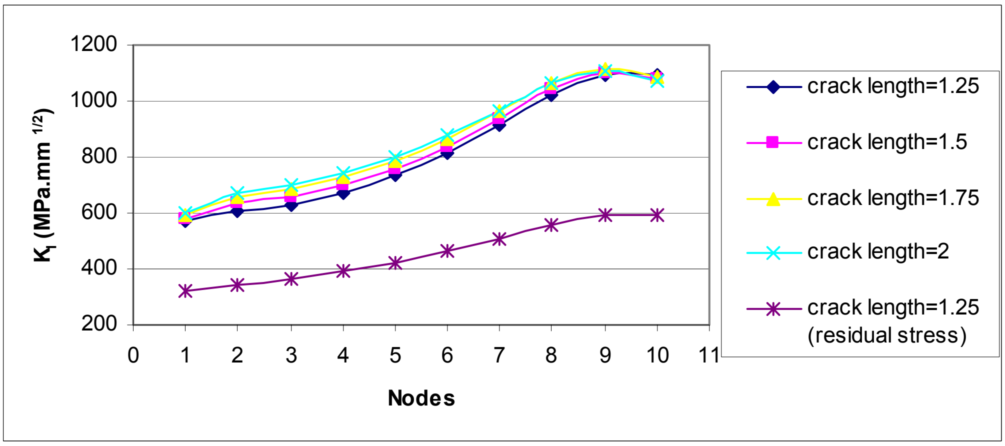

5.12 (a)

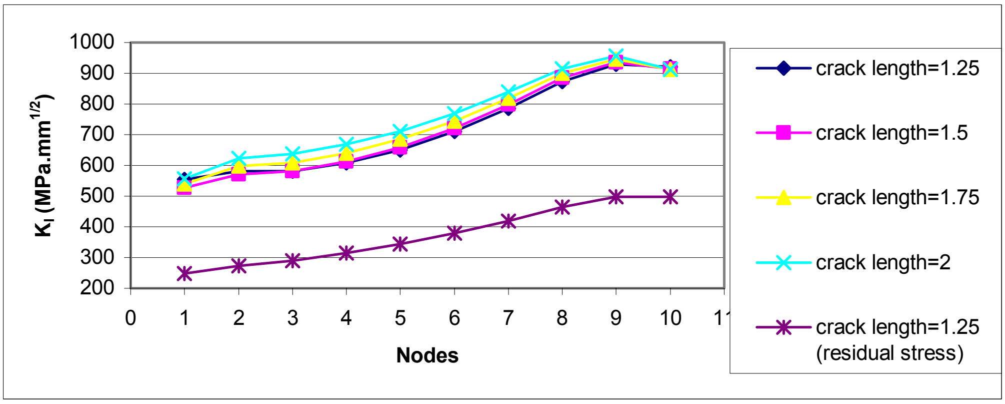

5.12 (b)

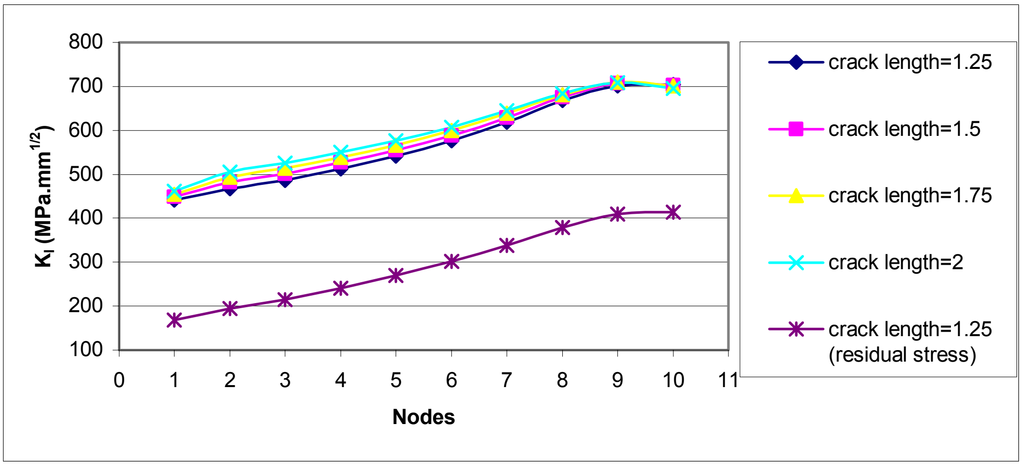

5.12 (c)

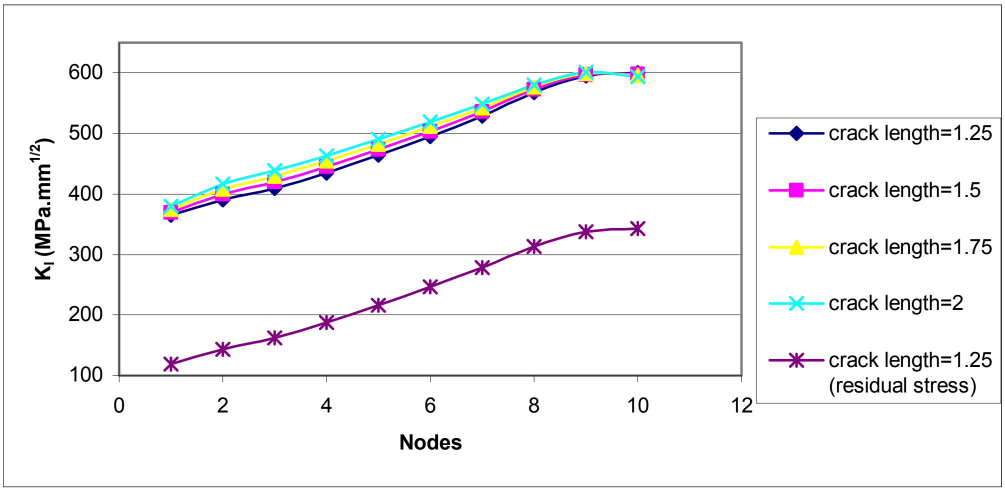

5.12 (d)

**Figure 5.12** Variation o the mode-I stress intensity factor as a function of crack lengths for clearance values of (a) 0.055 mm, (b) 0.095 mm, (c) 0.135 mm, (d) 0.170 mm for crack tip-2

Increasing crack length affected the joint strength adversely and resulted in higher stress intensity factors. Figure 5.11 and 5.12 show that as the crack length was increased the possible risk of failure also increased. Furthermore, the stress intensity factors along crack tip-1 affected from the variations of the crack length more than those of the crack tip-2.

Before closing the discussion of this chapter an approximation to the current study was examined. Hitherto, external loading was applied after the riveting process and the SIF's were calculated. From now on, the same process was approximated by a superposition technique in which the effect of riveting and external loading on the crack will be examined separately and than added. For this purpose a simplified rivet model was generated as illustrated in Figure 5.13. The driven head of the rivet was modeled geometrically. By this way the residual stress field that forms as a result of riveting process was disregarded. Crack length of this model was 1.25 mm and the clearance was 0.055 mm. The boundary conditions were applied and the contacts were defined as in the same manner as the previous model of this chapter.

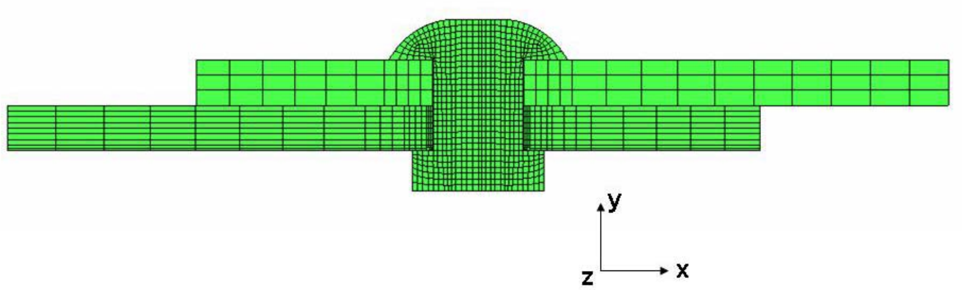

**Figure 5.13** Geometry of the simplified rivet model

Deformed shape of the model was depicted in figure 5.14. In order to observe the deformed shape more clearly the figure was scaled five times in y direction only. In this figure, the rivet tilt due to load eccentricity and separation of the free ends of the plates were clearly seen.

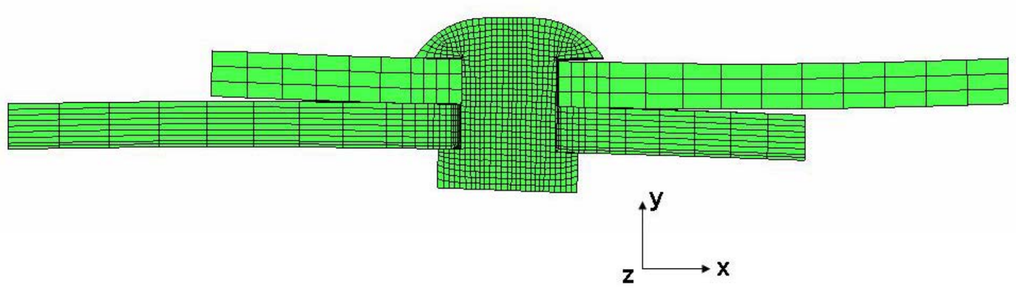

**Figure 5.14** Deformed shape of the simplified rivet model after loading

The results of the current analysis and the previous results were drawn in figure 5.15 and 5.16 so as to compare all the results that were obtained till now.

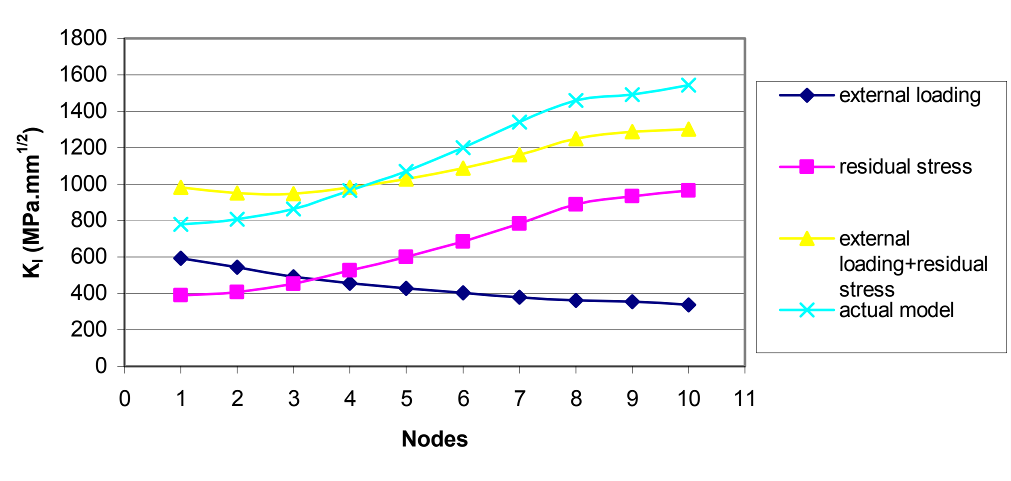

**Figure 5.15** Results of each analysis for crack tip-1

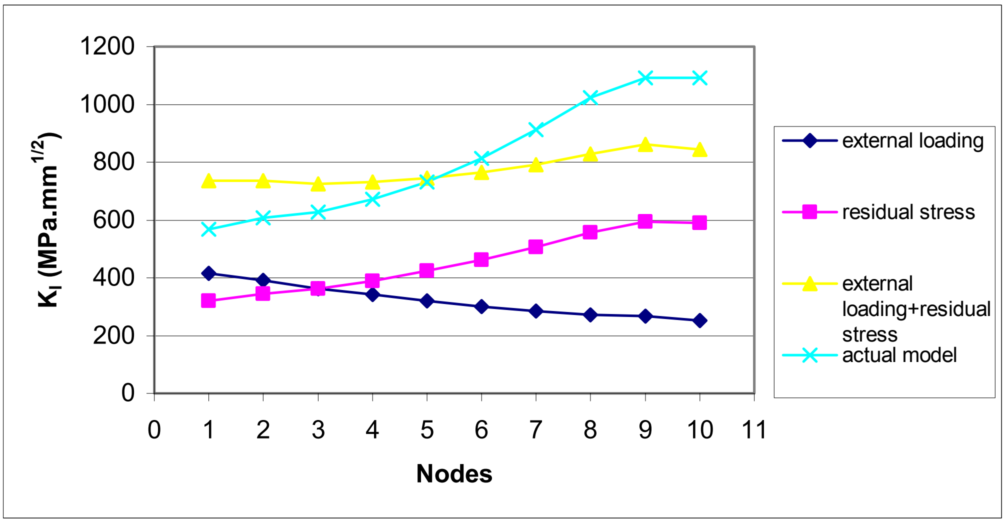

**Figure 5.16** Results of each analysis for crack tip-2

Although the resulting curves are not exactly the same they are similar in magnitude and shape. Therefore, superposition of the results can be used as an approximation to the actual process for all practical purposes.

# CHAPTER-8

# DISCUSSION AND CONCLUSION

Finite element analysis of riveting process was realized in 2-D and 3-D. The capability of the commercial software ABAQUS/CAE in modeling such a nonlinear problem was examined. The results of 2-D model were compared with the experimental studies issued in the literature and with the 3-D model's results. The results were found consistent.

Then, parametric studies were carried out on 2-D axisymmetrical model so as to observe the sensitivity of the model to the changes in the process parameters. Rivet/hole clearance was selected as the parameter to be inspected. A standard rivet was used throughout the study and the clearance values were changed. Residual stress fields were extracted and compared. Inspection of the results revealed that as the clearance was decreased radial and tangential stresses that were formed in the plates increased in magnitude. Higher stress levels were observed in the inner plate than those in the outer plate. Compressive radial stress in the vicinity of the hole edge was beneficial in terms of fatigue performance as it retards the fatigue crack nucleation. On the other hand, a tangential tensile stress zone in the inner plate was observed just after the compressive stress zone. The location of the tensile stress zone is critical in terms of nucleation and subsequent propagation of the fatigue cracks. As the clearance was decreased the magnitude of the tensile stresses in this zone enhanced and the zone was shifted away from the hole periphery. Hence, decreased clearance not only increases the magnitude of the compressive stresses but also moves the hazardous tensile stress zone away from the hole edge.

Moreover, a crack was modeled in a rectangular plate having finite thickness. Tensile loading was applied on the remote edge. The model was solved by using different type elements on the crack tip and by applying varying mesh densities. The mode-I stress intensity factor was extracted from the model and compared with the literature. Effect of the meshing parameters on the results was obtained. The most accurate results were obtained for the model with second order tetrahedral elements on the crack tip. The edge length of these elements influenced the result considerably. Therefore, smallest possible elements were used to model the crack tip singularity in the subsequent model.

Finally, a 3-D model was generated and the inner plate was substituted with a potentially cracked plate. External loading in the form of tensile stress was applied on the edges. In this model, the crack was allowed to open just after the rivet installation in order to catch the effect of the residual stress field. A through crack perpendicular to the loading direction was placed in the inner plate. SIF's were calculated via DCT method. The model was also solved without external loading for comparison purpose. For the unloaded model SIF's were calculated in the residual stress field and it was observed that their values increased with decreasing clearance. High stress magnitudes resulting from small clearances were responsible for this effect. For the loaded configuration only the $K_I$ was calculated since other stress intensity factors could not be predicted accurately with the current model. The $K_I$ values, as expected, were enhanced under effect of external loading. In addition, increased crack lengths were found hazardous as it increased the $K_I$. Finally, it was observed that the crack tip-2, which was away from the hole edge, was affected less than the crack tip-1 from the crack length variations as the latter experienced higher stress variations.

# REFERENCES

1. Szolwinski M.P., “Linking riveting process parameters to the fatigue performance of riveted aircraft structures,” Journal of Aircraft, Vol. 37, No. 1, 2000, pp. 130- 137.

2. Pratt J.D., “Testing and Analysis of Mechanically-Fastened Joints,” Univesity of California, Irvine 2001, Dissertation.

3. Urban M.R., “Analysis of the fatigue life of riveted sheet metal helicopter airframe joints,” International Journal of Fatigue 25, 2003, pp. 1013-1026.

4. Langrand B., Patronell L., Deletombe E., Markiewicz E., Drazetic P., “An alternative numerical approach for full scale characterization for riveted joint design,” Aerospace Science and Technology 6, 2002, pp. 343-354.

5. Toparli M., Ozel A., Aksoy T., “Effect of the residual stress on the fatigue crack growth behavior at fastener holes,” Material Science and Engineering A225, 1997, pp. 196-203.

6. Moreira P.M.G.P. et al.,” Stress intensity factor and load transfer analysis ofa cracked riveted lap joint,” Materials and Design, March , 28 (2007) 1263-1270.

7. Langrand B., Patronelli L., Deletombe E., Markiewicz E., Drazetic P., “Full scale experimental characterization for riveted joint design,” Aerospace Science and Technology 6, 2002, pp. 333-342.

8. DiBattista J.D., Adamson D.E.J., Kulak G.L., “Fatigue Strength of riveted connections,” Journal of Structural Engineering, July 1998.

9. Iyer K.A., “Three dimensional finite element analyses of the local mechanical behavior of riveted lap joints,” Nashville, Tennessee, May 1997.

10. Matos P.F.P., Moreira P.M.G.P., Camanho P.P., Castro P.M.S.T., “Numerical simulation of cold working of rivet holes,” Finite Element Analyses in Analysis and Design 41, 2005, pp. 989-1007.

11. Fung C-P., Smart J., “Riveted single lap joints. Part 1: a numerical parametric study,” Proc. Instn Mech. Engrs, Part G, 1997, 211, pp. 13-27.

12. Xiong Y., Bedair O.K., “Analytical and finite element modeling of riveted lap joints in aircraft structure,” AIAA Journal, Vol. 37, No.1, 1999, pp. 93-99.

13. Ryan L., Monaghan J., “Failure mechanism of riveted joint in fiber metal laminates,” Journal of Material Processing Technology 103, 2000, pp. 36-43.

14. Deng X., Hutchinson J.W., “ The clamping stress in a cold-driven rivet,” Int J Mech Sci., Vol 40, No. 7, 1998, “Fatigue strength of riveted connections,” Journal of structural engineering, July 1998, pp. 792-797.

15. Heywood R.B. “Designing Against Fatigue,”, 1962, pp.230-242 (Chapman and Hall Limited London, 1979).

16. Fung C-P., Smart J., “Riveted single lap joints Part 2: fatigue life prediction,” Proc. Instn Mech. Engrs, Part G, 1997, 211, pp. 123-128.

17. Silva L.F.M. et al., “Multiple-site damage in riveted lap-joints: experimental simulation and finite element prediction,” International of Fatigue 22, 2000, pp. 319-338.

18. Ralph W.C. et al., “Effect of various aircraft production drilling procedures on hole quality,” International Journal of Fatigue, September 2005.

19. Liao M. et al., “Analytical methodology for predicting fatigue life distribution of fusalge splices,” International Journal of Fatigue, 23(2001), 177-185.

20. Courtin S. et al., “Advantages of the J-integral approach for calculating stress intensity factors when using the commercial finite element software ABAQUS,” Engineering Fracture Mechanics, 72 (2005), 2174-2185.

21. Matos P.F.P. et al.,”Stress intensity factor determination using the finite element method,” http://paginas.fe.up.pt, August 2007.

22. Tada H., Paris P.C., Irwin G., “The stress analysis of cracks handbook,” Del Research Corporation, Missouri, USA, 1973

23. Davies D.P. etal., “Survey of Fatigue Failures in Helicopter Components and Lessons Learnt”, Technical Report, 2007

24. Owen D.R.J., Fawkes A.J., “Engineering Fracture Mechanics- Numerical Methods and Applications,” Pineridge Press Ltd., 1983.

25. Kosker S., ”Three Dimensional Mixed Mode Fracture Analysis of Functionally Graded Material”, M.S. Thesis, Middle East Technical University, Ankara 2007.

26. Kelly B., Costello C., “FEA modeling of setting and numerical testing of aluminum blind rivets,” Journal of Materials Processing Technology 153-154, 2004, pp. 74-79.

27. Han L., Yuong K.W., Chrysanthou A., O’Sullivan, J.M., “The effect of pre-straining on the mechanical behavior of self-piercing riveted aluminum alloy sheets,” Materials and Design, 2005.

28. Fitzgerald T.J., Cohen J.B., “Residual stresses in and around rivets in clad aluminium alloy plates,” Materials Science and Engineering, A188, 1994, pp. 51-58

29. Bellinger N.C., Komorowski J.P., Benak T.J., “Residual life predictions of corroded fuselage lap joints,” International Journal of Fatigue 23, 2001, pp. 349-356.

30. Langrand B. et al., “Numerical approach for assessment of dynamic strength for riveted joints,” Aerosapce Sci. Technology 3, 1999, pp. 431-446.

31. Iyer K., Rubin C.A., Hahn, G.T., “Influence of interference and clamping on fretting fatigue in single rivet-row lap joints,” Journal of Tribology, 2001, Vol. 123, pp. 686-698.

32. Rice J.R., “A path independent integral and the approximate analysis of strain concentration by notches and craks,” Journal of Applied Mechanics, 35 (1968), 379-386.

33. Mackerle J., “Finite element analysis of joining and fastening: A bibliography (1990-2002),” International Journal of Pressure Vessels and Joining, 80 (2003), 253-271.

34. Rijck J.M.M. et al., “The driven head dimensions as an indication of the fatigue performance of aircraft lap joints,” International Journal of Fatigue, 2007.

35. Barsoum R.S., “On the use of isoparametric .nite elements in linear fracture mechanics.” Int J Numer Methods Engng 1976;10:25–37.

# APPENDIX-A

# APPLICATION OF SECOND ORDER ELEMENTS TO THE RIVETING PROCESS

In any finite element analysis selection of the element type plays a crucial role. In order to get an accurate result, user should predict the nature of the problem and assign appropriate element types to the analysis domain. In the beginning of a finite element analysis a comprehensive knowledge of the element properties such as element dimensionality, integration method, interpolation method etc. is required so as to select the correct element type among various elements available in the software library.

In the current study, the first order elements were preferred since the results were compared with similar studies cited in the literature. In addition, first order elements decreased the run time of the analysis considerably and helped us to perform as much trial runs as possible without concerning about the time. However, the accuracy of the problem was preserved by applying mesh refinements wherever necessary. In general, second order elements provide higher accuracy and also capture stress concentrations more effectively. On the other hand, second order elements may cause convergence problems in the contact problems, if the correct interaction property is not assigned. In order to observe the impact of second order elements on the riveting simulation the 2-D axisymmetrical model which was used in Chapter 3 was remeshed with CAX8R 8-node second order axisymmetric elements instead of CAX4R available in ABAQUS library. The resulting von Mises contour plots were presented in Figure A.1. Moreover, in Figure A.2, force displacement histories of the both model were compared.

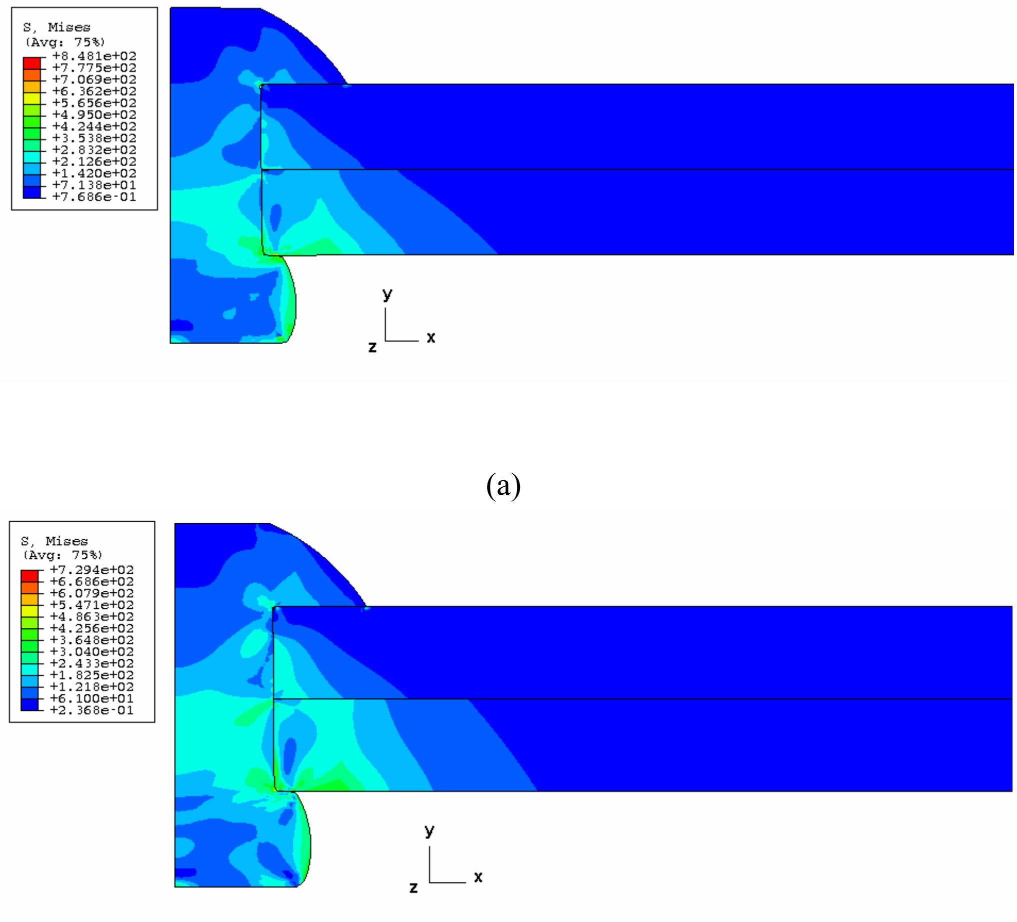

(a)

(b)

**Figure A.1**von Mises contour plots of riveting process with (a) second order elements (b) first order elements

As it is seen from Figure A.1, although vonMises contours look similar to each other, stress levels of both analyses were different. Second order elements caught higher stress concentrations and resulting maximum stress level is %16 higher than that of the first order elements. However, the difference diminishes for the distant points from the stress concentration locations.

**Figure A.2** Comparison of force diplacement histories of both models

In Figure A.2 consistent force displacement curves obtained for the current analyses. As a result, higher order elements should be used for capturing the stress filed more accurately. On the other hand, lower order elements could still give satisfactory results where the displacement field was the main concern.

# APPENDIX-B

# REVIEW OF THE DISPLACEMENT CORRELATION TECHNIQUE

## B.1 Modeling of crack tip singularity

In early attempts conventional constant stress elements are employed in order to use of finite element method in fracture mechanics [24]. However, these elements required extremely refined mesh subdivisions in the vicinity of the crack tip so as to model the strain and stress field singularity. By the help of higher order elements, it became possible to obtain the same order of accuracy with coarser mesh subdivisions. For the accurate numerical solution of the fracture problems it is better to use special crack tip elements which can directly model $1/\sqrt{r}$ near tip singularity. Among various alternatives of such elements an efficient way of introducing $1/\sqrt{r}$ singularity was offered by Barsoum [35]. Barsoum replaced the midside node of an eight noded quadrilateral element to a position which was quarter edge length away from the corner node. This method is known as quarter node point technique. In addition, he collapsed the one side of the element to the crack tip for better accuracy, see

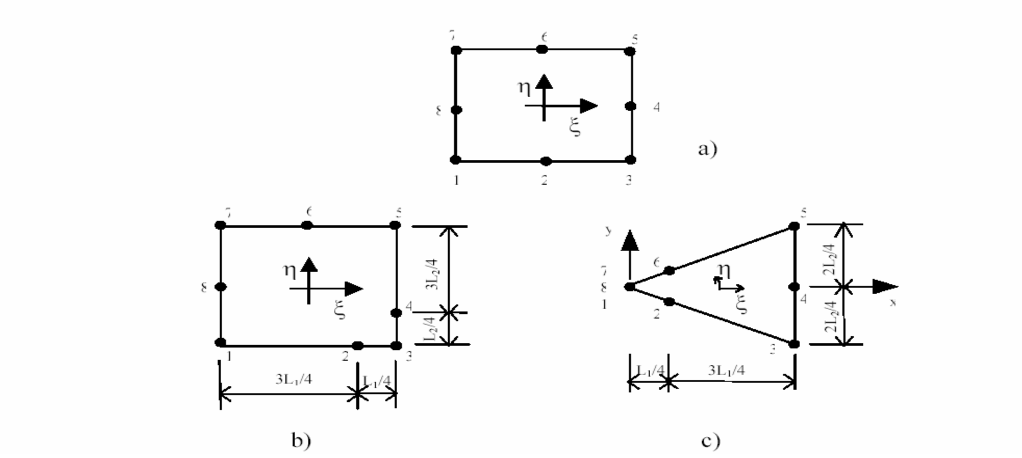

**Figure B.1** (a) 8-node quadrilateral element (b) quadrilateral element with quarter node points (c) collapsed element with quarter node points [21]

## B.2 Calculation of SIF using DCT method

Three stress intensity factors namely $K_I$, $K_{II}$ and $K_{III}$ can be calculated by means of the displacement field obtained by finite element analysis. Displacement correlation technique (DCT) in conjunction with the displacement field can be used to estimate the stress intensity factors. In order to utilize this method, a local coordinate system is positioned on the crack front as shown in Figure B.2. Displacement of point P under the action of mode-I loading can be expressed by Equation B.5 [25].

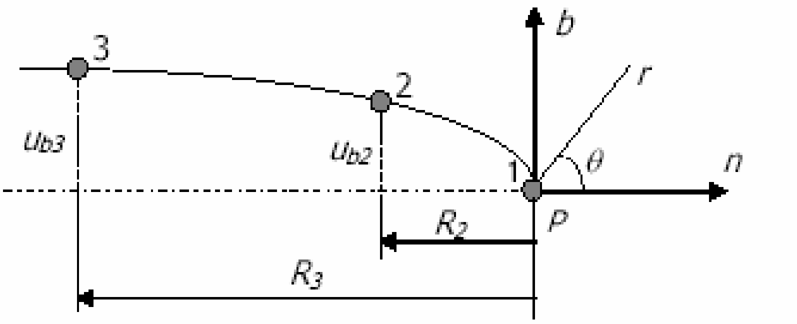

**Figure B.2** Deformed shape of a symmetrical crack surface [25]

$$\mathrm{U_b} = \left(\frac{1+\nu}{E}\right)\times\left(\sqrt{\frac{2r}{\pi}}\right)\times \mathrm{K_I} \times\sin\left(\frac{\theta}{2}\right)\times\left[2(1-\nu)-\cos^2\left(\frac{\theta}{2}\right)\right] \quad \text{(B.5)}$$

In Figure B.2 for θ = π, one can obtain,

$$\mathrm{U_b}\ (\mathrm{r},\pi) = \frac{2(1-\nu^2)}{E}\times\left(\sqrt{\frac{2r}{\pi}}\right)\times \mathrm{K_I} \quad \text{(B.6)}$$

The above expression can be solved for $\mathrm{K_I}$ as,

$$\mathrm{K_I} = \left[\lim_{r\to 0}\left\{\frac{\mathrm{U_b}\ (\mathrm{r},\pi)}{\sqrt{r}}\right\}\right]\times\frac{\sqrt{2\pi}\times E}{4(1-\nu^2)} \quad \text{(B.7)}$$

Assuming a linear solution for the above expression and using the known displacement values at points 2 and 3, Equation B.8 can be obtained as stated below,

$$\mathrm{K_I} = \frac{\sqrt{2\pi}\times E}{4(1-\nu^2)}\times\left\{\frac{R_2^{\frac{3}{2}}\times U_{b3} - R_3^{\frac{3}{2}}\times U_{b2}}{\sqrt{R_2\times R_3}\times(R_2-R_3)}\right\} \quad \text{(B.8)}$$

All these calculations are valid for a symmetrical crack. In the case of a asymmetrical crack, as shown in Figure B.3, the mode-I stress intensity factor is obtained in a similar approach. This time the displacement values of four adjacent nodes to the crack tip are used as a result the mode-I stress intensity factor for a full crack is obtained as shown below,

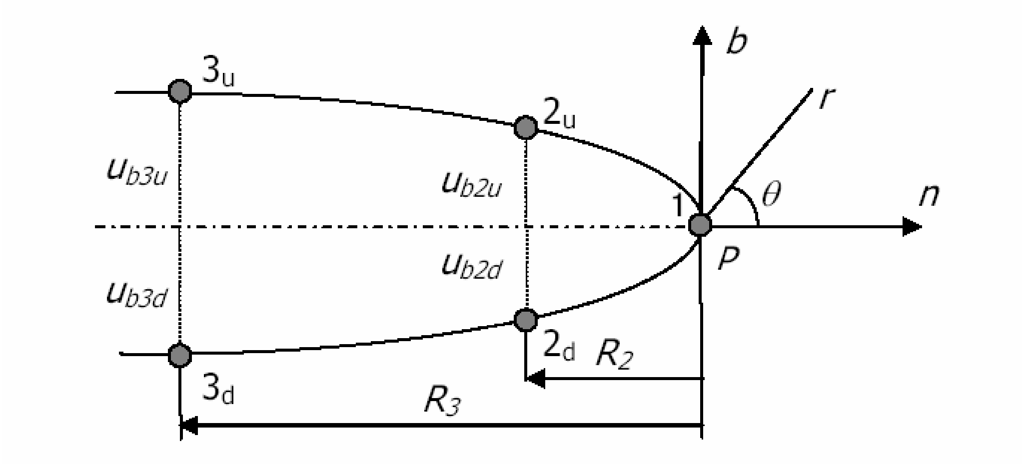

**Figure B.3** Deformed shape of a non-symmetrical crack surface [25]

$$\mathrm{K_I} = \frac{\sqrt{2\pi} \times E}{8\left(1-\nu^2\right)} \times \left\{ \frac{R_2^{\frac{3}{2}} \times \left(U_{b3} - U_{b5}\right) - R_3^{\frac{3}{2}} \times \left(U_{b2} - U_{b4}\right)}{\sqrt{R_2} \times \sqrt{R_3} \times \left(R_2 - R_3\right)} \right\} \qquad \text{(B.9)}$$

In a similar approach using the relevant displacement vector for each type of loading condition the mode-II and mode-III stress intensity factors can be found [33] as stated below,

$$K_{II} = \frac{\sqrt{2\pi} \times E}{8\left(1-\nu^2\right)} \times \left\{ \frac{R_3^{\frac{3}{2}} \times \left(U_{n2u} - U_{n2d}\right) - R_2^{\frac{3}{2}} \times \left(U_{n3u} - U_{n3d}\right)}{\sqrt{R_2} \times \sqrt{R_3} \times \left(R_3 - R_2\right)} \right\} \qquad \text{(B.10)}$$

$$K_{III} = \frac{\sqrt{2\pi} \times E}{8\left(1-\nu^2\right)} \times \left\{ \frac{R_3^{\frac{3}{2}} \times \left(U_{t2u} - U_{n2d}\right) - R_2^{\frac{3}{2}} \times \left(U_{t3u} - U_{t3d}\right)}{\sqrt{R_2} \times \sqrt{R_3} \times \left(R_3 - R_2\right)} \right\} \qquad \text{(B.11)}$$